Open Access Dissertations   Electronic Theses and Dissertations

2019-04-24

Random Phase Modulation of Stationary Light Fields with Applications in Biophotonics

Xi Chen
University of Miami, xichen_cathy@yahoo.com

UNIVERSITY OF MIAMI

RANDOM PHASE MODULATION OF STATIONARY LIGHT FIELDS WITH
APPLICATIONS IN BIOPHOTONICS

By

Xi Chen

A DISSERTATION

Submitted to the Faculty
of the University of Miami
in partial fulfillment of the requirements for
the degree of Doctor of Philosophy

Coral Gables, Florida

May 2019

UNIVERSITY OF MIAMI

A dissertation submitted in partial fulfillment of
the requirements for the degree of
Doctor of Philosophy

RANDOM PHASE MODULATION OF STATIONARY LIGHT FIELDS WITH
APPLICATIONS IN BIOPHOTONICS

Xi Chen

Approved:

_____
Olga Korotkova, Ph.D.
Professor of Physics

_____
Seyed Mohammad Hashemi, Ph.D.
Assistant Professor of Physics

_____
Kenneth J Voss, Ph.D.
Professor of Physics

_____
Guillermo J Prado, Ph.D.
Dean of the Graduate School

_____
Jessica Ramella-Roman, Ph.D.
Associate Professor of Biomedical
Engineering, Florida International
University

CHEN, XI   (Ph.D., Physics)

 Random Phase Modulation of Stationary Light   (May 2019)
Fields with Applications in Biophotonics

Abstract of a dissertation at the University of Miami.

Dissertation supervised by Professor Olga Korotkova.
No. of pages in text. (97)

Light modulation is a vital component in optical communications, imaging and
sensing systems. It imparts information on the optical wave carriers and establishes
the reliability of the communication links. In imaging systems, a modulated light
source has the potential in exceeding the diffraction limit and achieving better con-
trast in images. Improving the performance of light modulating devices such as
Spatial Light Modulators (SLMs), multiplexers, couplers and polarization controllers
can substantially benefit optical sensing and signal processing. Phase modulation
of light, as an important format of light modulation, has gained appreciably more
attention than its amplitude modulation due to its remarkable sensitivity and close
relation to spectrum, coherence and polarization of light.

This dissertation focuses on active (artificial) and passive (natural) phase modu-
lation of light including light source generation, light propagation in biological tissues
and light scattering from deterministic or random media. For genuine light source
generation, two aspects of phase modulation are discussed. One deals with modeling
the complex degree of coherence for 1D and 2D sources. A straightforward sliding
function method is first presented and simple conditions on the sliding function are
derived. The other contribution consists of the experimental method of stationary
beam synthesis from its coherent modes. As an example, the I_m-Bessel correlated

beam with a separable vortex phase is experimentally generated. Moving on to light propagation in biological tissues, the spectral density and the coherence state evolution in isotropic and anisotropic samples are explored and the light scintillation is examined. Finally, light scattering from hollow and semi-hollow 3d scatterers with ellipsoidal, cylindrical and Cartesian symmetries is presented. Interesting intensity patterns coming off these scatterers can lead to prospective applications in inverse problems. The Probability Density Functions (PDFs) of the instantaneous Stokes parameters on weak scattering are also calculated for random stationary scatterers with Gaussian statistics and Gaussian spatial correlation function. The illustrated sensitivity of the Stokes parameters' PDFs to incident light polarization and the scatterers' statistics is of importance for developing novel sensing, communication and imaging schemes operating in the presence of particulate collections.

to my parents

Acknowledgements

First of all, I would like to show my greatest appreciation to my advisor Dr. Olga Korotkova. She is the first person who opened the statistical optics world to me and guided me to this fascinating research field. Her enthusiasm for optics inspired me and strengthened the determination in my research. She helped me with great patience at all stages throughout the research from reading, conducting experiments, solving problems to writing and publishing the results. She supported me not only through my research as a mentor, but also gave me important suggestions for career path as a friend. She encouraged me and offered me the opportunities to attend professional conferences and to present my research. She introduced me to the optics society and helped me build my connections to the networking. I would never become a researcher as I am today without her generous help and endless support.

Secondly, I would like to thank my committee members (Dr. Seyed Mohammad Hashemi, Dr. Kenneth J Voss and Dr. Jessica Ramella-Roman) and my colleague (Dr. Jia Li). I am grateful to Dr. Hashemi for the opportunity to work in his lab and invaluable advice that he gave me throughout the projects. Without his contribution the projects would not progress smoothly to where they are now. His crucial remarks helped me shape and enrich my dissertation. I am also thankful to Dr. Jia Li for sharing his experiences and great support to the projects.

Last but not the least, I would like to express my deepest gratitude to my parents and friends. Their warm love and endless support help me achieve what I have in my life and encourage me to go further in the future.

<div align="right">Xi Chen</div>

University of Miami

May 2019

Table of Contents

3　LIGHT PROPAGATION IN SOFT BIOLOGICAL TISSUES　46

List of Figures

List of Tables

CHAPTER 1

Introduction

1.1   The significance of statistical optics

The state of nature is fundamentally random and almost nothing in nature can be predicted precisely. For instance, uncertainty principle in quantum mechanics states that the photons of the same spin state (same polarization) belonging to a cell of phase space (counterpart in classical coherence theory known as coherence volume) are intrinsically indistinguishable. Each quantity in nature has its own probability density function. When measurements occur, the state of the quantity collapses to the eigenstate of the measurement, hence it is impossible to obtain the state of the quantity before the measurement. In addition, experimental devices used for optical measurements involve even more complex statistics of light interacting with matter, leading to extremely complicated probability density functions.

As an example to illustrate the importance of statistical optics, let us consider an imaging system. The goal of an imaging system is to retrieve and record information about samples using the interaction of light and matter. First of all, the illumination in imaging systems has its statistical properties. The state of the illumination is random and the optical waves that it emits are randomly fluctuating. Then the light

wave travels to the sample and interacts with it. This process can be extremely complicated, it might involve a number of linear and/or nonlinear interactions. Moreover, certain interactions might result in generation of secondary light fields oscillating at different frequencies. After scattering, the perturbed light waves arrive at measuring devices which involve another light-matter interaction. Along the path from the source to the measurement instrument, the light waves propagate through an ambient medium which adds more unknown statistics to the perturbed light. Furthermore, light passing through lenses and other optical elements will accumulate more errors. In summary, all steps in the imaging system including illumination, transmission, interaction, detection, and image reconstruction involve different random processes. Therefore, it is paramount to understand the statistical properties of optical fields at each step in order to improve the imaging system.

1.2 Basic concepts of coherence theory and Van Cittert-Zernike theorem

In the second-order space-frequency domain coherence theory, the cross-spectral density is an important function characterizing correlations in stationary wavefronts. It is known to be the Fourier transform of the mutual coherence function $\Gamma(\boldsymbol{r_1}, \boldsymbol{r_2}, \tau)$ in space-time domain according to the generalized Wiener-Khintchine theorem [1].

For a fluctuating stationary field $U(\boldsymbol{r}, \omega)$, the cross-spectral density function $W(\boldsymbol{r_1}, \boldsymbol{r_2})$ at any pair of points is defined as the ensemble-averaged correlation of the electric field

$$W(\boldsymbol{r_1}, \boldsymbol{r_2}; \omega) = \langle U^*(\boldsymbol{r_1}, \omega) U(\boldsymbol{r_2}, \omega) \rangle. \tag{1.1}$$

Here $\boldsymbol{r_1}$ and $\boldsymbol{r_2}$ are positions of two points anywhere within the field, oscillating at angular frequency ω, star stands for complex conjugate, and the angular brackets denote an average taken over the ensemble of monochromatic realizations.

In order to serve as a genuine correlation function, the cross-spectral density function W should satisfy the following conditions:

1. W must be square-integrable with respect to ω, i.e.,

$$\int_0^\infty |W(\boldsymbol{r_1}, \boldsymbol{r_2}; \omega)|^2 d\omega < \infty. \tag{1.2}$$

2. If W is a continuous function of its spatial arguments then

$$\iint |W(\boldsymbol{r_1}, \boldsymbol{r_2}; \omega)|^2 d^2r_1 d^2r_2 < \infty \tag{1.3}$$

3. W must be quasi-Hermitian, in the sense that,

$$W(\boldsymbol{r_1}, \boldsymbol{r_2}; \omega) = W^*(\boldsymbol{r_2}, \boldsymbol{r_1}; \omega) \tag{1.4}$$

4. W must be non-negative definite, i.e., for any square-integrable function $f(\boldsymbol{r})$,

$$\iint W(\boldsymbol{r_1}, \boldsymbol{r_2}; \omega) f^*(\boldsymbol{r_1}) f(\boldsymbol{r_2}) d^2r_1 d^2r_2 \geq 0. \tag{1.5}$$

However, it is not an easy task to prove the validity of a correlation function especially due to condition (1.5). The Bochner's theorem of functional analysis provides a simple alternative condition: a valid correlation function W must have representation of the form [2]

$$W(\boldsymbol{r_1}, \boldsymbol{r_2}; \omega) = \int p(\boldsymbol{v}; \omega) H^*(\boldsymbol{r_1}, \boldsymbol{v}; \omega) H(\boldsymbol{r_2}, \boldsymbol{v}; \omega) d^2v, \tag{1.6}$$

where H is an arbitrary function, p is a non-negative Fourier-transformable function.

The most frequently measurable quantity in an optical experiment, spectral-density, is just the cross-spectral density function calculated at two coinciding positions, $\boldsymbol{r} = \boldsymbol{r_1} = \boldsymbol{r_2}$,

$$S(\boldsymbol{r};\omega) = W(\boldsymbol{r},\boldsymbol{r};\omega). \tag{1.7}$$

The cross-spectral density function contains information about both the spectral-density and the coherence state of the field, the complex degree of spectral coherence is defined by expression

$$\mu(\boldsymbol{r_1},\boldsymbol{r_2};\omega) = \frac{W(\boldsymbol{r_1},\boldsymbol{r_2};\omega)}{\sqrt{S(\boldsymbol{r_1};\omega)}\sqrt{S(\boldsymbol{r_2};\omega)}}, \tag{1.8}$$

with its magnitude ranging between 0 and 1, i.e.,

$$0 \le |\mu(\boldsymbol{r_1},\boldsymbol{r_2};\omega)| \le 1. \tag{1.9}$$

In 1934 van Cittert and later Zernike derived a very important relation in coherence theory

$$\mu(\boldsymbol{r_1},\boldsymbol{r_2}) = \frac{1}{\sqrt{S(\boldsymbol{r_1})S(\boldsymbol{r_2})}} \iint_{-\infty}^{\infty} S^{(0)}(\boldsymbol{X})\frac{e^{ik[|\boldsymbol{r_1}-\boldsymbol{X}|-|\boldsymbol{r_2}-\boldsymbol{X}|]}}{|\boldsymbol{r_1}-\boldsymbol{X}||\boldsymbol{r_2}-\boldsymbol{X}|}d^2X, \tag{1.10}$$

which provides a bridge between planar source spectral-density and the complex degree of coherence at any two points in the field radiated from the source. Here $\boldsymbol{r_1}, \boldsymbol{r_2}$ are two points in the radiated field, $S^{(0)}(\boldsymbol{X})$ is the spectral-density at point $\boldsymbol{X}$ in the source plane and k is the wave number of light, $k = 2\pi/\lambda$. If we calculate the complex degree of coherence in the far-field regime, then with Fraunhofer approximation Eq.(1.10) reduces to

$$\mu(\boldsymbol{r_1},\boldsymbol{r_2}) = \frac{1}{\sqrt{S(\boldsymbol{r_1})S(\boldsymbol{r_2})}} \iint_{-\infty}^{\infty} S^{(0)}(\boldsymbol{X})e^{ik\boldsymbol{X}\cdot(\boldsymbol{r_1}-\boldsymbol{r_2})/r}d^2X, \tag{1.11}$$

where $|\boldsymbol{r_1}| \approx |\boldsymbol{r_2}| = r$. Moreover, if the source is of Schell-model type, i.e., the complex degree of coherence only depends on the separation between $\boldsymbol{r_1}$ and $\boldsymbol{r_2}$, then we have

$$\mu(\boldsymbol{r_d}) = \frac{1}{\sqrt{S(\boldsymbol{r_1})S(\boldsymbol{r_2})}} \iint_{-\infty}^{\infty} S^{(0)}(\boldsymbol{X})e^{ik\boldsymbol{X}\cdot\boldsymbol{r_d}/r}d^2X, \tag{1.12}$$

where $\boldsymbol{r_d} = \boldsymbol{r_1} - \boldsymbol{r_2}$. From Eq. (1.12) we can see that the correlation function (cross-spectral density) in the radiated field and the spectral-density in the source plane are essentially Fourier transform pair. More generally this relation can be understood as a reciprocity between the spectral density and the coherence state at two planes that are Fourier transform conjugates to each other. This relation will be employed in the sliding function method that we will introduce for spatial structuring of coherence states.

1.3 Coherent mode decomposition

From the conditions for the cross-spectral density function W mentioned in section 1.2, it is implied that W is a Hilbert-Schmidt kernel. The cross-spectral density can then be expressed in the form of the Mercer's series [3]

$$W(\boldsymbol{\rho}_1, \boldsymbol{\rho}_2, \omega) = \sum_{n=0}^{\infty} \lambda_n(\omega)\psi_n(\boldsymbol{\rho}_1, \omega)\psi_n(\boldsymbol{\rho}_2, \omega), \tag{1.13}$$

widely known as the coherent mode decomposition. Here λ_n and $\psi_n(\boldsymbol{\rho}, \omega)$ are the eigenvalues (weights) and the eigenfunctions (coherent modes) of decomposition. The Hermiticity and the non-negative definiteness of W ensures that all the eigenvalues are real and non-negative, i.e.,

$$\lambda_n(\omega) \geq 0. \tag{1.14}$$

The eigenfunctions with different indexes are mutually orthogonal, i.e.,

$$\int \psi_n^*(\boldsymbol{\rho}, \omega)\psi_m(\boldsymbol{\rho}, \omega)d^3r = \delta_{nm}. \tag{1.15}$$

Moreover, the spectral degree of coherence for each mode is given by the expression

$$\mu_n(\boldsymbol{\rho_1}, \boldsymbol{\rho_2}; \omega) = \frac{\psi_n^*(\boldsymbol{\rho_1}, \omega)\psi_n(\boldsymbol{\rho_2}, \omega)}{|\psi_n(\boldsymbol{\rho_1}, \omega)||\psi_n(\boldsymbol{\rho_2}, \omega)|}. \tag{1.16}$$

It is evidently unimodal, hence the modes are termed coherent. The coherent modes has played a crucial part in understanding the laser resonators [4] and partially coherent beam interaction with random media [5]. Apart from their application to optical radiation they can also be applied to other random structures, for instance, random scattering media [6].

The benefit of coherent mode decomposition method is in the versatility in structuring diverse types of beams, not limited to the Schell-model type. Using this method, we will illustrate the construction of I_m-Bessel correlated beams carrying optical vortices. Beams with helical wavefronts carry orbital angular momentum which may induce torque on an electric dipole. Any pair of points symmetric with respect to the beam axis have phase difference of π, leading to a phase singularity in the center of the beam. These properties propel the technologies known as optical trapping/tweezers, broadly adopted in biological manipulation and micro electromechanical systems.

Let us choose eigenfunctions $\psi_n(\boldsymbol{\rho}, \omega)$ in Eq. (1.13) to be the Laguerre-Gaussian (LG) modes [7]

$$\psi_n^m(\boldsymbol{\rho}; \omega) = \left(\frac{\sqrt{2}\rho}{\sigma}\right)^m L_n^m\left(\frac{2\rho^2}{\sigma^2}\right)\exp\left(-\frac{\rho^2}{\sigma^2}\right)\exp[-im\phi], \tag{1.17}$$
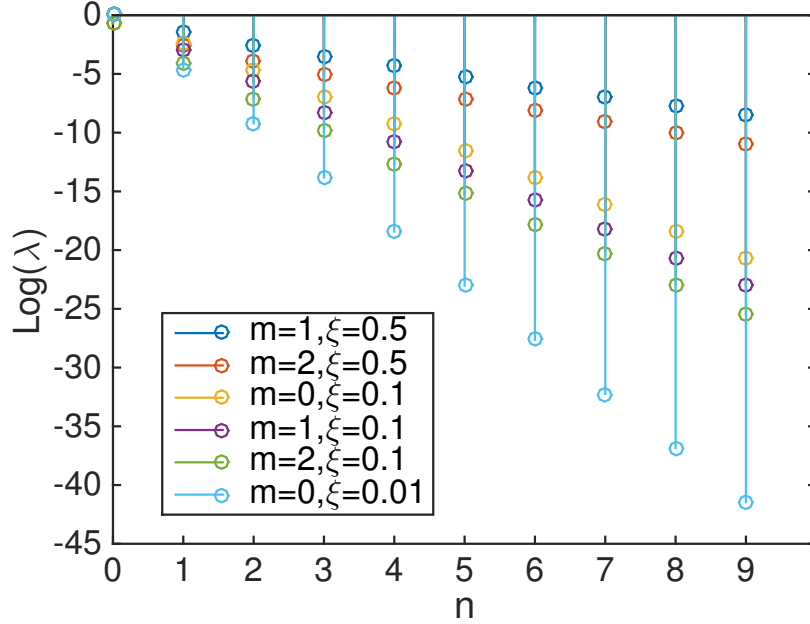
Figure 1.1: Eigenvalues for values m and ξ used in Figs. 2.13-2.14. (From Ref. [40])

where (ρ, ϕ) are the polar coordinates of vector $\boldsymbol{\rho}$, σ is the spot size at the waist of the beam, m is the OAM index, also known as the topological charge. Further, L_n^m is the associated Laguerre polynomial of order n. According to the mutual orthogonality of the eigenfunctions, the eigenvalues λ_{nm} can be obtained as follows

$$\lambda_{nm} = \frac{n!}{(n+m)!}\xi^n. \tag{1.18}$$

The distribution of the eigenvalues with different m and ξ is presented in Fig. 1.1. It is clear that the eigenvalues (weights) decrease extremely fast for smaller values of ξ, implying that beams with larger degree of coherence need fewer coherent modes to generate. We can also see that beams with larger OAMs need fewer coherent modes than those with smaller OAMs.

As was shown in Ref. [8], substitution from Eqs. (1.17) and (1.18) into Eq. (1.13) leads to the cross-spectral density of the form

$$W(\boldsymbol{\rho}_1, \boldsymbol{\rho}_2, \omega) = \frac{\xi^{-m/2}}{1-\xi} \exp\left[-\frac{1+\xi}{1-\xi} \frac{(\rho_1^2 + \rho_2^2)}{\sigma^2}\right] I_m \left(\frac{4\sqrt{\xi}}{1-\xi} \frac{\rho_1 \rho_2}{\sigma^2}\right) \exp[-im(\phi_1 - \phi_2)],$$

(1.19)

with I_m being the modified Bessel function of the first kind, of order m. Parameter ξ appearing in Eq. (1.19) is real ($0 < \xi < 1$) defining the effective width of the source correlation function. $\xi \approx 0$ gives coherent beam; $\xi \approx 1$ leads to incoherent beam. The sequence of real non-negative eigenvalues decreasing to zero with increasing values of n and m defined in Eq. (1.18) determines the effective number of modes needed for the satisfactory synthesis of the beam. The source spectral density is then obtained from Eq. (1.19) by setting $\boldsymbol{\rho}_1 = \boldsymbol{\rho}_2 = \boldsymbol{\rho}$:

$$S(\boldsymbol{\rho}, \omega) = \frac{\xi^{-m/2}}{1-\xi} \exp\left[-\frac{1+\xi}{1-\xi} \frac{2\rho^2}{\sigma^2}\right] I_m \left(\frac{4\sqrt{\xi}}{1-\xi} \frac{\rho^2}{\sigma^2}\right).$$

(1.20)

Since the LG modes are shape-invariant on propagation [1], the (transverse) far-zone radiant intensity, specified along three-dimensional vector $\mathbf{r} = r\mathbf{s}$ ($|\mathbf{s}| = 1$, $|\mathbf{r}| = r$) has the same profile as that in Eq. (1.20) [8]:

$$J(r\mathbf{s}, \omega) = \frac{\sigma^4}{4} \frac{\xi^{-m/2}}{1-\xi} \exp\left[-\frac{1+\xi}{1-\xi} \frac{k^2\omega^2|\mathbf{s}_\perp|^2)}{2}\right] I_m \left(\frac{\sqrt{\xi}k^2\sigma^2|\mathbf{s}_\perp|^2}{1-\xi}\right),$$

(1.21)

where $\mathbf{s}_\perp$ is the two-dimensional projection of vector $\mathbf{s}$ onto the source plane. The model beam introduced in this section will be experimentally synthesized from coherent modes in chapter 2.

1.4 Fourth-order Rytov perturbation theory

In this section we will review the Rytov perturbation theory which will be needed below for studying light evolution in weakly-fluctuating bio-tissues. We will consider the general case first: a Gaussian beam propagation in weak turbulence, then deduce two limiting cases: the plane wave and the spherical wave.

A Gaussian beam is a highly directional optical field whose complex amplitude is given by a Gaussian function. The propagation of a Gaussian wave in 3D space can be conveniently characterized by the set of two dimensionless parameters [9]. Such parameters, Λ_0 and Θ_0, associated with the source plane are defined by expressions

$$\Theta_0 = 1 - L/F_0, \qquad \Lambda_0 = 2L/(kW_0^2), \tag{1.22}$$

where L is the propagation distance, F_0 is the source phase front radius of curvature, and W_0 is the source radius. Then the wave propagating to the detector plane can be characterized by a pair Λ and Θ relating to the source parameter pair as

$$\Theta = \Theta_0(\Theta_0^2 + \Lambda_0^2)^{-1}, \qquad \Lambda = \Lambda_0(\Theta_0^2 + \Lambda_0^2)^{-1}. \tag{1.23}$$

Now consider a scalar optical wave propagating in an unbounded continuous media with smoothly varying stochastic refractive index. Under the assumptions including neglected backscattering, neglected depolarization effects, delta correlated refractive index along the propagation direction, and paraxial approximation, the electric field $U(\boldsymbol{r}, \omega)$ at the point $\boldsymbol{r}$ is governed by the stochastic Helmholtz equation

$$\nabla^2 U(\boldsymbol{r}, \omega) + k^2 n^2(\boldsymbol{r}, \omega)U(\boldsymbol{r}, \omega) = 0, \tag{1.24}$$

where k is the wave number, n is the refractive index of the medium.

The Rytov approximation is one of the perturbation approaches to solve the stochastic Helmholtz equation under weak fluctuation conditions. The Rytov method expresses the fluctuating field as

$$U(\mathbf{r}, L) = U_0(\mathbf{r}, L) \exp[\varphi(\mathbf{r}, L)], \tag{1.25}$$

where $\mathbf{r}$ is the transverse position and L is the propagation distance, φ is the complex phase perturbation due to the turbulence having series expansion

$$\varphi(\mathbf{r}, L) = \varphi_1(\mathbf{r}, L) + \varphi_2(\mathbf{r}, L) + \cdots \quad . \tag{1.26}$$

The scintillation index analysis is an indispensable tool in characterizing the global regime of turbulence (weak, moderate or strong) on the optical waves, whether for the well studied atmosphere [10], oceans [11] or the bio-tissues. In weak fluctuation regime, the scintillation is proven to have the following relation to the phase perturbation φ [9]

$$\sigma_I^2(\boldsymbol{r}, L) = 2\Re[\langle \varphi_1(\boldsymbol{r}, L)\psi_1^*(\boldsymbol{r}, L)\rangle + \langle \varphi_1(\boldsymbol{r}, L)\varphi_1(\boldsymbol{r}, L)\rangle], \tag{1.27}$$

where $\Re$ denotes the real part, the angular brackets stand for the ensemble average over the realizations of the fluctuating medium. It is convenient to express it as the summation of the longitudinal and the radial parts as follows [9]

$$\begin{aligned}
\sigma_I^2(\boldsymbol{r}, L) &= [\langle I(\boldsymbol{r}, L)^2\rangle - \langle I(\boldsymbol{r}, L)\rangle^2]\langle I(\boldsymbol{r}, L)\rangle^{-2} \\
&= \sigma_l^2(0, L) + \sigma_r^2(\boldsymbol{r}, L),
\end{aligned} \tag{1.28}$$

where I is the instantaneous intensity. Under the Rytov approximation, the on-axis and the radial components of the scintillation index for homogeneous and isotropic

media are given as [9]

$$\sigma_l^2(0, L) = 8\pi^2 k^2 L \int_0^1 \int_0^\infty \kappa \Phi_n(\kappa) \exp\left(-\frac{\Lambda L \kappa^2 \xi^2}{k}\right)$$
$$\times \left[1 - \cos[L\kappa^2 \xi(1 - (1 - \Theta)\xi)/k]\right] d\kappa d\xi, \tag{1.29}$$

$$\sigma_r^2(\boldsymbol{r}, L) = 8\pi^2 k^2 L \int_0^1 \int_0^\infty \kappa \Phi_n(\kappa) \exp\left(-\frac{\Lambda L \kappa^2 \xi^2}{k}\right)$$
$$\times \left[I_0(2\Lambda r \xi \kappa) - 1\right] d\kappa d\xi, \tag{1.30}$$

where Φ_n is the power spectrum, being the spatial Fourier transform of the correlation function of the refractive index of the medium

$$\Phi_n(\kappa) = \frac{1}{(2\pi)^3} \iiint_{-\infty}^{\infty} C_n(R) \exp(-i\kappa R) d^3 R, \tag{1.31}$$

where κ is the spatial frequency in the Fourier domain.

According to the Rytov theory, the weak regime of turbulence for a Gaussian beam must satisfy the following inequality ([9], p.230.)

$$\sigma_R^2 \Lambda^{5/6} < 1, \tag{1.32}$$

where σ_R^2 is the Rytov variance (the scintillation index of a plane wave).

For the case of a plane wave, $\Lambda = 0$ and $\Theta = 1$, the radial part σ_r^2 vanishes and the longitudinal part becomes [9]

$$\sigma_l^2(0, L) = 8\pi^2 k^2 L \int_0^1 \int_0^\infty \kappa \Phi_n(\kappa) \left[1 - \cos(L\kappa^2 \xi/k)\right] d\kappa d\xi. \tag{1.33}$$

For the spherical incident wave $\Lambda = 0$ and $\Theta = 0$, it follows that the radial part σ_r vanishes and the longitudinal part yields

$$\sigma_l^2(0, L) = 8\pi^2 k^2 L \int_0^1 \int_0^\infty \kappa \Phi_n(\kappa) \left[1 - \cos[L\kappa^2 \xi(1 - \xi)/k]\right] d\kappa d\xi. \tag{1.34}$$

1.5   Extended Huygens-Fresnel Principle

In this section we will review another widely used method for treating evolution of light in stationary media. This approach will be applied below for examining the effects of isotropic and anisotropic bio-tissues on light spectral density and coherence state. The extended Huygens-Fresnel principle is a powerful approach for solving stochastic Helmholtz equation which governs the light wave propagation in random media. It is applicable for first-order and second-order field moments under weak or strong fluctuation conditions of turbulence.

The solution of Eq. (1.24) is expressed, according to the extended Huygens-Fresnel integral as

$$U(\boldsymbol{r},\omega) = -\frac{ik\exp(ikz)}{2\pi z}\int U(\boldsymbol{\rho}',\omega)\exp\left[ik\frac{(\boldsymbol{\rho}'-\boldsymbol{\rho})^2}{2z}\right]\exp[\Psi(\boldsymbol{\rho}',\boldsymbol{r},\omega)]d^2\rho', \quad (1.35)$$

where $\Psi(\boldsymbol{\rho}',\boldsymbol{r},\omega)$ is the complex phase perturbation caused by the stochastic refractive index of the medium. The second-order correlation of the optical wave can be described by Eq. (1.1).

On substituting from Eq.(1.35) into Eq.(1.1), the cross-spectral density takes form

$$W(\boldsymbol{r}_1,\boldsymbol{r}_2,z) = \iint W(\boldsymbol{\rho}'_1,\boldsymbol{\rho}'_2,\omega)K(\boldsymbol{r}_1,\boldsymbol{r}_2;\boldsymbol{\rho}'_1,\boldsymbol{\rho}'_2,z)d^2\rho'_1 d^2\rho'_2, \quad (1.36)$$

where propagator K is given by expression

$$K(\mathbf{r}_1,\mathbf{r}_2;\boldsymbol{\rho}'_1,\boldsymbol{\rho}'_2,z) = \left(\frac{k}{2\pi z}\right)^2 \exp\left[-ik\frac{(\mathbf{r}_1-\boldsymbol{\rho}'_1)^2-(\mathbf{r}_2-\boldsymbol{\rho}'_2)^2}{2z}\right]$$
$$\times \langle\exp[\Psi^*(\boldsymbol{\rho}'_1,\mathbf{r}_1;\omega)+\Psi(\boldsymbol{\rho}'_2,\mathbf{r}_2;\omega)]\rangle. \quad (1.37)$$

For the homogeneous and isotropic turbulence the phase function is related to the power spectrum $\Phi(\kappa)$ by the formula

$$\langle \exp[\Psi^*(\boldsymbol{\rho'}_1, \mathbf{r}_1; \omega) + \Psi(\boldsymbol{\rho'}_2, \mathbf{r}_2; \omega)] \rangle =$$
$$\exp\left[-4\pi^2 k^2 z \int_0^1 dt \int_0^\infty \kappa d\kappa \Phi_n(\kappa)\left(1 - J_0\left[\kappa\left|(1-t)(\boldsymbol{r_1} - \boldsymbol{r_2}) + t(\boldsymbol{\rho_1} - \boldsymbol{\rho_2})\right)\right|\right]\right)\right],$$

$$(1.38)$$

where J_0 is the Bessel function of the first kind. For the anisotropic turbulence the phase function takes form

$$\langle \exp[\Psi^*(\boldsymbol{\rho'}_1, \mathbf{r}_1; \omega) + \Psi(\boldsymbol{\rho'}_2, \mathbf{r}_2; \omega)] \rangle = \exp\left[-2\pi k^2 z \int_0^1 dt \int_0^\infty d^2\kappa \Phi_n(\boldsymbol{\kappa})\right.$$
$$\left. \times \left(1 - \exp\left[(1-t)(\boldsymbol{r_1} - \boldsymbol{r_2}) \cdot \boldsymbol{\kappa} + t(\boldsymbol{\rho_1} - \boldsymbol{\rho_2}) \cdot \boldsymbol{\kappa}\right]\right)\right].$$

$$(1.39)$$

1.6 Weak scattering theory with Born approximation

Light scattering is a very broad topic and this section will only focus on one type of scattering: elastic light scattering by a linear, isotropic, statistically stationary medium with relative refractive index close to unity. This scattering regime is very convenient for analyzing important problems of light-matter interactions: particle design for controlling scattered radiation [12], scatterer's reconstruction by diffraction tomography method [13], imaging by the quantitative phase microscopy tools [16].

Let the scatterer occupy domain D of a three-dimensional space and be characterized by the scattering potential [3]

$$F(\mathbf{r'}) = \frac{k^2}{4\pi}[n^2(\mathbf{r'}) - 1],$$

$$(1.40)$$

$n(\mathbf{r}')$ being the refractive index at position $\mathbf{r}'$ within the scatterer.

Let us consider the simplest case first: the scalar monochromatic plane wave

$$U^{(i)}(\mathbf{r}, \omega) = a^{(i)}(\omega) \exp[ik\mathbf{s}_0 \cdot \mathbf{r}] \tag{1.41}$$

with amplitude $a^{(i)}(\omega)$ is incident from direction $\mathbf{s}_0$ ($|\mathbf{s}_0| = 1$) onto a deterministic stationary scatterer with potential given by Eq. (1.40). Then under validity of the first Born approximation, the far-zone intensity of the weakly-scattered field, measured along direction $\mathbf{r} = r\mathbf{s}$ ($|\mathbf{s}| = 1, |\mathbf{r}| = r$), can be expressed as [3]

$$S^{(s)}(r\mathbf{s}, \omega) = \frac{1}{r^2} S^{(i)}(\omega) |\widetilde{F}[k(\mathbf{s} - \mathbf{s}_0), \omega]|^2, \tag{1.42}$$

where $\widetilde{F}$ is the three-dimensional spatial Fourier transform

$$\widetilde{F}(\mathbf{K}) = \int_D F(\mathbf{r}'; \omega) \exp\left[-i\mathbf{K} \cdot \mathbf{r}'\right] d^3r', \tag{1.43}$$

and $K = k(\mathbf{s} - \mathbf{s}_0)$ is the momentum transfer vector.

In the electromagnetic case, the three-dimensional scattered electromagnetic field along direction $\mathbf{r} = r\mathbf{s}$, where $\mathbf{s}$ is a unit vector along the direction of vector $\mathbf{r}$, can be found from double cross product [3]:

$$\mathbf{E}^{(s)}(r\mathbf{s}) = -\mathbf{s} \times \left[\mathbf{s} \times \int_D F(\mathbf{r}') G(\mathbf{r}, \mathbf{r}') \mathbf{E}^{(i)}(\mathbf{r}') d^3r' \right], \tag{1.44}$$

where

$$G(\mathbf{r}, \mathbf{r}') = \frac{\exp[ik|\mathbf{r} - \mathbf{r}'|]}{|\mathbf{r} - \mathbf{r}'|} \tag{1.45}$$

is the free-space Green's function. More explicitly, three Cartesian components of the scattered field have the form:

$$E_x^{(s)}(r\mathbf{s}) = (1 - s_x^2)Q_x(r\mathbf{s}) - s_x s_y Q_y(r\mathbf{s}),$$

$$E_y^{(s)}(r\mathbf{s}) = -s_x s_y Q_x(r\mathbf{s}) + (1 - s_y^2)Q_y(r\mathbf{s}), \tag{1.46}$$

$$E_z^{(s)}(r\mathbf{s}) = -s_x s_z Q_x(r\mathbf{s}) - s_y s_z Q_y(r\mathbf{s}),$$

where

$$Q_i(r\mathbf{s}) = \int_D F(\mathbf{r}')G(\mathbf{r}, \mathbf{r}')E_i^{(i)}(\mathbf{r}')d^3r', \quad (i = x, y). \tag{1.47}$$

It is clear that the scattered field depends on coupled incident field components due to the cross product in Eq. (1.44). This approximation will be used in chapter 4 for analyzing the PDFs of the instantaneous Stokes parameters and scattered patterns produced by 3D structured scattering potentials.

CHAPTER 2

Phase Structuring of Complex Degree of Coherence

2.1 Sliding function method

2.1.1 Background

The spatial coherence state of light, as one of the most important observable quantities, inspired a variety of applications including singular optics of random light [14], phase-resolved crystallography [15], quantitative phase imaging of random structures [16], and structured photovoltaics [17]. From the theoretical standpoint, it involves modeling of the magnitude and the phase of the Complex Degree of Coherence (CDC).

In the last several years, modeling of the magnitude of the CDC has become a very well established branch of statistical optics. In particular, it was shown that the magnitude of the CDC leads to radiation of stationary fields with various intermediate- and far-field spectral density profiles perhaps the most illustrative example being the flat-top with a Gaussian edge [18]. So far, structuring of the CDC's phase has been largely overlooked. However, as a few results indicate, inclusion of the non-trivial

phase distribution in the CDC can break the Cartesian symmetry in the far field [19], generate twist phase [20], and lead to other interesting features [21].

Modeling the CDC of a statistically stationary source is not an easy procedure due to a number of constraints including spatial integrability, non-negative definiteness and Hermiticity (see section 1.2). In this chapter, we introduce a very simple method for design of the CDCs with non-trivial phase profiles [22]. This method is valid for the broad class of Schell-like sources (the CDC depends solely on the separation between two points) and relies on the complex-valued sliding function that obeys very simple restrictions: Fourier transformability, even magnitude, and odd phase. The source CDC is shown to be just the auto-convolution of the sliding function.

2.1.2 Theory

Let us start with a one-dimensional (1D) model first. Recall that according to the Bochner's theorem the cross-spectral density of a stationary source can be expressed by Eq. (1.6), for a one-dimensional stationary source it yields

$$W(x_1, x_2) = \int\limits_{-\infty}^{\infty} p(v) H^*(x_1, v) H(x_2, v) dv, \qquad (2.1)$$

where x_1 and x_2 are any source points. For Schell-like sources the correlation class takes the form

$$H(x, v) = \tau(x) \exp[-2\pi i x v], \qquad (2.2)$$

making the cross-spectral density factorize as

$$W(x_1, x_2) = \tau(x_1)^* \tau(x_2) \mu(x_d), \qquad (2.3)$$

where $\tau(x)$ is the complex amplitude profile, $|\tau(x)| = \sqrt{S(x)}$, $S(x)$ being the spectral density. Here $\mu(x_d)$ is the CDC defined as a function of a difference of two points, $x_d = x_1 - x_2$, being the Fourier transform of profile function $p(v)$, i.e., $\mathcal{F}[\mu(x_d)] = p(v)$.

Now let us represent $p(v)$ as a product

$$p(v) = \sqrt{p(v)}\sqrt{p(v)} = h(v)h(v), \tag{2.4}$$

for uniquely defined, real-valued function, $h(v) = \sqrt{p(v)}$. It must satisfy that $\int_{-\infty}^{\infty} |h(v)|dv < \infty$, i.e., belongs to the $L^1(\mathbb{R})$ space. According to the convolution theorem, $\mu(x_d)$ can be expressed as

$$\mu(x_d) = \mathcal{F}^{-1}[h(v)] \circledast \mathcal{F}^{-1}[h(v)] = g(x_d) \circledast g(x_d), \tag{2.5}$$

where $\circledast$ denotes one-dimensional convolution and $g(x_d) = \mathcal{F}^{-1}[h(v)] = \mathcal{F}^{-1}[\sqrt{p(v)}]$. We name $g(x_d)$ as *sliding* function, it will play a crucial part in our analysis. It also needs to be in the $L^1(\mathbb{R})$ space, i.e., $\int_{-\infty}^{\infty} |g(x_d)|dx_d < \infty$.

We can conclude from the properties of the Fourier transform that the sliding function is Hermitian:

$$g(-x_d) = g^*(x_d). \tag{2.6}$$

Indeed, on denoting $g_R(x_d)$ and $g_I(x_d)$ the real and the imaginary parts of $g(x_d)$, respectively, it follows that

$$\begin{aligned}
h(v) &= \int_{-\infty}^{\infty} g(x_d) \exp[2\pi i x_d v]dx_d \\
&= \int_{-\infty}^{\infty} [g_R(x_d) + ig_I(x_d)][\cos(2\pi x_d v) + i\sin(2\pi x_d v)]dx_d \\
&= \int_{-\infty}^{\infty} [g_R(x_d)\cos(2\pi x_d v) - g_I(x_d)\sin(2\pi x_d v)]dx_d \\
&\quad + i\int_{-\infty}^{\infty} [g_R(x_d)\sin(2\pi x_d v) + g_I(x_d)\cos(2\pi x_d v)]dx_d.
\end{aligned} \tag{2.7}$$

It is implied from the last line of Eq. (2.7) that in order for $h(v)$ to be real, its imaginary part must be zero, i.e., $g_R(x_d)$ must be an even function and $g_I(x_d)$ must be an odd function. This condition is equivalent to $g(-x_d) = g^*(x_d)$, being the definition of a Hermitian function.

Further, if the sliding function is represented via its magnitude $g_M(x_d)$ and phase $g_P(x_d)$:

$$g(x_d) = g_M(x_d) \exp[ig_P(x_d)], \tag{2.8}$$

then

$$g_M(-x_d) = g_M(x_d), \quad g_P(-x_d) = -g_P(x_d), \tag{2.9}$$

i.e., the magnitude and the phase of $g(x_d)$ must be even and odd functions, respectively. It is worthy of attention that while the integrability condition on $g(x_d)$ directly affects $g_M(x_d)$, i.e., $\int_{-\infty}^{\infty} g_M(x_d)dx_d < \infty$, it does not affect $g_P(x_d)$.

Now we will generalize this method and apply it for two-dimensional (2D) sources [23]. We will skip the similar procedure and go directly to the conditions for 2D sliding functions. Note that all the integrals now are in 2D.

On expressing function $h(\mathbf{v})$ as the 2D Fourier transform of the real and imaginary parts of function $g(\mathbf{r}_d)$, namely $g_R(\mathbf{r}_d)$ and $g_I(\mathbf{r}_d)$, respectively, it follows that

$$
\begin{aligned}
h(v_x, v_y) &= \int_{-\infty}^{\infty} \int_{-\infty}^{\infty} g(x_d, y_d) \exp[2\pi i(x_d v_x + y_d v_y)] dx_d dy_d \\
&= \int_{-\infty}^{\infty} \int_{-\infty}^{\infty} [g_R(x_d, y_d) + ig_I(x_d, y_d)] \\
&\quad \times [\cos[2\pi(x_d v_x + y_d v_y)] + i \sin[2\pi(x_d v_x + y_d v_y)]] dx_d dy_d.
\end{aligned}
\tag{2.10}
$$

The imaginary part of $h(v_x, v_y)$ is given as

$$\Im[h(v_x, v_y)] = \int\limits_{-\infty}^{\infty} \int\limits_{-\infty}^{\infty} [g_R(x_d, y_d) \sin[2\pi(x_d v_x + y_d v_y)]$$

$$+ g_I(x_d, y_d) \cos[2\pi(x_d v_x + y_d v_y)]] dx_d dy_d. \tag{2.11}$$

After applying summation formulas for sine and cosine it has the expression

$$\Im[h(v_x, v_y)] = \int\limits_{-\infty}^{\infty} \int\limits_{-\infty}^{\infty} g_R(x_d, y_d)[\sin(2\pi x_d v_x) \cos(2\pi y_d v_y)$$

$$+ \cos(2\pi x_d v_x) \sin(2\pi y_d v_y)] dx_d dy_d$$

$$+ \int\limits_{-\infty}^{\infty} \int\limits_{-\infty}^{\infty} g_I(x_d, y_d)[\cos(2\pi x_d v_x) \cos(2\pi y_d v_y)$$

$$- \sin(2\pi x_d v_x) \sin(2\pi y_d v_y)] dx_d dy_d. \tag{2.12}$$

Therefore, in order to have trivial $\Im[h(v_x, v_y)]$, the real and imaginary parts of the sliding function must be even and odd functions respectively, i.e.,

$$g_R(-x_d, -y_d) = g_R(x_d, y_d), \quad g_I(-x_d, -y_d) = -g_I(x_d, y_d), \tag{2.13}$$

i.e., that $g(x_d, y_d)$ is Hermitian in 2D, i.e.,

$$g^*(-x_d, -y_d) = g(x_d, y_d). \tag{2.14}$$

If the sliding function is represented via its magnitude $g_M(x_d, y_d)$ and phase $g_P(x_d, y_d)$:

$$g(x_d, y_d) = g_M(x_d, y_d) \exp[ig_P(x_d, y_d)], \tag{2.15}$$

then it immediately follows from Eq. (2.14) that

$$g_M(-x_d, -y_d) = g_M(x_d, y_d), \quad g_P(-x_d, -y_d) = -g_P(x_d, y_d). \tag{2.16}$$

2.1.3   Examples of 1D field

In order to emphasize on the phase structuring of CDC, we set g_M as a Gaussian function with the r.m.s. width δ, i.e.,

$$g_M(x_d) = \frac{1}{\sqrt{\delta}\pi^{1/4}} \exp\left(-\frac{x_d}{2\delta^2}\right). \tag{2.17}$$

The first example is the linear phase case of the sliding function

$$g_P(x_d) = ax_d. \tag{2.18}$$

On substituting Eqs. (2.17) and (2.18) into Eq. (2.5) the CDC has the expression

$$\mu(x_d) = \exp\left(-\frac{x_d^2}{4\delta^2} + iax_d\right). \tag{2.19}$$

The Fourier transform of $\mu(x_d)$ gives the far-field profile function

$$p(v) = 2\delta\sqrt{\pi}\exp\left[-\delta^2(2\pi v + a)^2\right]. \tag{2.20}$$

Figure 2.1 shows the absolute value, the argument, the real part and the imaginary part of the CDC and the corresponding far-field profile functions, plotted from Eqs. (2.19) and (2.20), respectively, for two selected values of parameter a. The linear phase acts as a tilt. Linear combinations of the CDC with linear phases (with $\delta = \infty$) can be found in coherence gratings [24].

As the second example, we choose *Signum* function

$$g_P(x_d) = \text{sign}(x_d)a = \begin{cases} -a, & x_d < 0, \\ 0, & x_d = 0 \\ a, & x_d > 0. \end{cases} \tag{2.21}$$

Figure 2.1: Degree of coherence (A), (C) and the corresponding far-field profile function (B), (D), for the case of linear phase in (2.18). (A), (B) $a = 2\pi/10$; (C), (D) $a = 2\pi/3$. (From Ref. [22])

Figure 2.2: Degree of coherence (A), (C) and the corresponding far-field profile function (B), (D), for the case of *sign* phase in (2.21). (A), (B) $a = 2\pi/10$; (C), (D) $a = 2\pi/3$. (From Ref. [22])

After performing the auto-convolution in Eq. (2.5) the CDC takes form

$$\mu(x_d) = \begin{cases} \exp\left(-\frac{x_d^2}{4\delta^2}\right)\left(1 + \left(1 - \exp[-2ai]\right)Erf\left[\frac{x_d}{2\delta}\right]\right), & y \leq 0 \\ \exp\left(-\frac{x_d^2}{4\delta^2}\right)\left(1 + \left(\exp[2ai] - 1\right)Erf\left[\frac{x_d}{2\delta}\right]\right). & y > 0 \end{cases} \quad (2.22)$$

The corresponding far-field profile function takes the form

$$p(v) = 2\delta\sqrt{\pi}\exp[-4\pi^2\delta^2 v^2]\left(\cos a - Erfi[\sqrt{2}\pi\delta v]\sin a\right)^2. \quad (2.23)$$

Here, Erf and $Erfi$ are the error function and the imaginary error function defined

as

$$Erf(x) = \frac{2}{\sqrt{\pi}}\int_0^x e^{-t^2}dt,$$

$$Erfi(x) = -iErf(ix). \quad (2.24)$$

Figure 2.2 illustrates $\mu(x_d)$ in Eq. (2.22) and the corresponding far field profile

in Eq. (2.23). The far field shows two asymmetric peaks and non-zero center for

$a \neq \pi/2$. For $a = \pi/2$, we can predict that the intensity vanishes at the center

(destructive interference) and two symmetric peaks with respect to the center because

of the π difference of the phase in the CDC.

Our next example involves the higher-order monomials

$$g_P(x_d) = ax_d^n, \quad n = 2m + 1, \quad m = 1, 2, ... \quad (2.25)$$

for $n = 3$ the CDC takes the form

$$\mu(x_d) = \exp\left(-\frac{x_d^2}{4\delta^2}\right)\exp\left(\frac{iax_d^3}{4}\right)(1 - i3a\delta x_d)^{-1/2}. \quad (2.26)$$

For $\delta = \infty$, $p(v) = |Ai(v)|^2$, where Ai is the Airy function of the first kind but cannot

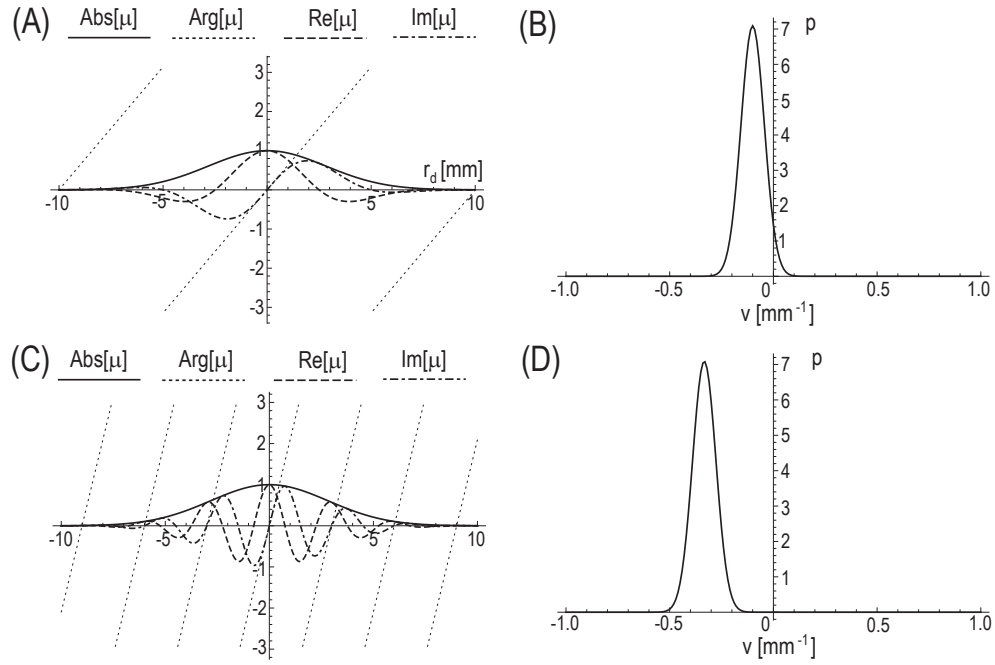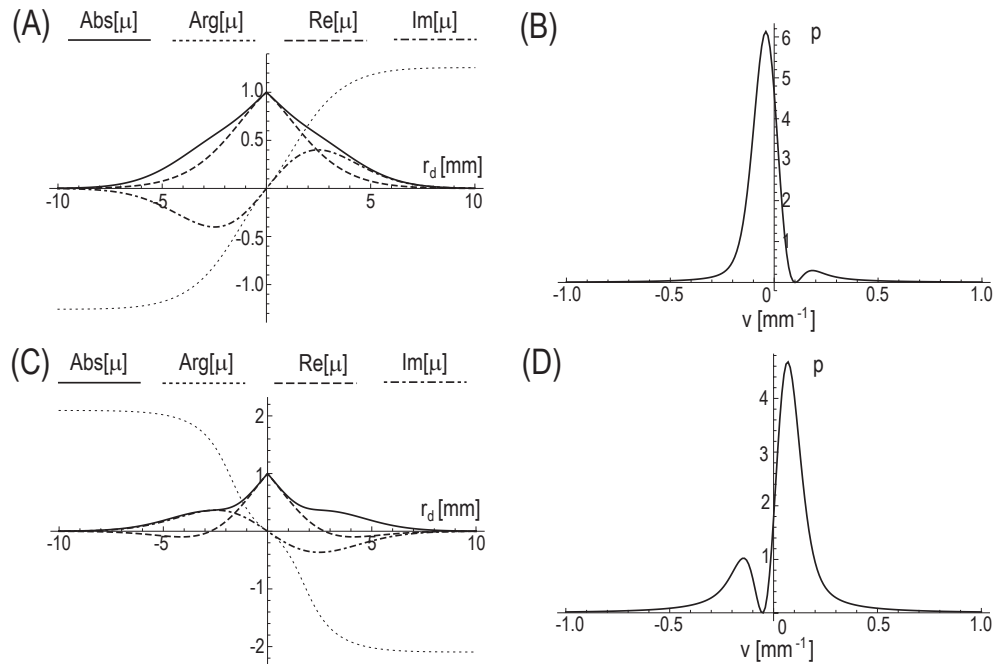be expressed in the closed form for finite δ.
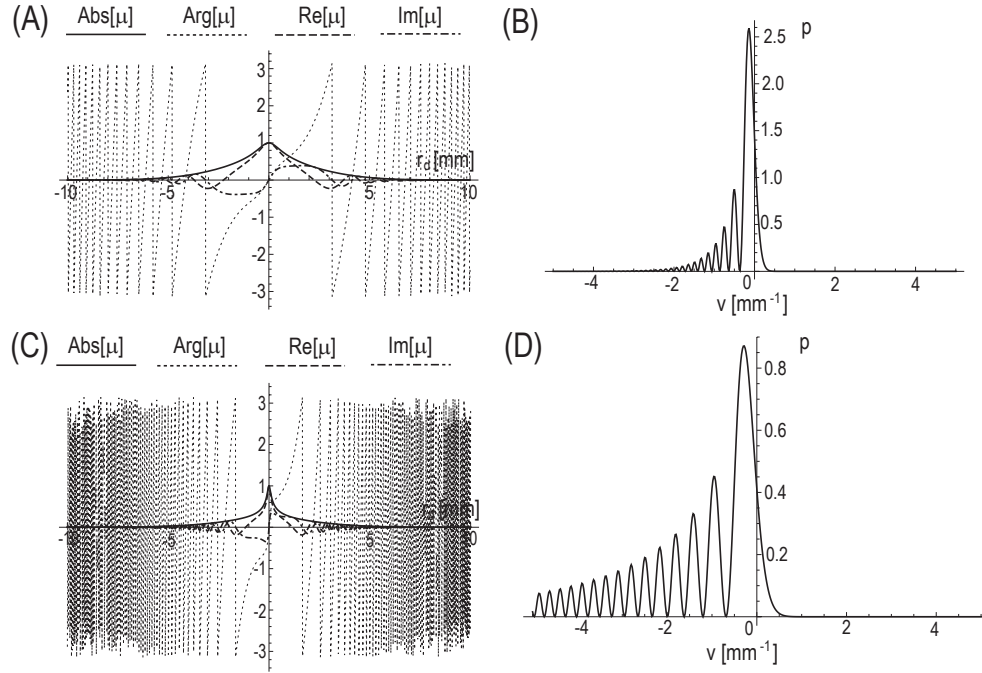
Figure 2.3: Degree of coherence (A), (C) and the corresponding far-field profile function (B), (D), for the case of the cubic phase in (2.25). (A), (B) $a = 2\pi/20$; (C), (D) $a = 2\pi/3$. (From Ref. [22])

The results for $n = 3$ are shown in Fig. 2.3. The far fields radiated by the source with the cubic-phase sliding function (calculated numerically) resemble those for coherent Airy beam [25].

The polarization states of random light can be represented on the Poincare sphere [3], while the coherence states did not have an elegant visual representation so far (except for coherence clouds relating to speckle analysis [26]). We would like to introduce a concept of a *Coherence Curve* (CC) serving as the visual form of the complex coherence state. As we have seen from the suggested examples, in cases where the CDC has a varying phase its representation as a set of functions, such as magnitude, phase, real and imaginary parts, may become overwhelming. Indeed, one can combine the separate plots into a single parametric plot, with parameter x_d, in a

Figure 2.4: Coherence curve diagrams. (From Ref. [22])

complex plane. Then it appears natural to set parameter x_d vary in the interval $[0, \infty)$ and let the real and imaginary parts of the CDC trace a curve. Since the CDC can take on values everywhere within the unit circle (boundary included) of the complex plane and, since its value at $x_d = 0$ is unity, the typical scenario for the CC is to start from real number 1 and to spiral down to zero, p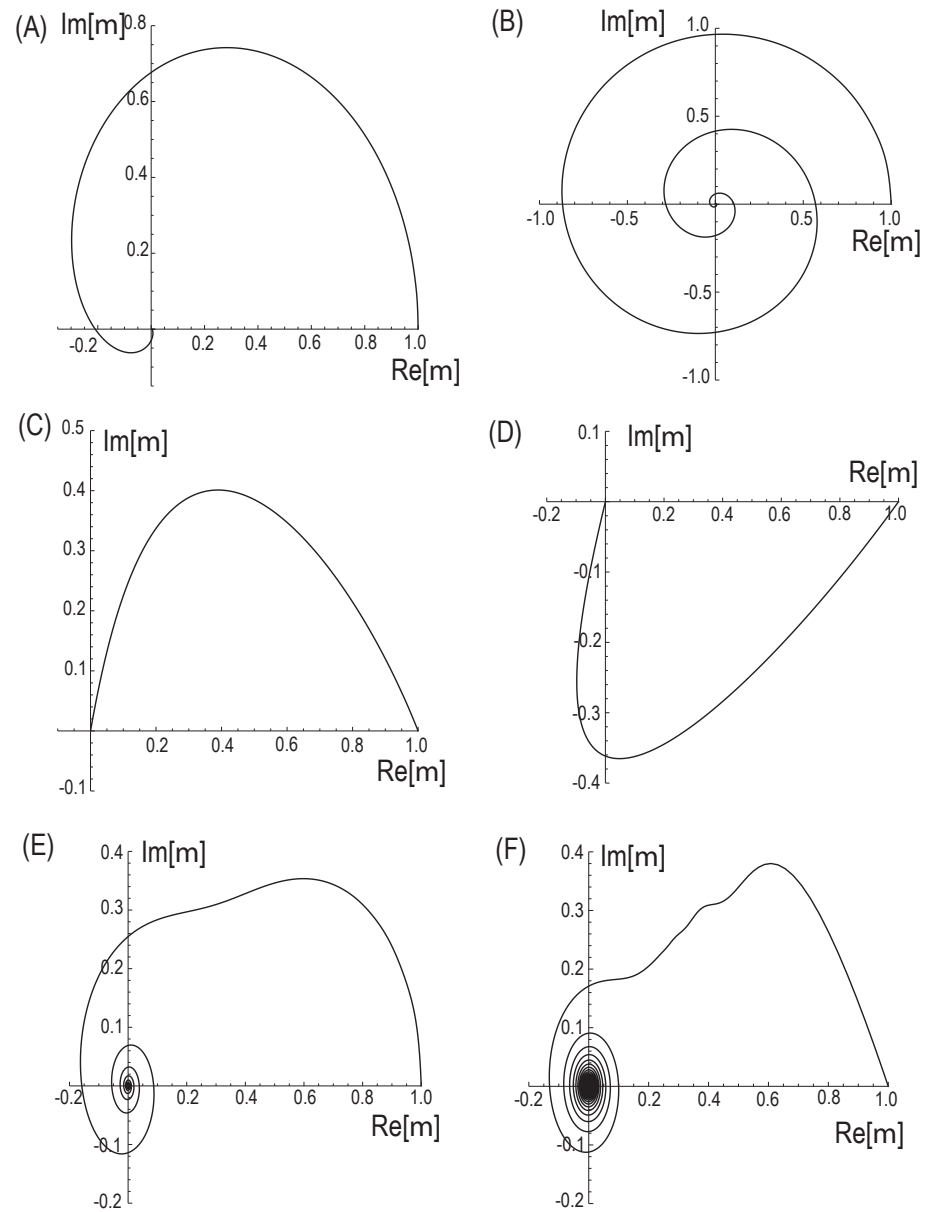erhaps reversing the trend, locally, but globally tending to the origin. Since for $x_d < 0$ the curve is just the reflection of that for $x_d > 0$ with respect to the real line its presence is not necessary.

In Fig. 2.4 we show the CCs for the examples we have introduced earlier. Subplots 2.4(A) and 2.4(B) illustrate the CDC having a linear phase, for $a = 2\pi/10$ and $a = 2\pi/3$, respectively. As a increases the spiral converging to the origin appears to have more loops. We also note that such a CDC [specifically subplot 2.4(B)] is capable of achieving a negative correlation being very close to -1. Subplots 2.4(C) and 2.4(D) correspond to the case of the *sign* phase dependence. The evolution of the degree of coherence here is much more rapid, and virtually no spiraling is possible. This is the consequence of the monotonic phase dependence. Sub figures 2.4(E) and 2.4(F) show the CC curves for the cubic phase dependence. In this case, as the value of parameter a increases the spiral about the origin makes more loops.

Of course, if the information about the x_d values must be preserved, the CDC can also be represented as a 3D parametric curve (with parameter x_d) confined in a semi-infinite cylinder ($x_d \geq 0$) of unit radius, with its transverse axes being $Re[\mu]$ and $Im[\mu]$.

2.1.4 Examples of modeling with famous curves in 1D field

With the concept of CC curves, it is natural to consider planar curves that became famous in different branches of science and engineering. One of the most famous curves satisfying these restrictions is a spiral-like *cochleoid* defined as $r(\theta) = a\sin(\theta)/\theta$, where r and θ are polar coordinates, and a is a positive constant being set to unity here due to the required normalization, $r(0) = 1$. The cochleoid was first introduced by J. Perks in 1699 [27], and its geometrical properties were further studied by Bernoulli and Goldbach in 1726. The cochleoid has been heavily used in engineering since the late nineteen century, in particular for the design of the starting gear of a steam engine [28]. On choosing x_d as a parameter for the polar curve we can set $g(x_d)$ in the form [29]

$$g(x_d) = \frac{\sin(x_d)}{x_d} \left[\cos(x_d) + i\sin x_d\right] \exp(-x_d^2/\delta^2). \tag{2.27}$$

The first and the second factors in Eq. (2.27) represent the cochleoid parametrized by x_d and the third factor is a Gaussian function assuring the sufficiently rapid decrease of $g(x_d)$ to zero for large values of x_d. Its inclusion is not necessary for legitimacy of $g(x_d)$ but rather conveniently controls its width. Figures 2.5A and 2.5B represent $g(x_d)$ for the original cochleoid ($\delta = \infty$) and its truncated version ($\delta = 10\text{mm}$), respectively, as a parametric plot in the complex plane. Figure 2.5C includes magnitude, phase, real and imaginary parts of $g(x_d)$ varying with x_d. Figure 2.5D shows magnitude, phase, real and imaginary parts of $\mu(x_d)$ varying with x_d(for $\delta = 10\text{mm}$). Figure 2.5E demonstrates coherence curve $\mu(x_d)$, corresponding to Fig. 2.5D. Finally, Fig. 2.5F

gives the far-field spectral density. The rest of the figures in this section are organized in the same manner as Fig. 2.5.

One important feature of the cochleoid-based CDC is in the multitude of the 1D singularities occurring at separations $x'_d = \pi n$, $n = \pm 1, \pm 2, ...$, that are inherited from those of $g(x_d)$. A singularity in the CDC is defined as the coherence state at x'_d for which the CDC's magnitude vanish and its phase is undetermined [30]. In the 1D case the CDC's phase singularity can only be represented by a phase jump, i.e., if

$$\lim_{x_d \to x'_{d-}} Arg[\mu(x_d)] \neq \lim_{x_d \to x'_{d+}} Arg[\mu(x_d)]. \tag{2.28}$$

In our example the phase singularities of $\mu(x_d)$ also occur at the same positions as those in $g(x_d)$, however the directions along which the singularities in $\mu(x_d)$ are approached are the opposite from those in $g(x_d)$ (see Figs. 2.5C and 2.5D). This is because that, unlike polar curve $g(x_d)$ being entirely in the upper half of the complex plane for all the positive values of x_d, coherence curve $\mu(x_d)$ crosses the real axis of the complex plane for some positive x_d values (Fig. 2.5E). For our choice of δ the far-field spectral density $p(v)$ of the cochleoid-based CDC has a flat shape in the center and a Gaussian decay at the edge, while the whole distribution is shifted from the optical axis to the left. In the limiting cases when $\delta \to 0$ and $\delta \to \infty$, $p(v)$ tends to have Gaussian and square profiles, respectively, similarly to $p(v)$ in Ref. [18].

Our next example adopts a *lamniscate*, a particular but very well-known member of the Watt's family, that was originally introduced by Jakob Bernoulli in 1694, as a modification of an ellipse and one of the elastica solutions [31]. In polar coordinates the lamniscate is described as $r(\theta) = \pm a\sqrt{\cos(2\theta)}$, for some positive a that we set to unity. Its general properties were studied by Giovanni Fagnano in 1750 and its
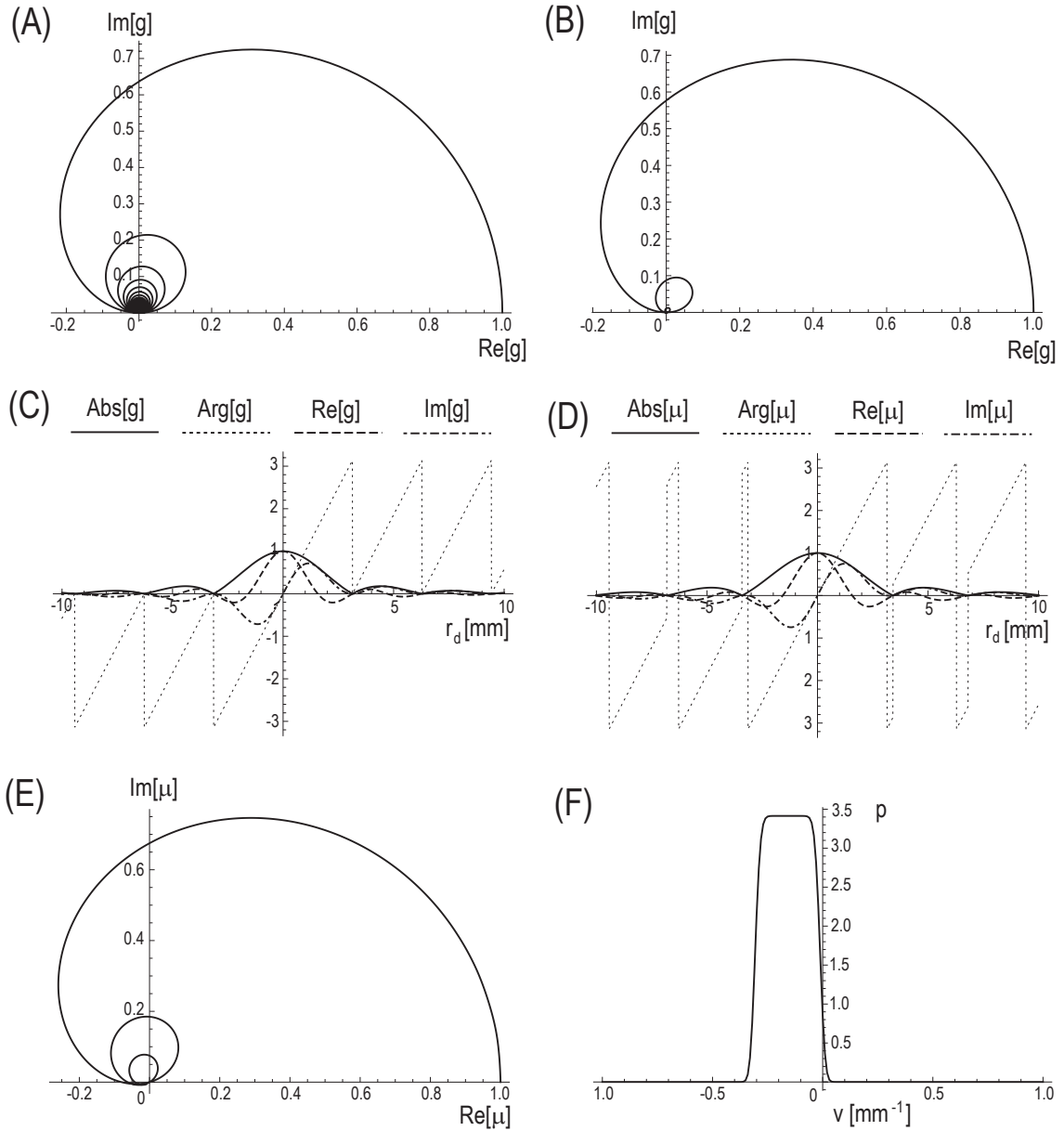
Figure 2.5: (A) parametric representation of $g(x_d)$ of original cochleoid; (B) parametric representation of $g(x_d)$ for cochleoid truncated by a Gaussian function; (C) Abs, Arg, Re and Im parts of $g(x_d)$, corresponding to (B); (D) Abs, Arg, Re and Im parts of $\mu(x_d)$; (E) cochleoid-based coherence curve $\mu(x_d)$; (F) far-field angular spectrak density distribution $p(v)$. (From Ref. [29])
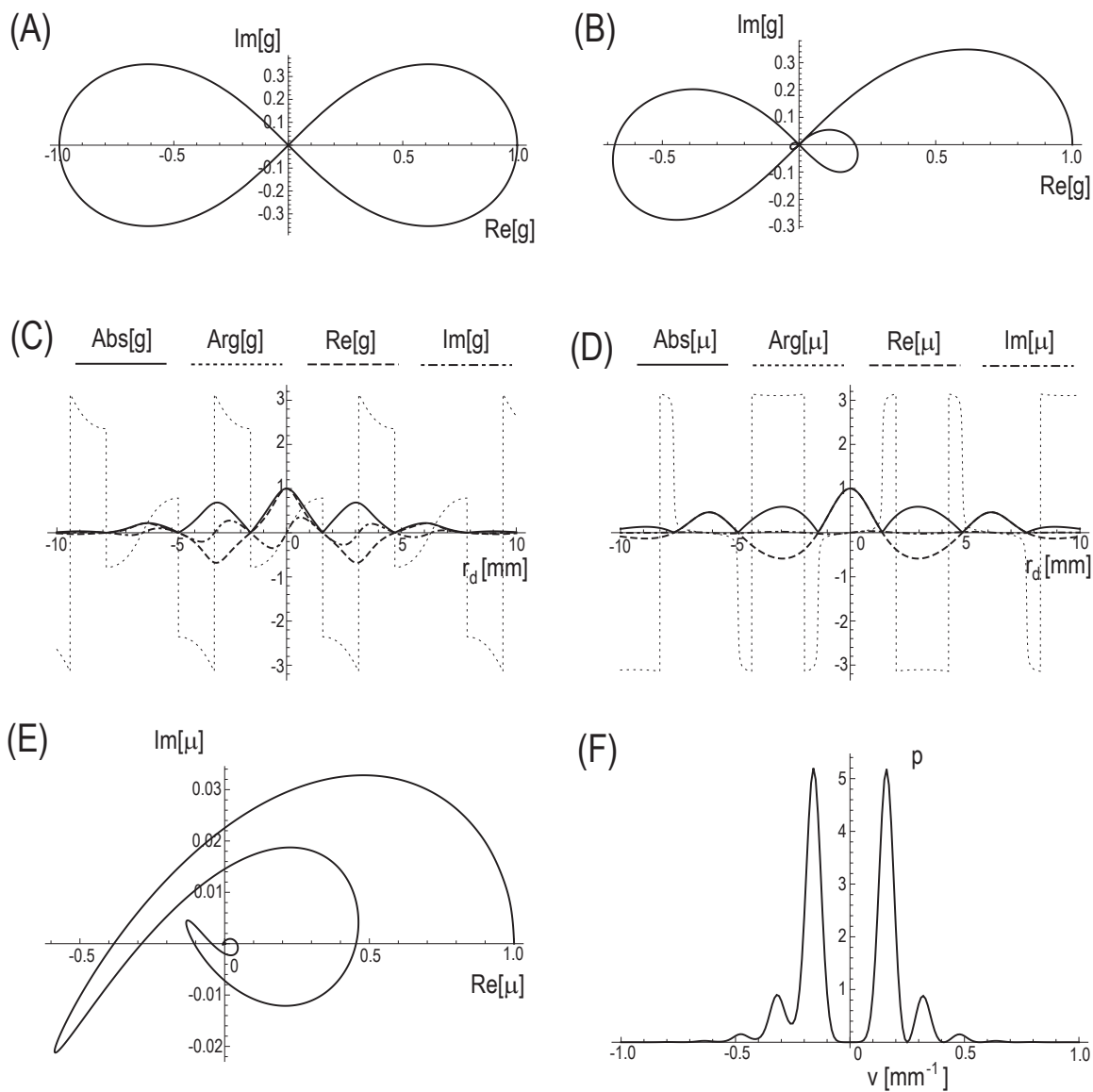
Figure 2.6: Same as Fig. 1 but for lemniscate. (From Ref. [29])

connection to elliptic functions were discovered by Euler in 1751. The lamniscate is prevalent in quasi-1D models describing the dynamics of solid-state particulate systems. Using parametrization by x_d, $g(x_d)$ can be set as

$$g(x_d) = \frac{\cos x_d}{1 + \sin^2 x_d} \left[1 + i \sin x_d\right] \exp(-x_d^2/\delta^2), \tag{2.29}$$

where the truncating Gaussian function is for ensuring the absolute integrability of $g(x_d)$. Figure 2.6 presents the CDC construction for the lamniscate-like sliding function with $\delta = 5mm$. The phase of $g(x_d)$ is confined to ranges $-\pi/4 < \theta < \pi/4$ and $3\pi/4 < \theta < 5\pi/4$ for all x_d (Figs. 2.6A-2.6B). It is clear from Figs. 2.6C and 2.6D that the singularities of $g(x_d)$ disappear in the CDC. The resulting coherence curve (Fig. 2.6E) has a number of changes in directions as it approaches zero for increasing values of x_d, but never crosses the origin. The obtained far-field spectral density (Fig. 2.6F) is a sequence of maxima decaying with larger values of v being symmetric with respect to the optical axis. However, the minima on two sides of the optical axis are not symmetric.

Our last example is from a broad family of *centered trochoids*, formed on tracing a curve by a point attached to a circle with radius b, at distance d from its center, as the circle rolls without slipping along a fixed circle of radius a [32]. Centered trochoids are widely used in engineering for design of rotatory gear pumps, for satellite motion control, etc. [33]. Generally, this class of curves is defined via parametrization

$$g(x_d) = r_1 \exp[ix_d] + r_2 \exp[i(\omega_2/\omega_1)x_d], \tag{2.30}$$

where $r_1 = a \pm b$, $r_2 = d$ and $\omega_2/\omega_1 = 1 \pm a/b$. If $\omega_1\omega_2 > 0$ then the curve is *epitrochoid* (the rolling circle moves outside of the fixed circle) and if $\omega_1\omega_2 < 0$ then

(A)

(B)

(C) Abs[g] ⋯⋯⋯ Arg[g] ⎯ ⎯ Re[g] ⎯·⎯ Im[g]

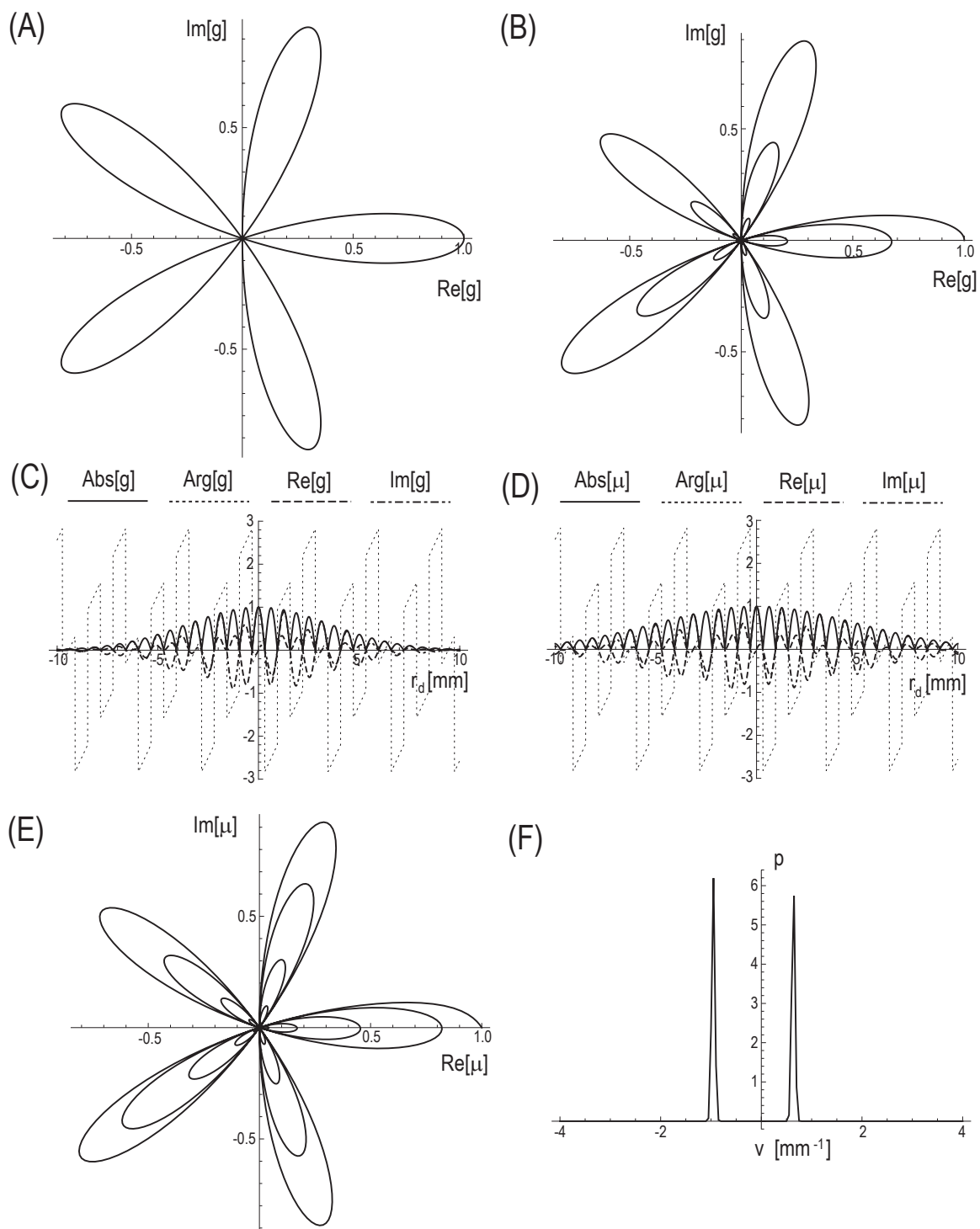(D) Abs[μ] ⋯⋯⋯ Arg[μ] ⎯ ⎯ Re[μ] ⎯·⎯ Im[μ]

(E)

(F)

Figure 2.7: Same as Fig. 1 but for rhodonea. (From Ref. [29])

it is *hypotrochoid* (the rolling circle moves inside of the fixed circle). There are also three other subgroups: *roses* or *rhodoneas* if $r_1 = r_2$; *centered cycloids* if $r_1\omega_1 = r_2\omega_2$ (equal angular speeds); and *trochoids with a meplat* if $r_1\omega_1^2 = r_2\omega_2^2$ (equal angular accelerations).

Let us consider a *rhodonea* curve as a particular example of a centered trochoid for $g(x_d)$, expressed in polar coordinates by relation $r(\theta) = a\cos(b\theta)$, where b is a real number. Rhodonea curves were introduced by Luigi Guido Grandi in 1723 [34]. By setting $a = 1$, parameterizing it by x_d and truncating the result by a Gaussian function yields

$$g(x_d) = \cos(bx_d)\left[\cos x_d + i\sin x_d\right]\exp(-x_d^2/\delta^2). \tag{2.31}$$

Figure 2.7 represents rhodonea structuring of the CDC, with $b = 5mm^{-1}$ and $\delta = 5mm$. It demonstrates that the CDC inherits all the main characteristics of the sliding function for this family of curves, including the set of its singularities. Such a source radiates to the far field with two very well pronounced maxima, asymmetrically positioned about the optical axis, the left maximum being higher than the right one. The smaller values of parameter b result in tighter spacing between the two peaks.

2.1.5   Examples of 2D field

We again set the magnitude of the sliding function to be Gaussian in order to retain the attention on the phase modeling of the CDC

$$g_M(x_d, y_d) = \frac{1}{\delta\sqrt{\pi}}\exp\left(-\frac{x_d^2 + y_d^2}{2\delta^2}\right), \tag{2.32}$$
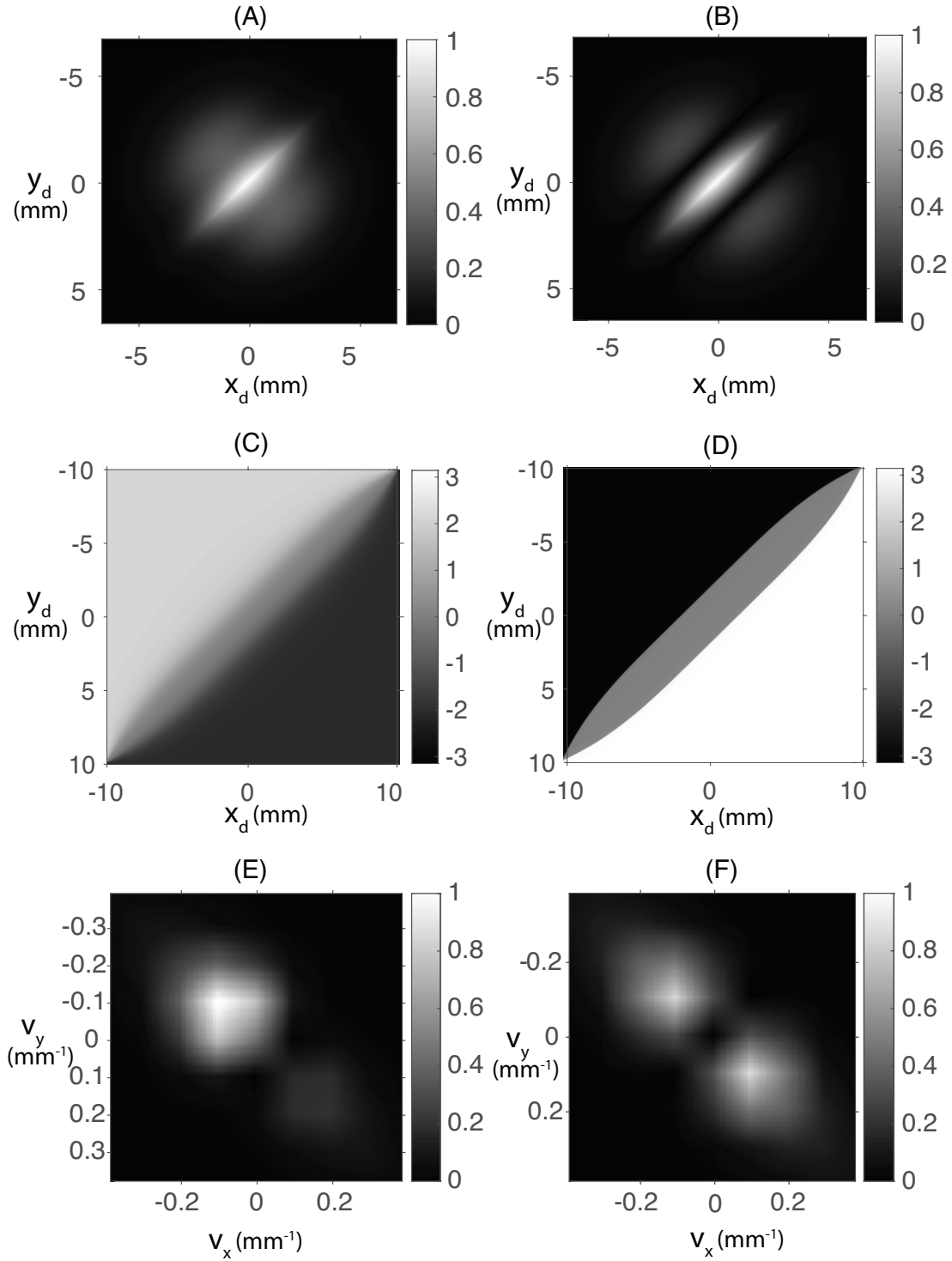
with the r.m.s. width set as $\delta = 1mm$.

Figure 2.8: Magnitude of CDC (A), (B), phase of CDC (C), (D) and the corresponding far-field profile function (E), (F), for the case of the Signum phase. (A), (C), (E) $a = 2\pi/3$; (C), (D) $a = \pi/2$. (From Ref. [23])

Our first example of the non-trivial 2D CDC phase will be obtained with the help of the *Signum* function. Let us set

$$g_P(x_d, y_d) = \text{sign}(\text{x}_\text{d} + \text{y}_\text{d})\text{a} = \begin{cases} -a, & x_d + y_d < 0, \\ 0, & x_d + y_d = 0 \\ a, & x_d + y_d > 0, \end{cases} \tag{2.33}$$

where a is a real parameter. The CDC $\mu(\mathbf{r}_d)$ and the far-field spectral density $p(\mathbf{v})$ can be then evaluated on substituting from Eqs. (2.32) and (2.33) into Eqs. (2.5) and (2.4), respectively. Fig. 2.8 presents the magnitude (top row) and the phase (middle row) of source CDC as well as the corresponding far field (bottom row), evaluated numerically for two values of parameter a: $a = 2\pi/3$ (left column) and $a = \pi/2$ (right column).

The magnitudes of CDC [Fig. 2.8(A) and Fig. 2.8(B)] has two-fold rotational symmetry, inherited from the properties of the sliding function $g(x_d, y_d)$. There are three lobes in the magnitude distributions among which two regions of the CDC are completely vanished with $a = \pi/2$. The parameter a controls the range of the phase of the CDC manifested in Fig. 2.8(C) and Fig. 2.8(D). The phase of the CDC has the value of $-\pi$ and π respectively in the upper and lower region when $a = \pi/2$, while the phase of the CDC can not cover the whole range of complex plane when $a = 2\pi/3$. There is one new feature appearing around the line $y = -x$ with vanished phase due to the convolution of $g(x_d, y_d)$. For the corresponding far field distribution with $a = \pi/2$ [Fig. 2.8(F)], the center shows the completely destructive interference with two peaks symmetric to the line $y = -x$. However, the far field distribution

with $a = 2\pi/3$ breaks the symmetry, having one peak much higher in the upper left than the other peak in the lower right with no destructive interference anymore.

Our next example involves cubic phase which is famous for Airy beams. The separable cubic phase of $g(x_d, y_d)$ takes the form

$$g_P(x_d, y_d) = a[x_d^3 + y_d^3]. \tag{2.34}$$

The non-separable quadratic phase of the sliding function has the expression

$$g_P(x_d, y_d) = a[x_d^2 y_d + y_d^2 x_d]. \tag{2.35}$$

Figures 2.9(A), (C), (E) represent the numerical results from the separable phase in Eq. (2.34), and Fig. 2.9(B), (D), (F) are the numerical results from non-separable phase in Eq. (2.9). The separable phase results are similar to the Airy beam case with some distinctions around the center due to the extra non-cubic phase term resulting from the convolution of the cubic phase. As for the non-separable case results, the four long legs in the magnitude of the CDC for the separable phase disappear with larger coherent area around the center. The center of the corresponding far field shows a triangular peak and several crescent peaks on the side.

Our next example includes sliding functions with polar arctan phase,

$$g_P(x_d, y_d) = 2a\,Arctan\left[\frac{y_d^2}{x_d}\right]. \tag{2.36}$$

The CDC and the far-field profile for the arctan phase calculated numerically are given in Fig. 2.10 for two values of parameter a. It is clear that different values of a govern the distributions for both the CDC and the far field profiles. More separate regions with phase from $-\pi$ to π show up in the phase plot of the CDC with larger

Figure 2.9: Magnitude of CDC (A), (B), phase of CDC (C), (D) and the corresponding far-field profile function (E), (F), for the case of the cubic phase with $a = 2\pi/3$. (A), (C), (E) separable; (C), (D) non-separable. (From Ref. [23])
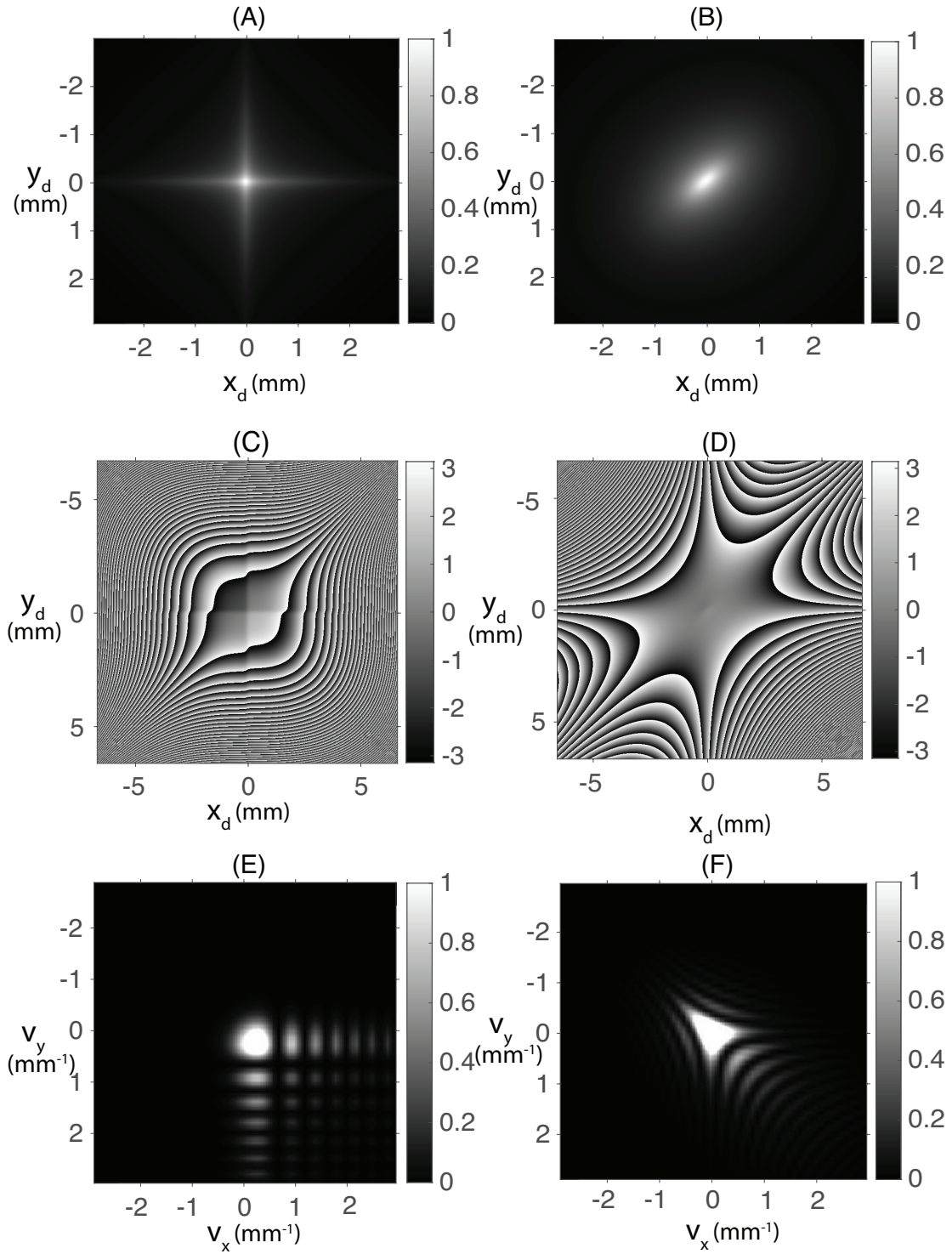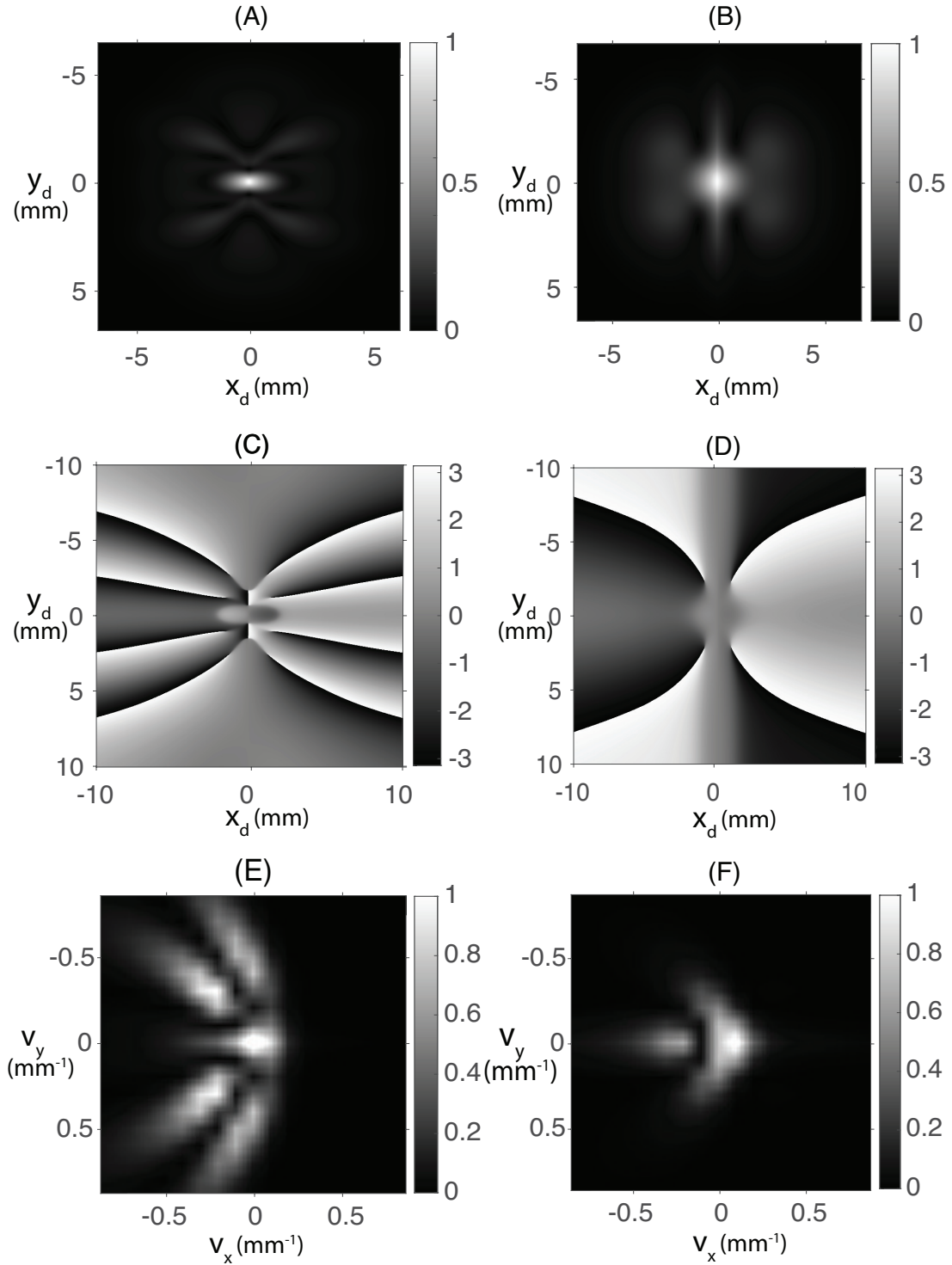
Figure 2.10: Magnitude of CDC (A), (B), phase of CDC (C), (D) and the corresponding far-field profile function (E), (F), for the case of the arctan phase. (A), (C), (E) $a = 2\pi/3$; (C), (D) $a = \pi/5$. (From Ref. [23])

values of a, resulting in more lobes in the source CDC as well as in the far-field spectral density.

2.1.6 Conclusions

In summary we have represented the CDC of a scalar, Schell-like light as an auto-convolution of a Fourier-transformable sliding function, shown to be Hermitian, i.e., having even magnitude and odd phase distributions. Focusing on the phase structuring of the CDC, we illustrated the procedures to model the non-trivial phase of the source CDC and the corresponding far-field spectral density. The concept of the coherence curve as a parametric curve in the complex plane representing the CDC for 1D fields has been introduced, which can serve as a simple visual tool for the coherence state. It can also be extended into 2D and 3D scalar fields, as being a higher dimensional coherence surface.

2.2 Coherent mode decomposition method

In section 2.1, we focused on structuring the phase of the CDC by sliding function method. However, this method is applicable only for Schell-model beams. In this section, we will present the coherent mode decomposition method which is applicable for a variety of beams.

The emerging attention to coherent modes [35], [36], particularly to the LG modes, is stimulated by the development of the fast free-space optical communications where each mode can serve as an information channel [37]. With the coherent modes decomposition, it is convenient to control the weights of the individual modes and therefore to determine the coherent states of the beam. These extensions help to optimize

the channel capacity and improve the performance of the communication systems operating in fluctuating media [38], [39].

In this section, we will show in details how to generate the I_m-Bessel correlated beam from the LG modes experimentally [40]. In particular, we will present the experimental results of the synthesized spectral density and validate the OAM by phase conjugation method.

2.2.1 Experimental setup

The experimental setup for generation is presented in Fig. 2.11(A). A laser beam passes through an SLM with the sequence of random individual LG modes. The probability of selecting a specific LG mode is proportional to its corresponding eigenvalue, λ_{nm}. In this way, the ensemble average of the cycled sequence matches the distribution of the cross-spectral density, $W(\boldsymbol{\rho}_1, \boldsymbol{\rho}_2, \omega)$. In details, we use a 1mm HeNe laser beam ($\lambda = 633nm$) expanded by 15x telescope T (with entrance at 5cm from the laser exit) and then pass it through a nematic phase-only SLM1 (Holoeye 2012) with 724x1024 pixel array, controlled by computer PS1. SLM1 is placed 30cm from the telescope exit. SLM1 acts as a grating producing a two-dimensional array of diffraction orders. The LG modes are programmed onto the first diffraction order which is being reflected by mirror M1 (at distance 200cm from SLM1) and separated from other modes by diaphragm A (at 155cm from M1). The resulting field then passes through lens L (f=50cm, located at 8cm from A) and is captured by the CMOS Thorlabs camera C (at 30cm from L), being controlled by computer PS2.

Figure 2.11(B) shows the experimental setup for validation of the OAM indexes. The path of the beam is the same as that in Fig. 2.11(A) up to diaphragm A (now
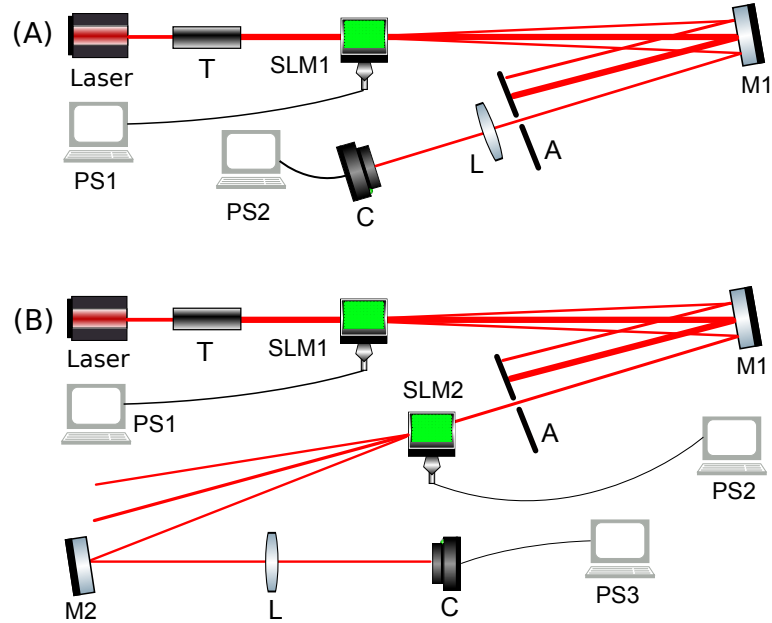
Figure 2.11: Experimental setup for (A) generation of the individual LG modes and their sequences; (B) validation of the OAM indexes. (From Ref. [40])

placed at 30cm from mirror M1), after which it passes through SLM2 (identical to SLM1, at 150cm from A), controlled by computer PS2. The array of diffraction orders is reflected by mirror M2 (at 100cm from SLM2) and then is focuses by lens L (f=50cm, at 20cm from M2) into the CMOS camera (same as in Fig. 2.11(A), at 50 cm from L), controlled by computer PS3.

2.2.2   Results and discussion

The spectral densities (average intensities) of the individual LG modes, normalized by their maximum values are shown in Fig. 2.12. The first four sub figures show the modes with $m = 0$: (A) ψ_0^0; (B) ψ_1^0, (C) ψ_3^0 and (D) ψ_7^0. Modes with $n = 0, ..., 9$ have been successfully generated and used for synthesis of the random beams (not all shown). The limitation for producing modes with $n > 9$ comes from their large size: their outer rings cannot be spatially separated from those of the other diffraction
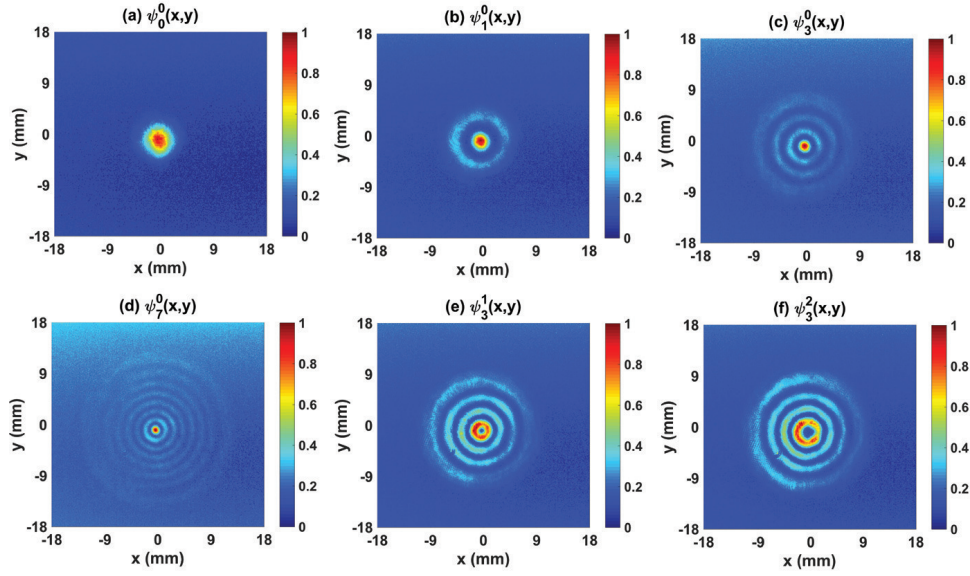
Figure 2.12: Laguerre-Gaussian coherent modes. (From Ref. [40])

orders produced by the SLM, including the zeroth-order bright spot (already seen for $n = 7$ in Fig. 2.12(D)). The last two sub figures give the modes with higher OAMs: ψ_3^1 in Fig. 2.12(E) and ψ_3^2 in Fig. 2.12(F), both having the characteristic ring in the center, larger ring with $m = 2$.

The spectral densities (normalized by its maximum value) of the I_m-Bessel correlated beams recorded by the camera in configuration shown in Fig. 2.11(A) are presented in Fig. 2.13-2.14. In these figures the left column presents the experimentally synthesized spectral density, the middle column reproduces the theoretical distribution plotted from Eq. (1.20) (normalized by its maximum value) and the right column shows the comparison of their one-dimensional cross-sections ($y = 0$).

In particular, the I_m-Bessel correlated beams with $m = 0$ for two values of parameter ξ: $\xi = 0.01$ (top row) and $\xi = 0.1$ (bottom row) are presented in Fig. 2.13. For this range of values only the first several LG modes are required for satisfactory beam
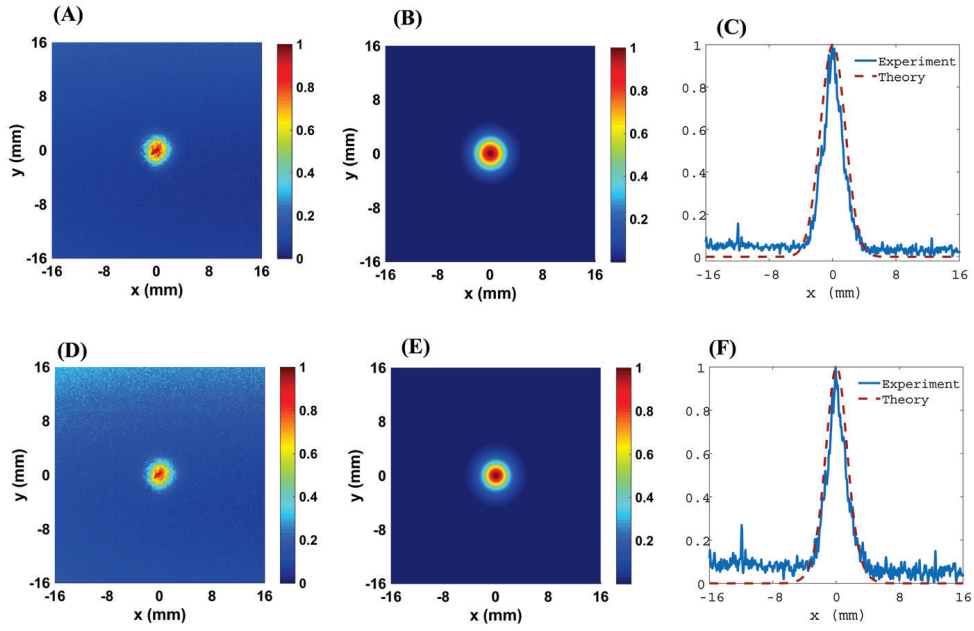
Figure 2.13: I_m-Bessel correlated beam with $m = 0$.(A)(B)(C)$\xi = 0.01$ (D)(E)(F)$\xi = 0.1$ (From Ref. [40])
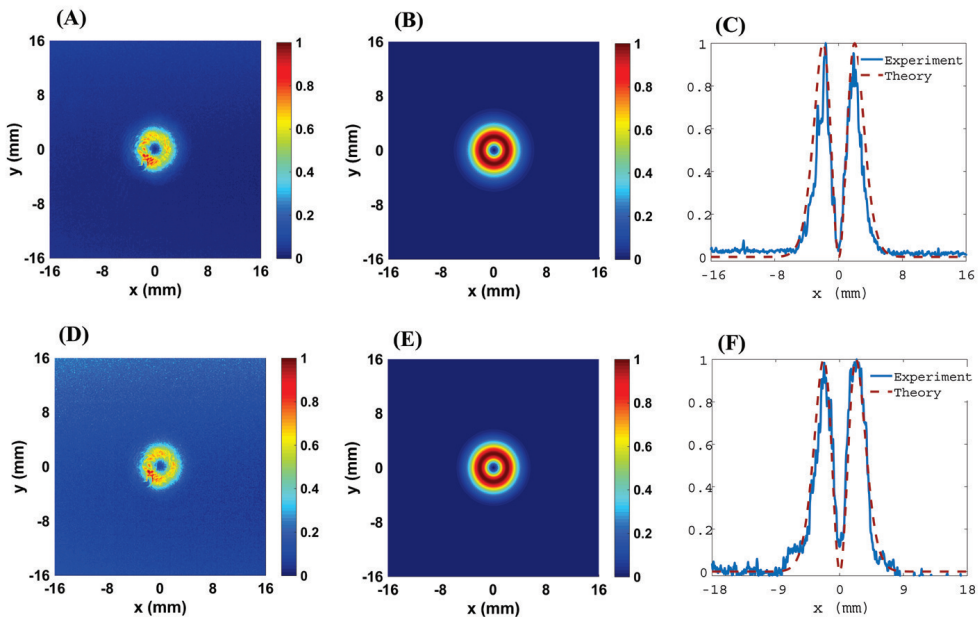
Figure 2.14: I_m-Bessel correlated beam with $m = 1$.(A)(B)(C)$\xi = 0.1$ (D)(E)(F)$\xi = 0.5$ (From Ref. [40])
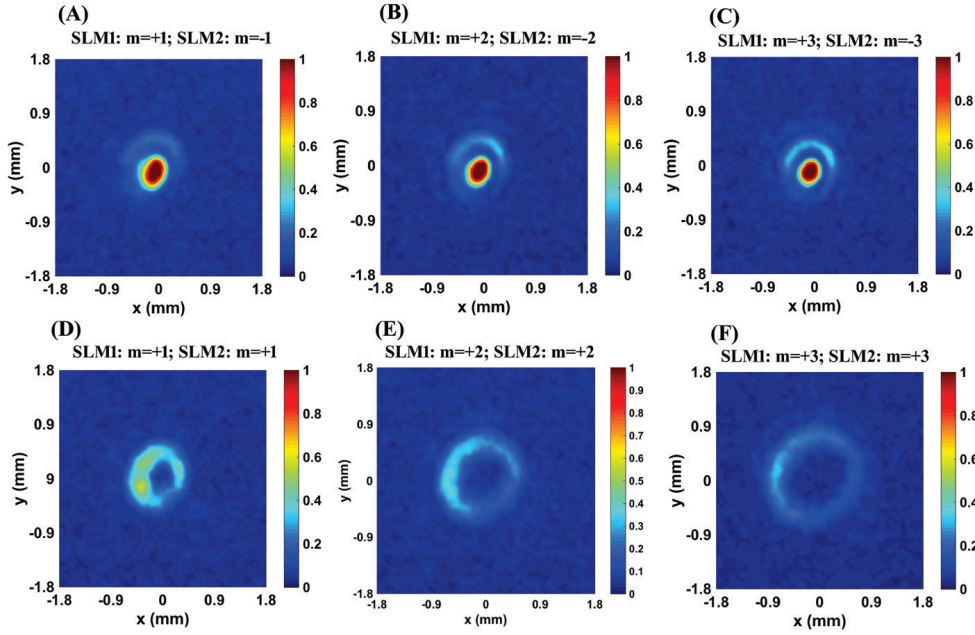
Figure 2.15: Validation of the OAM of the beam by phase conjugation method. (From Ref. [40])

synthesis and the results vary only slightly. The results of the I_0-Bessel correlated beams with $m = 1$ are presented in Fig. 2.14 with $\xi = 0.1$ and $\xi = 0.5$. The spectral density has a larger ring for larger values of ξ and m, which agrees with the theory in Ref. [8],

In Fig. 2.15, we validate the proper OAM carried by the synthesized LG mode. The first diffraction order produced by SLM1 with OAM $m = 1, 2, 3$ is passed through SLM2 on which the LG mode with $m = \pm1, \pm2, \pm3$ is displayed respectively. The constructive interference showing a bright spot in the center is observed when the OAMs on two SLMs have opposite sign due to the phase conjugation. The destructive interference will be presented if the OAMS on the SLMs have the same sign.

2.2.3 Conclusions

In summary, the experimental results of the synthesis of I_m-Bessel correlated beams via superposition of their coherent modes are presented. A random sequence of LG coherent modes with weights proportional to their eigenvalues are used to construct the beam. The LG modes are produced by passing the HeNe Gaussian laser beam through the SLM. The validation of the OAM is carried out by phase conjugation method.

We stress that it is the very first attempt to generate a stationary beam from its coherent modes and it is an entirely digitized method, meaning that the adjustment to other beams within the same class and outside can be readily achieved via reprogramming of the SLM sequence. The simplicity and the versatility of this method will contribute largely to the FSO communication and bio-photonics systems.

CHAPTER 3

Light Propagation in Soft Biological Tissues

3.1 Light scintillation in soft biological tissues

3.1.1 Background

Biological tissues are very complex media for light statistics studies due to their strong refractive index variations at spatial scales greater and smaller than the wavelength of light. The turbulent nature of the refractive index variations was first discovered by Schmitt and Kumar using phase-contrast microscopy in 1996 [41]. The spectrum of the refractive index variations of a typical soft bio-tissue exhibits a power-law behavior which has the same form as the Von Karman spectrum for atmospheric turbulence [9]. However, the variations of the refractive index in bio-tissues can be 9-13 orders of magnitude stronger than those in the atmosphere. Moreover, the outer scales of biological tissues above which correlations are no longer seen are 4-10 μm compared to 5-100 m in atmosphere. In these turbid media with sub wavelength structures, light scattering and absorption is so strong that the penetration depth is only about tens of microns which impedes the analytical studies of deep tissues [42], [43]. This nature of biological tissues also leads to the difficulties in imaging systems and

furthermore in medical diagnostics [44]. To understand the light behavior within biological tissues and to extract useful information are essential and fundamental to bio-optics applications [45].

Until now estimation of typical distances into the bio-tissue at which the coherent wave experiences weak, moderate and strong fluctuations [9] has not been performed. Such classification is conventionally treated with the help of the scintillation index, i.e., the normalized intensity variance, of a plane wave, known as the Rytov variance. The aim of this section is to provide the complete analysis of the scintillation index of a plane wave, a spherical wave and a Gaussian beam on propagation in typical soft bio-tissues and to illustrate the limits of applicability of the Rytov theory [46].

3.1.2   Power spectrum of biological tissues

The power-law (also called fractal or self-affinity) dependence of the tissues' spectra has been adopted for developing successful techniques for cancer diagnostics [47], [48]. Some of the bio-tissues were shown to carry multi-fractal characteristics having values of different power-law slopes for different ranges of spatial scales [49]- [51].

The widely accepted mathematical models for the spatial power spectra and the spatial correlation functions of the soft bio-tissues' refractive index in 1D, 2D and 3D, under the assumptions of their homogeneity and isotropy are summarized in Table 3.1. Here x, ρ and r are the distances between two points in 1D, 2D and 3D, respectively, κ is the magnitude of the spatial frequency vector $\boldsymbol{\kappa}$, $0 < \kappa < \infty$. σ^2 is the ensemble average of the refractive index's variance, being on the order of $10^{-3} - 10^{-4}$ in most soft tissues. Further, L_0 is the outer scale of the tissue which have values around 4 μm in most tissues.

Table 3.1: Normalized correlation functions and refractive-index power spectra of bio-tissues. (From Ref. [46])

	Normalized correlation function	Power spectrum	α
1D	$C(x) = \frac{2}{\Gamma(\alpha-\frac{1}{2})}\left(\frac{x}{2L}\right)^{\alpha-\frac{1}{2}}K_{\alpha-\frac{1}{2}}\left(\frac{x}{L}\right)$	$\Phi_n(\kappa) = \frac{2\sqrt{\pi}\sigma^2 L_0\Gamma(\alpha)}{\Gamma(\alpha-\frac{1}{2})(1+\kappa^2 L_0^2)^\alpha}$	$0.5 < \alpha < 1$
2D	$C(\rho) = \frac{2}{\Gamma(\alpha-1)}\left(\frac{\rho}{2L}\right)^{\alpha-1}K_{\alpha-1}\left(\frac{\rho}{L}\right)$	$\Phi_n(\kappa) = \frac{4\pi\sigma^2 L_0^2(\alpha-1)}{(1+\kappa^2 L_0^2)^\alpha}$	$1 < \alpha < 1.5$
3D	$C(r) = \frac{2}{\Gamma(\alpha-\frac{3}{2})}\left(\frac{r}{2L}\right)^{\alpha-\frac{3}{2}}K_{\alpha-\frac{3}{2}}\left(\frac{r}{L}\right)$	$\Phi_n(\kappa) = \frac{\sigma^2 L_0^3\Gamma(\alpha)}{\pi^{3/2}\Gamma(\alpha-\frac{3}{2})(1+\kappa^2 L_0^2)^\alpha}$	$1.5 < \alpha < 2$

First, we adopt the 2D power spectrum for biological tissues [41]. Then according to the projection-slice theorem, 1D power spectrum is obtained by integration of the 2D power spectrum along one of the directions [52]. Finally, the 3D power spectrum can be found by the differential relation, $\Phi_n(\kappa) = -dV(\kappa)/(2\pi\kappa d\kappa)$, where $V(\kappa)$ being the 1D power spectrum [9]. The spatial correlation functions are determined by the Fourier transforms of the power spectrum in the corresponding dimensions. All the correlation functions in Table 3.1 are normalized to unity at the coinciding arguments.

3.1.3 Scintillation index of plane and spherical waves

In section 1.4, we have introduced the general expressions governing the scintillation index of an optical wave in a random, turbulent-like medium. For a plane wave, on substituting the 3D power spectrum in Table 3.1 into Eq. (1.33), with $t = \kappa^2 L_0^2$, the scintillation for a plane wave becomes,

$$\sigma_I^2(0, L) = \frac{4\sqrt{\pi}k^2 L\sigma^2 L_0\Gamma(\alpha)}{\Gamma(\alpha - 3/2)}\left[\frac{1}{\alpha-1} - \frac{kL_0^2}{L}\int_0^\infty \frac{1}{t(1+t)^\alpha}\sin\left(\frac{Lt}{L_0^2 k}\right)dt\right]. \quad (3.1)$$

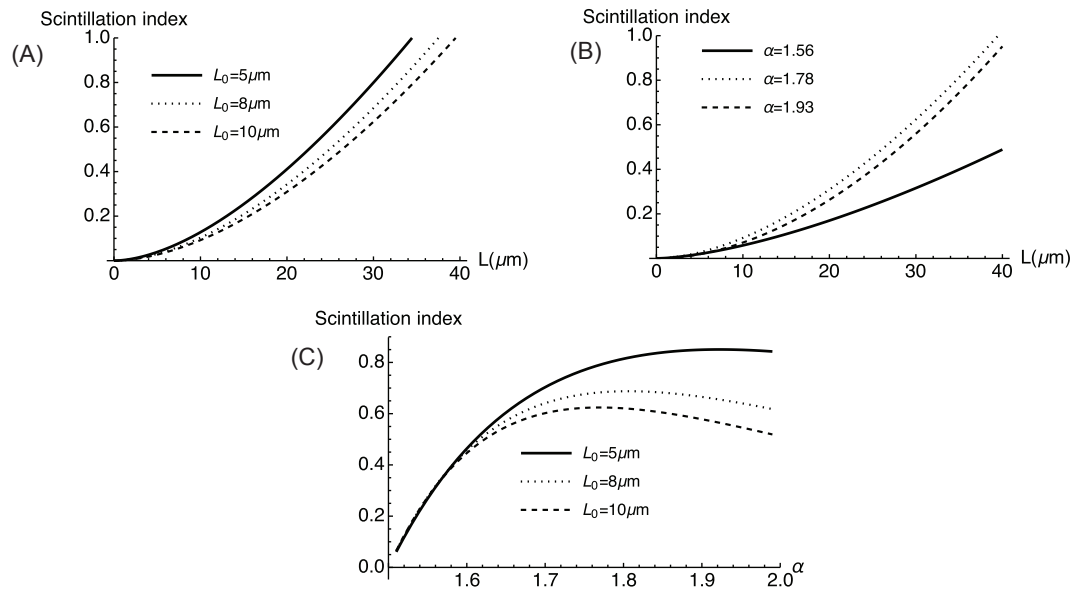Figure 3.1: Rytov variance: (a) $\alpha = 1.78$; (b) $L_0 = 10\mu m$; (c) $L = 30\mu m$. (From Ref. [46])

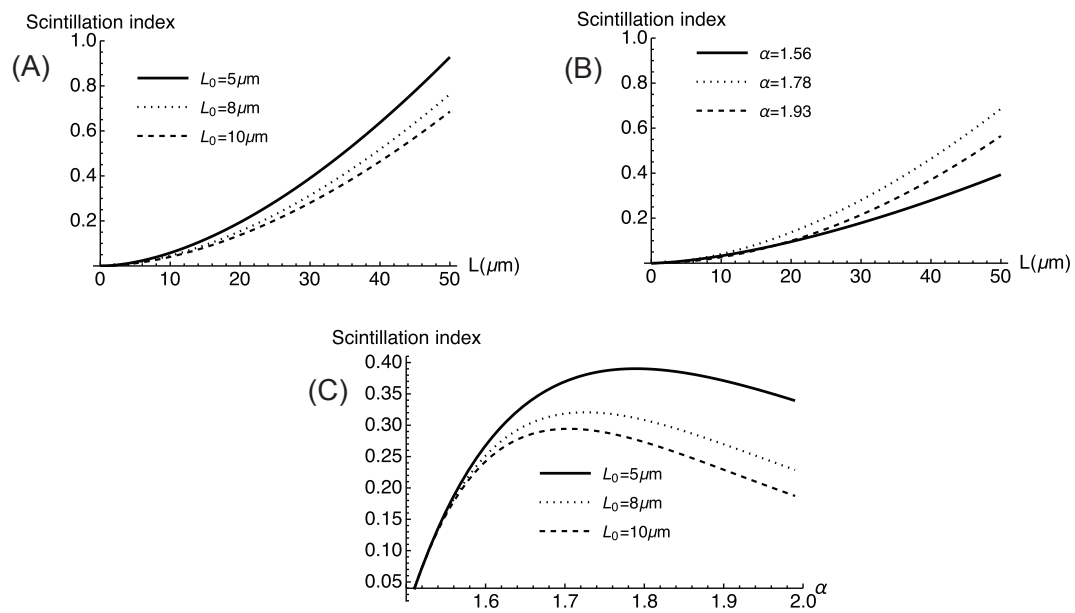Figure 3.2: Scintillation index of spherical wave: (a) $\alpha = 1.78$; (b) $L_0 = 10\mu m$; (c) $L = 30\mu m$. (From Ref. [46])

This integral does not have analytical solution, hence we will present the numeral calculation results. The fixed parameters for the following examples are: $\lambda = 1.55\mu m$, $\sigma^2 = 5 \times 10^{-4}$. Figure 3.1 shows the Rytov variance dependence on propagation distance L in (a) and (b); dependence on power law constant α in (c). It illustrates that the Rytov variance increases really fast, resulting in that the weak regime of tissue refractive index fluctuations is limited to only several tens of microns. This implies that the refractive ability of tissue driven by the large scales diminishes at this range and scattering-like effects caused by small scales become dominant.

For the spherical incident wave $\Lambda = 0$ and $\Theta = 0$, therefore, the radial part σ_r vanishes and the longitudinal part becomes

$$
\sigma_l^2(0, L) = \frac{8\sqrt{\pi}k^2 L\sigma^2 L_0^3 \Gamma(\alpha)}{\Gamma(\alpha - 3/2)} \left[\frac{1}{2L^2(\alpha - 1)} \right.
$$
$$
\left. - \int_0^1 \int_0^\infty \frac{\kappa}{(1 + \kappa^2 L_0^2)^\alpha} \cos[L\kappa^2 \xi(1 - \xi)/k] d\kappa d\xi \right].
$$

(3.2)

Figure 3.2 shows the scintillation index of the spherical wave. Comparing with the results in Fig. 3.1, we can see that the main trends of the scintillation index are the same but its numerical values for the spherical wave are always smaller.

3.1.4 Scintillation index of a Gaussian beam

We will now present the results of the incident Gaussian beam. Figure 3.3 has the same structure as Figs. 3.1 and 3.2. The evolution of the scintillation in bio-tissues is similar because the Gaussian beam reduces to the plane and spherical waves as limiting cases. Moreover, the scintillation index of the Gaussian beam is always between higher values of the plane wave and lower values of the spherical wave.
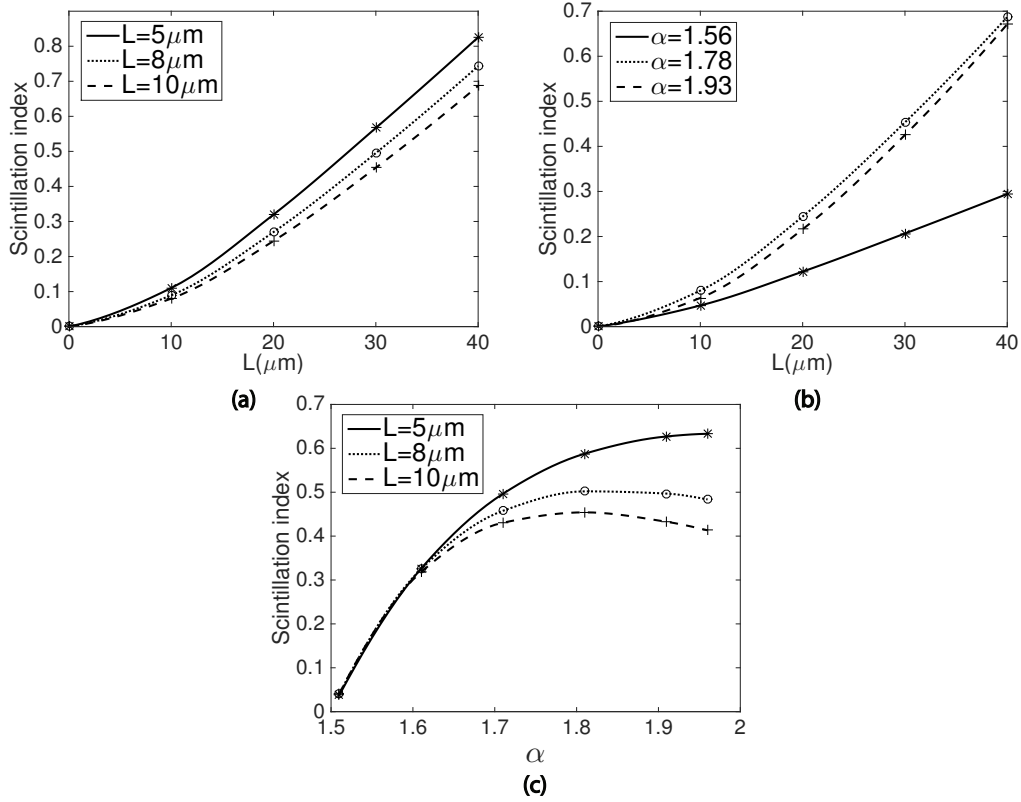
Figure 3.3: On-axis scintillation index of Gaussian incident beam with $F_0 = 10^6 \mu m$, $W_0 = 10\mu m$. (a) $\alpha = 1.78$ (b)$L_0 = 10\mu m$ (c) $L = 30\mu m$. (From Ref. [46])
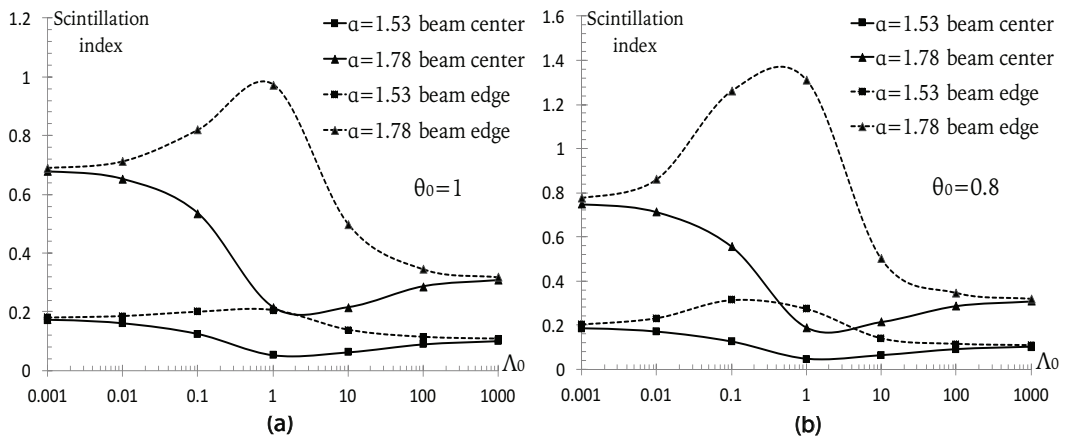

Figure 3.4: scintillation index of Gaussian beam: (a) collimated ($\Theta_0 = 1$), (b) focused ($\Theta_0 = 0.8$), $L = 30\mu m$, $L_0 = 8\mu m$. (From Ref. [46])

Figure 3.4 illustrates the variation of the scintillation index of the Gaussian beam varying with Λ_0, for a collimated beam (a) and a focused beam (b). On the axis of the collimated beam ($r = 0$) the scintillation index attains the minimum at the first Fresnel zone $\Lambda_0 = 1$, while at the diffractive beam edge ($r = W$) it attains its maximum at the first Fresnel zone. In the near field ($\Lambda_0 \ll 1$) and far field ($\Lambda_0 \gg 1$) the scintillation index at the beam edge saturates to constant values. For focused Gaussian beam, when $\alpha = 1.78$, the scintillation index is generally slightly larger but has almost the same trend as that of the collimated beam. However, when $\alpha = 1.53$ the peak of the scintillation index at the beam edge moves to $\Lambda_0 \approx 0.1$.

3.1.5   Conclusion

The power spectra of the refractive index for biological tissues in different dimension have been summarized. Using the second-order Rytov complex phase perturbation theory, we have discussed the scintillation index of plane waves, spherical waves and Gaussian waves propagating in isotropic and homogeneous bio-tissues. Our results provide insight into the interaction process of the waves and the bio-tissues, separating the predominantly refractive-based regime of weak fluctuations from the scattering regime of moderate and strong fluctuations. The threshold between weak and moderate fluctuation regimes is shown to be limited to tens of micrometers for most types of bio-tissues. This study might be of interest in medical imaging and diagnostics.

3.2 Light propagation in soft anisotropic biological tissues

3.2.1 Background

Optical methods of biological tissue analysis have become a significant part in medical diagnostics and treatments nowadays [53]- [55]. Quasi-elastic light scattering [56], optical coherence tomography [57], Mueller matrix polarimetry [58], two-photon fluorescence microscopy [59] are only a few in the variety of well-established methods developed for efficient sensing and imaging of biological structures [60], [61].

In reality, some biological tissues may exhibit anisotropy due to their intrinsic cell composition, for instance, tissues containing fibers, due to external mechanical stresses, or both [62], [63]. There are two types of anisotropy of bio-tissues. One is geometrical anisotropy, causing spectral density of the beam to acquire elliptical shape for sufficiently large propagation distances but not changing the polarimetric content. The other is electromagnetic anisotropy, in which the random medium perturbs the electric field components differently and may couple them, resulting in the loss of the degree of polarization [64] - [67].

In this section we first introduce the geometrical anisotropic power spectrum for soft biological tissues. Then we apply the extended Huygens-Fresnel integral [9] for wide-sense stationary light beam propagation in tissues with such power spectra. In particular, we assume that the beam is generated by a scalar isotropic Gaussian Schell-model source [68] and analyze the effects of anisotropic tissues for two source properties: the root-mean-square (r.m.s.) width and the r.m.s. correlation width [69].
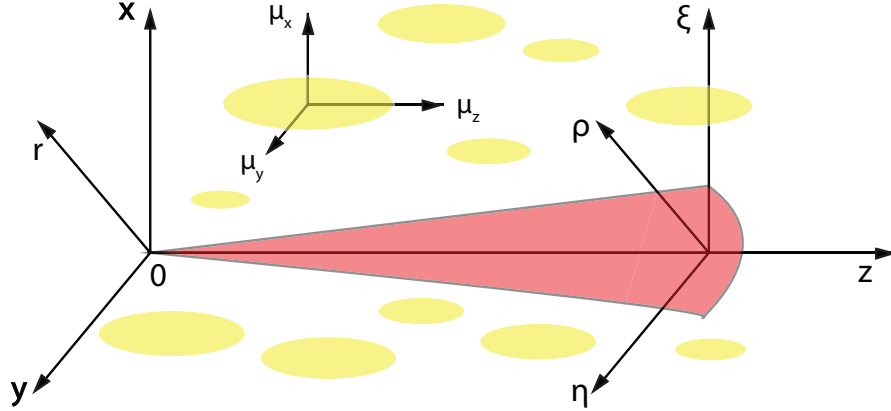
Figure 3.5: Illustration of beam propagation in biological tissues. (From Ref. [69])

3.2.2 GSM beam propagation in anisotropic biological tissues

Suppose that a scalar, Gaussian Schell-Model (GSM) light beam is incident on a soft anisotropic biological tissue with anisotropy factors $\mu_x = \mu_z \neq \mu_y$ in the plane $z = 0$ and propagates through it into the positive half-space $z > 0$ (see Fig. 3.5). The cross-spectral density of the GSM beam has the expression [68]

$$W^{(0)}(\mathbf{r}_1, \mathbf{r}_2; \omega) = \exp\left(-\frac{\mathbf{r}_1^2 + \mathbf{r}_2^2}{4\sigma_0^2}\right) \exp\left(-\frac{|\mathbf{r}_2 - \mathbf{r}_1|^2}{2\delta_0^2}\right), \tag{3.3}$$

where $\mathbf{r}_1 \equiv (x_1, y_1)$ and $\mathbf{r}_2 \equiv (x_2, y_2)$ are two position vectors in the source plane and ω is the angular frequency of light; σ_0 and δ_0 denote the initial r.m.s. beam width and the transverse r.m.s. coherence width, respectively. We suppress the dependence of σ_0 and δ_0 on angular frequency ω by assuming that the source is quasi-monochromatic.

The 3D geometrical anisotropic power spectrum for biological tissues can be justified as

$$\Phi_n(\kappa_x, \kappa_y, 0) = \frac{(2\pi)^3 \sigma_n^2 \mu_x \mu_y \mu_z \exp(-\kappa_x^2/\kappa_{mx}^2 - \kappa_y^2/\kappa_{my}^2)}{\kappa_0^3 (1 + 4\pi^2 \mu_x^2 \kappa_x^2/\kappa_0^2 + 4\pi^2 \mu_y^2 \kappa_y^2/\kappa_0^2)^{\alpha/2}}, \qquad 3 < \alpha < 4. \tag{3.4}$$

Here σ_n^2 is the variance of the refractive index of the bio-tissue, μ_x, μ_y and μ_z are the anisotropic strength coefficients in each direction, $\kappa_m = 2\pi/l_0$, $\kappa_0 = 2\pi/L_0$, l_0 and L_0 being the inner scale and the outer scale of the bio-tissue (both reported in [41]). As mentioned above, the inner scale of a typical bio-tissue is smaller than the wavelength but finite. It was not considered in [41] but is crucial for convergence of the integrals of interest. The smallest micro-structures participating in the scattering process from the soft bio-tissues are organelles, being on the order of 0.2-0.5 μm, i.e. roughly comparable with the half of a typical optical wavelength [42]. Therefore it is plausible to select the values of the inner scale in this range. We use the Markov approximation [9] in power spectrum (3.4), implying the delta-correlated fluctuations in the refractive index at any pair of points along the propagation direction.

Figure 3.6 presents the power spectrum of a typical anisotropic biological tissue from Eq. (3.4) along the x and y directions. The parameters of the bio-tissue are chosen as follows: $\sigma_n = 2 \times 10^{-2}$, $L_0 = 5\mu m$, $l_0 = 0.2\mu m$, $\mu_x = 1$, $\mu_y = 3$, $\mu_z = 1$, $\alpha = 3.5$. We can see the clear discrepancy between the spectral lines in the inertial range, while the two curves merge at both cut-off frequencies, about 0.1 μm^{-1} and 100 μm^{-1}.

In Chapter 1 section 1.5, we have introduced the extended Huygens-Fresnel integral method. On substituting the anisotropic power spectrum Eq. (3.4) into Eq. (1.39), then following the approximation procedure in [70], the complex phase correlation term can be represented as a product of two Cartesian parts:

$$\langle \exp[\Psi^*(\boldsymbol{\rho}_1, \mathbf{r}_1; \omega) + \Psi(\boldsymbol{\rho}_2, \mathbf{r}_2; \omega)] \rangle = \exp\left[-\frac{\pi^2 k^2 zT(\xi_d^2 + \xi_d x_d + x_d^2)}{3\mu_x^2}\right]$$
$$\times \exp\left[-\frac{\pi^2 k^2 zT(\eta_d^2 + \eta_d y_d + y_d^2)}{3\mu_y^2}\right], \tag{3.5}$$
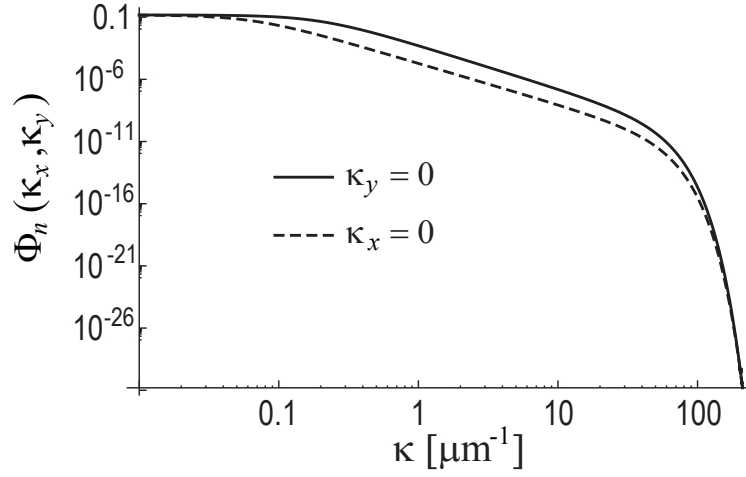
Figure 3.6: Anisotropic power spectrum of refractive index for bio-tissues. (From Ref. [69])

where

$$T = \frac{1}{\mu_x \mu_y} \int\limits_0^\infty \kappa'^3 \Phi'_n(\kappa') d\kappa', \tag{3.6}$$

the adjusted spectrum $\Phi'_n(\kappa')$ is obtained from $\Phi_n(\kappa)$ by changing spatial frequency vector $\boldsymbol{\kappa} = (\kappa_x, \kappa_y)$ to $\boldsymbol{\kappa}' = (\kappa'_x, \kappa'_y)$, where $\kappa'_x = \mu_x \kappa_x$, $\kappa'_y = \mu_y \kappa_y$. The expression is given as

$$\Phi'_n(\kappa') = (2\pi)^3 \sigma_n^2 \mu_x \mu_y \mu_z \frac{\exp\left[-|\kappa'|^2/\kappa_m^2\right]}{\kappa_0^3(1 + 4\pi^2|\kappa'|^2/\kappa_0^2)^{\alpha/2}}. \tag{3.7}$$

Then the term T becomes

$$
\begin{aligned}
T = &\frac{\mu_z \sigma_n^2 \kappa_0}{4\pi(\alpha - 2)} \left[\left(2 + 4\pi^2(\alpha - 2)(\kappa_m/\kappa_0)^2\right)(2\pi)^{2-\alpha}(\kappa_m/\kappa_0)^{2-\alpha} \right.\\
&\times \left. \exp\left[\kappa_0^2/4\pi^2\kappa_m^2\right]\Gamma\left(2 - \frac{\alpha}{2}, (2\pi\kappa_m/\kappa_0)^{-2}\right) - 2 \right],
\end{aligned}
\tag{3.8}
$$

where $\Gamma(\cdot, \cdot)$ is an incomplete Gamma function. Finally, on substituting from Eqs. (1.37), (3.5), and (3.8) into Eq. (1.36) we find that

$$W(\boldsymbol{\rho}_1, \boldsymbol{\rho}_2, z) = W_x(\xi_1, \xi_2) W_y(\eta_1, \eta_2), \tag{3.9}$$

with

$$W_x(\xi_1, \xi_2) = \frac{1}{\sqrt{\triangle_x(z)}} \exp(-\frac{\xi_1^2 + \xi_2^2}{4\sigma_0^2 \triangle_x(z)}) \exp(-\frac{ik(\xi_1^2 - \xi_2^2)}{2R_x(z)})$$

$$\times \exp\left[-\left(\frac{1}{2\delta_0^2 \triangle_x(z)} + \frac{\pi^2 k^2 Tz}{3\mu_x^2}\left(1 + \frac{2}{\triangle_x(z)}\right) - \frac{\pi^4 k^2 T^2 z^4}{18\mu_x^4 \triangle_x(z)\sigma_0^2} \right)(\xi_1 - \xi_2)^2 \right]$$

$$(3.10)$$

and

$$\triangle_x(z) = 1 + \left[\frac{1}{4k^2\sigma_0^4} + \frac{1}{k^2\sigma_0^2}\left(\frac{1}{\delta_0^2} + \frac{2\pi^2 k^2 Tz}{3\mu_x^2} \right) \right] z^2,$$

$$R_x(z) = z + \frac{\sigma_0^2 z - \pi^2 T z^4/3\mu_x^2}{(\triangle_x(z) - 1)\sigma_0^2 + \pi^2 T z^3/3\mu_x^2}.$$

$$(3.11)$$

Factor $W_y(\eta_1, \eta_2)$ has the same form as $W_x(\xi_1, \xi_2)$.

3.2.3 Numerical examples

We will now discuss two aspects of the beam-tissue interaction problem based on numerical calculations. First, we analyze how various bio-tissues change the statistics of light on propagation. We will use different values of power-spectrum parameters to characterize the bio-tissues: the variance of the refractive index σ_n^2, the ratio of the anisotropic factors along the x and y axes, μ_x/μ_y, and the slope α in the inertial range. On the other hand, we will explore how light beams radiated by sources with different properties, such as the initial r.m.s. beam width, σ_0, and the initial coherence width, δ_0, evolve on passing through the same tissue. For all the examples below the numerical values of parameters are selected to be: $\sigma_0 = 3mm$, $\sigma_n^2 = 4 \times 10^{-4}$, $\lambda = 0.6328\mu m$, $L_0 = 5\mu m$, $l_0 = 0.2\mu m$, $\mu_x = 1$, $\mu_y = 3$, $\mu_z = 1$, $\alpha = 3.5$, unless different values are specified in figure captions.
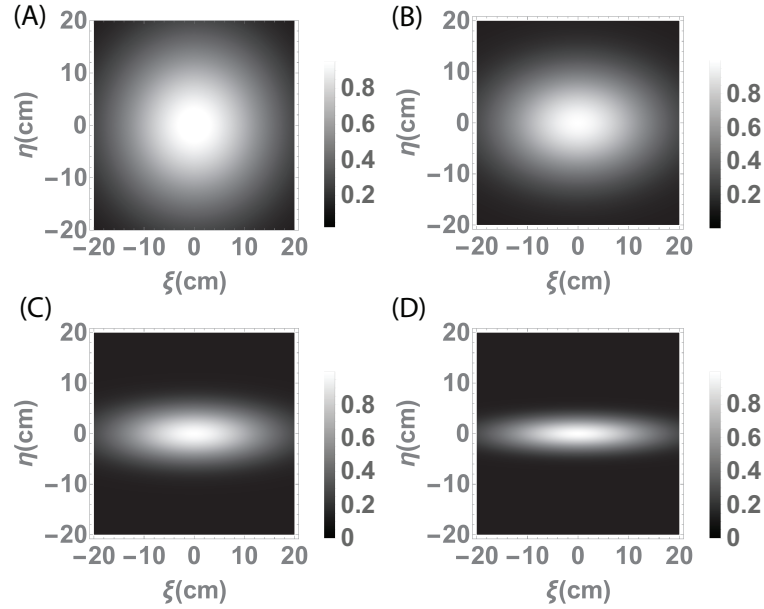
Figure 3.7: Spectral density of the coherent GSM beam ($\delta_0 = \infty$) propagating in the bio-tissue at $z = 1\text{cm}$ with different anisotropy ratios: (A) $\mu_x/\mu_y = 1 : 1$; (B) $\mu_x/\mu_y = 1 : 1.5$, (C) $\mu_x/\mu_y = 1 : 3$, (D) $\mu_x/\mu_y = 1 : 5$. (From Ref. [69])

Figure 3.8: Spectral density of the coherent GSM beam ($\delta_0 = \infty$) at $z = 1mm$ with different α (A) $\alpha = 3.1$, (B) $\alpha = 3.3$, (C) $\alpha = 3.6$, (D) $\alpha = 3.9$. (From Ref. [69])

Figure 3.7 presents the effect of different anisotropic factors on spectral density at a large enough propagation distance from the source (say, 1 cm). As expected, the smaller ratio μ_x/μ_y, i.e. the stronger anisotropy of the tissue results in the larger ratio of the two semi-axes of the ellipse, approximating such values at sufficiently large distances.

Figure 3.8 illustrates the effect of power spectrum slope, α, on the evolution of spectral density of the beam. Due to the fact that smaller values of α [Figs. 3.8(A), 3.8(B)] redistribute more weight to the smaller inhomogeneities, resulting in more small-scale scattering effects and less refraction-like effects, the spectral density spreads faster along the propagation path and starts to present the elliptical profiles at shorter distances from the source. On the other hand, larger values of α[Figs. 3.8(C), 3.8(D)] correspond to the refraction-like effects on the beam and therefore its spectral density preserves its source plane profile for larger ranges.

Figure 3.9 demonstrates the effect of initial beam width on the spectral density of the beam. It is clear that in terms of shape-invariance, initially smaller beams [Fig. 3.9(A), 3.9(B)] are more susceptible to the bio-tissue fluctuations, acquiring ellipse-like profiles, while initially larger beams [Fig. 3.9(C), 3.9(D)] maintain their initial circular profiles much better.

Comparing Eq. (3.9) to Eq. (3.3), the r.m.s. beam width and the r.m.s. coherence width of the GSM source at propagation distance z in bio-tissues are given by the expressions (see also [70]):

$$\sigma_i(z) = \sigma_0\sqrt{\triangle_i(z)} = \sqrt{\sigma_0^2 + \frac{z^2}{4k^2\sigma_0^2} + \frac{z^2}{k^2\delta_0^2} + \frac{2\pi^2 T z^3}{3\mu_i^2}}, \qquad (i = x, y) \qquad (3.12)$$

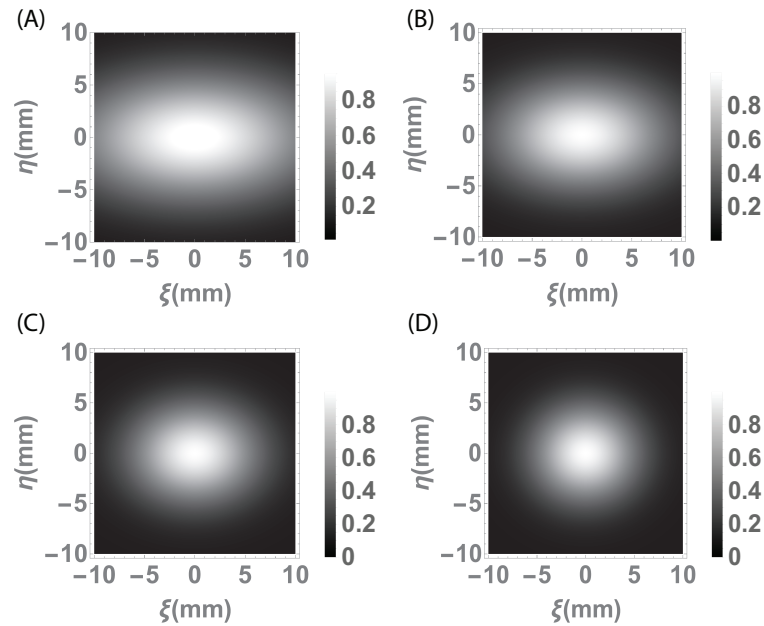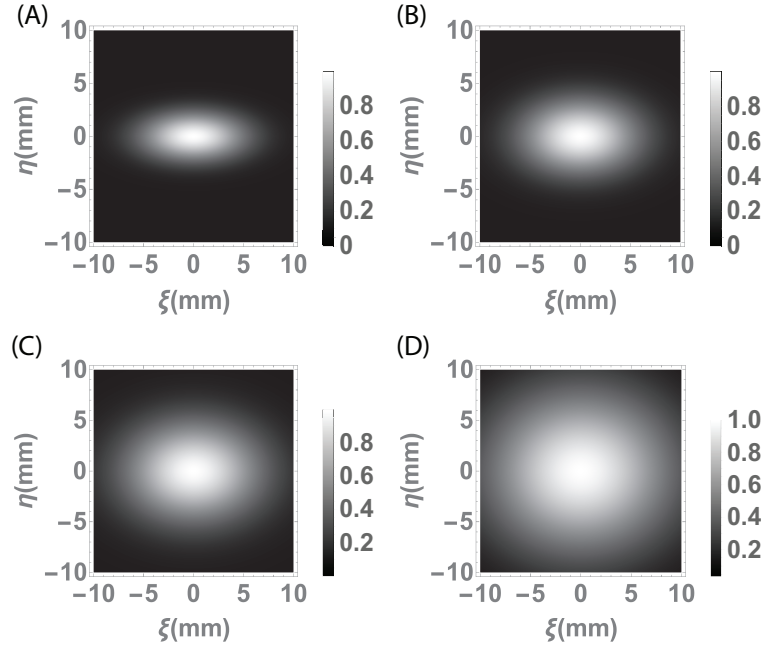Figure 3.9: Spectral density of the coherent GSM beam ($\delta_0 = \infty$) at $z = 1mm$ with different initial beam width (A) $\sigma_0 = 1mm$, (B) $\sigma_0 = 2mm$, (C) $\sigma_0 = 3mm$, (D) $\sigma_0 = 5mm$. (From Ref. [69])

$$\delta_i(z) = \left[\frac{1}{\delta_0^2 \triangle_i(z)} + \frac{2\pi^2 k^2 T z}{3\mu_i^2} + \frac{2\pi^2 k^2 T z}{3\mu_i^2 \triangle_i(z)} \left(2 - \frac{\pi^2 T z^3}{6\mu_i^2 \sigma_0^2} \right) \right]^{-\frac{1}{2}}, (i = x, y) \qquad (3.13)$$

Figure 3.10 represents the effects of bio-tissue parameters on the evolution of the

r.m.s. beam widths σ_i, $(i = x, y)$ of coherent GSM beams calculated from Eq. (3.12)

for a fixed ratio of anisotropic factors $\mu_x/\mu_y = 1/3$. Fig.3.10(A) presents the effects

due to different values of the local strength of fluctuations, σ_n^2 taken from Ref. [55]. It

is clear that larger values of σ_n^2 lead to a larger discrepancy between the beam widths

along the x and y directions, and more so at larger distances from the source. Fig.

3.10(B) illustrates the effect of the slope α of bio-tissue power spectrum on the beam

spreading. Smaller values of α result in larger beam expansion. Fig. 3.10(C) and

(D) show the influence of the outer scale L_0 and the inner l_0 of the power spectrum

on the beam expansion. We can find that the inner scale of the spectrum has bigger
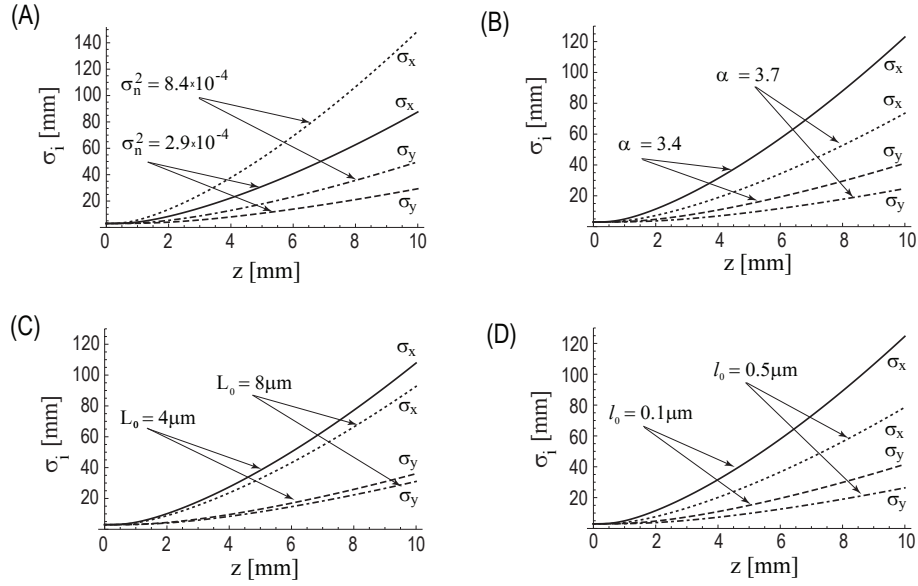
Figure 3.10: The r.m.s. beam widths σ_i, $(i = x, y)$ of the coherent GSM beam $(\delta_0 = \infty)$ vs. propagation distance z. (From Ref. [69])

effects on the expansion rates than the outer scales. Bio-tissues with smaller inner scales l_0 indicating finer structures contribute stronger scattering effects on the beam, resulting in a larger expansion rate. Tissues with larger outer scales L_0 introduce slightly smaller expansion rate. It might be explained by the increasing effective correlation length of refractive index due to the larger outer scales of bio-tissues.

Figure 3.11 explores the effects of source coherence on the beam spread and on the evolving coherence state. In Fig. 3.11, σ_i and δ_i, $(i = x, y)$ are calculated from Eqs. (3.12) and (3.13), for fairly coherent source [Fig. 3.11(A) and 3.11(B)] with δ_0 on the order of the source width and for nearly incoherent source [Fig. 3.11(C) and 3.11(D)] with δ_0 being on the order of the wavelength. It is clear that the beam expansion is the same in both cases, i.e. source coherence does not affect the beam size at all. This is due to the fact that in both cases the source coherence width decreases rapidly with the propagating distance and attains values smaller than the wavelength of light at
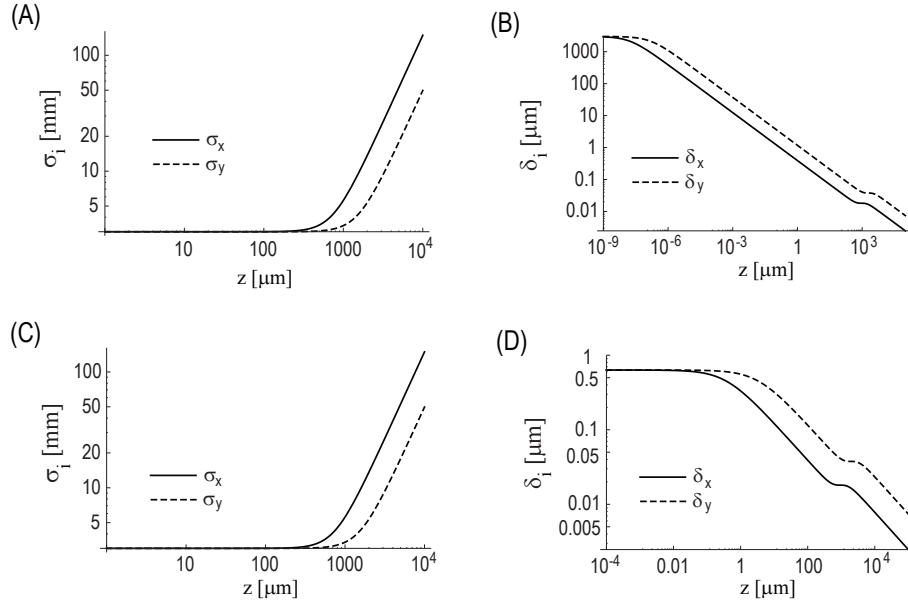
Figure 3.11: (A), (C) σ_i, $(i = x, y)$ and (B), (D) δ_i, $(i = x, y)$ of the GSM beam with (A), (B) $\delta_0 = \sigma_0 = 3mm$; (C), (D) $\delta_0 = \lambda = 0.6328\mu m$, as a function of propagation distance z. (From Ref. [69])

distances as little as several μm from the source. Therefore the width and coherence properties of the beam are dominated by the bio-tissues correlations, in particular by the ratio of the anisotropic factors μ_x/μ_y, as is seen from the two curves emerging in each of the subplots.

3.2.4 Discussion

In spite of the formal similarities between the power spectra of biological tissues with those of turbulent atmosphere and oceans, spatial scales and strength of fluctuations carry two essential distinctions. The variance of refractive index of biological tissues power (around 10^{-4}) is many orders of magnitude stronger than that of the atmosphere ($10^{-13} - 10^{-17}$). Moreover, the inertial range of scales in a soft bio-tissue extends from a fraction of a micron to several microns, compared with millimeters to tens of meters in atmosphere. The small scales in bio-tissues that are comparable

with the light wavelength cause predominantly scattering effects of light. Due to these two features in bio-tissues the parameter T, accounting for the tissue effects on the beam, is in the range from 0.4 to 7.2 mm^{-1} compared with 10^{-17} to $10^{-13} mm^{-1}$ for the atmosphere. The large value of T dominates the beam spreading over the initial coherence state of the beam and furthermore annihilates the coherence state within a tiny propagation distance. This can be examined by analyzing Eq. (3.12). The beam spreading due to the source coherence width δ_0 comes from the third term, due to the bio-tissues arises from the fourth term. On setting these two terms equal, a propagation distance z at which fluctuations of bio-tissues start dominating the beam spreading can be estimated,

$$\frac{z^2}{k^2 \delta_0^2} = \frac{2\pi^2 T z^3}{3\mu_i^2}. \tag{3.14}$$

Solving for z gives:

$$z_c = \frac{3\mu_i^2}{2\pi^2 T k^2 \delta_0^2}, \tag{3.15}$$

for typical values of parameters z_c has sub-micron values. It is also clear that the beam expand in inverse proportion with the anisotropic factors because of the forth term in Eq. (3.12).

3.2.5 Conclusion

Regarding anisotropic biological tissues as statistically stationary random media described by power spectra with different strengths along the two mutually orthogonal directions, we have analyzed the propagation of coherent and partially coherent, scalar light beams. We have applied the extended Huygens-Fresnel method for analytic evaluation of the beam spectral density and its coherence state, within the validity of the Markov approximation.

In conclusion, scattering and diffraction caused by bio-tissues dominate the beam spreading rather than the diffraction due to the initial coherence state of the source. The elliptical beam profiles appear at distances on the order of hundreds of microns to millimeters. Moreover, these effects annihilate the initial coherence state of the source within propagation distance of microns. This is because of the large fluctuation in refractive index and small inertial scales in bio-tissues. The results of this section may be useful in medical diagnostics and optical treatment of anisotropic bio-tissues.

CHAPTER 4

Scalar and Electromagnetic Weak Scattering

4.1 Scalar weak scattering

4.1.1 Background

In 1908 Gustav Mie developed an analytical solutions to Maxwell's equations to describe the scattering of light by homogeneous spherical particles [71]. The predicted scattered intensity of light is fringe-like pattern with several dark concentric circles centered about the optical axis depending on the particle size and transparency. Due to its high accuracy and sensitivity, Mie theory has various applications particularly in particle size analysis, superior to other particle size analysis methods especially with particle sizes from light wavelength to 50 microns.

However, Mie theory is limited to only homogeneous spherical particles. The particles or structures encountered in life are always with more complicated refractive index distributions. Weak scattering theory can deal with these more complex particles under the assumption that the refractive index of the particle is close to that of the surrounding media [3]. The well known application of the weak scattering theory

is diffraction tomography for construction of refractive index distribution for particles from their scattered fields.

The purpose of this section is to explore the light scattering from hollow and semi-hollow 3D potentials with ellipse, cylinder and parallelepiped-like shapes by weak scattering theory under Born approximation. We will analyze the dependence of the scattered angular intensity distribution on the particle size, shape, edge sharpness and the shell's thickness. This study may serve as a fundamental database for scattered field patterns by a variety of hollow and semi-hollow particles with spherical, elliptical, cylindrical, and Cartesian symmetries [72].

4.1.2 Spherically symmetric potentials

We start the analysis from the simplest situation when the hollow semi-hard edge potential is spherically symmetric:

$$
\begin{aligned}
F_{HS}(\mathbf{r};\omega) =& \frac{1}{C_l} \sum_{l=1}^{L} (-1)^{l-1} \binom{L}{l} \\
& \times \left[h_o \exp\left[-l \frac{x^2+y^2+z^2}{2\sigma_o^2} \right] - h_i \exp\left[-l \frac{x^2+y^2+z^2}{2\sigma_i^2} \right] \right],
\end{aligned}
\tag{4.1}
$$

where h_o is the maximum value of the potential, $(h_o - h_i)$ is the minimum value of the potential (at the particle's center) and $h_o > h_i$, σ_o is the radius of the outer edge, $\sigma_i < \sigma_o$, $\sigma_o - \sigma_i$ defines the thickness of the shell and a normalization factor is

$$
C_l = \sum_{l=1}^{L} (-1)^{l-1} \binom{L}{l}.
\tag{4.2}
$$

The finite sum of Gaussian functions with alternating signs is known as Multi-Gaussian, it has been extensively used in optics for modeling of semi-soft structures (apertures, intensity, coherence states, etc.). Multi-Gaussian functions reduce to Gaussian for $L = 1$ and represent hard drop for $L \to \infty$.
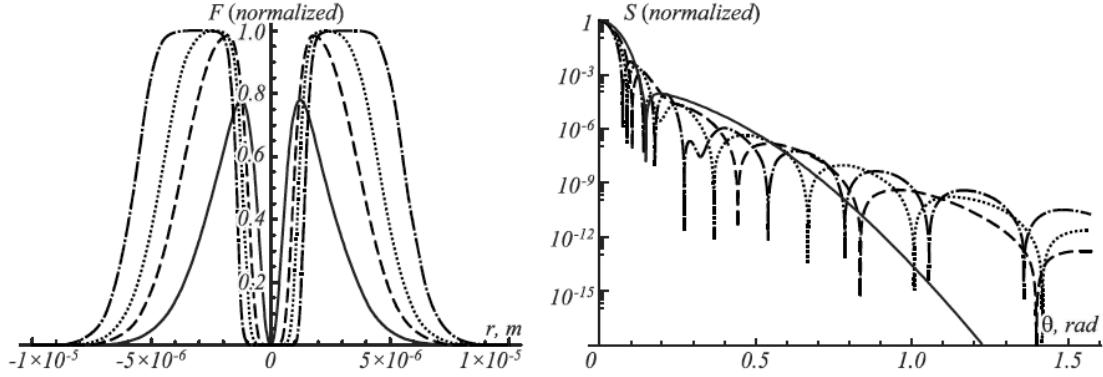
Figure 4.1: The potential and the intensity of the scattered plane wave for $\sigma_o = 20/k$, $\sigma_i = 5/k$, $h_o = h_i = 1$, with $L = 1$ (solid curve), $L = 4$ (dashed curve), $L = 10$ (dotted curve) and $L = 40$ (dash-dotted curve). (From Ref. [72])

In section 1.6, we have introduced the Born approximation weak scattering theory. On substituting the spherical potentials Eq. (4.1) into Eq. (1.42), we can find the scattered field intensity:

$$
\begin{aligned}
S_{HS}^{(s)}(r\mathbf{s};\omega) = \frac{S^{(i)}(\omega)}{r^2} & \left\{ h_o \frac{(2\pi)^{3/2}\sigma_o^3}{C_l} \sum_{l=1}^{L} \frac{(-1)^{l-1}}{l^{3/2}} \binom{L}{l} \right. \\
& \times \exp\left[\frac{-k^2\sigma_o^2}{2l}[(\mathbf{s}_x - \mathbf{s}_{0x})^2 + (\mathbf{s}_y - \mathbf{s}_{0y})^2 + (\mathbf{s}_z - \mathbf{s}_{0z})^2] \right] \\
& - h_i \frac{(2\pi)^{3/2}\sigma_i^3}{C_l} \sum_{l=1}^{L} \frac{(-1)^{l-1}}{l^{3/2}} \binom{L}{l} \exp\left[\frac{-k^2\sigma_i^2}{2l} \right. \\
& \left. \left. \times [(\mathbf{s}_x - \mathbf{s}_{0x})^2 + (\mathbf{s}_y - \mathbf{s}_{0y})^2 + (\mathbf{s}_z - \mathbf{s}_{0z})^2] \right] \right\}^2 .
\end{aligned}
\tag{4.3}
$$

Since the spectral density is non-negative, the following condition must be satisfied,

$$
h_0\sigma_o^3 - h_i\sigma_i^3 \geq 0,
\tag{4.4}
$$

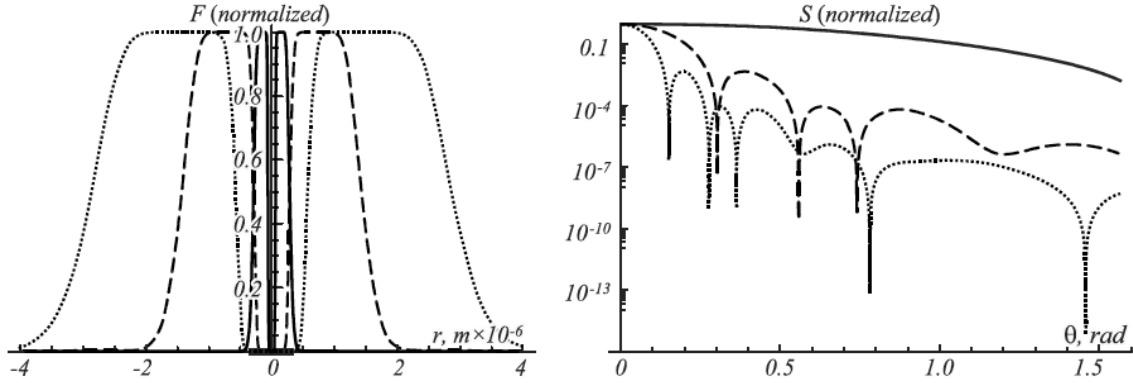which is indeed the case because of inequalities assumed above.

Figure 4.2: The potential and the intensity of the scattered plane wave for $L = 40$ and different sizes: $\sigma_o = 1/k$, $\sigma_i = 0.2/k$ (solid curve); $\sigma_o = 5/k$, $\sigma_i = 1/k$ (dashed curve); and $\sigma_o = 10/k$, $\sigma_i = 2/k$ (dotted curve). (From Ref. [72])

Figures 4.1–4.3 show spherically symmetric potentials F_{HS} for different values of the summation index L, size σ_o, and shell's fill factor and the corresponding scattered intensity distributions. For all the numerical examples we assume that the plane wave with wavelength $\lambda = 632nm$ is incident on scatterers centered at $x = 0$, $y = 0$, and $z = 0$ and $h_o = 1$, along direction $\mathbf{s}_0$ with coordinates $s_{0x} = \sin\theta_0\cos\phi_0$, $s_{0y} = \sin\theta_0\sin\phi_0$, $s_{0z} = \cos\theta_0$, where θ_0 and ϕ_0 are the polar and azimuthal incident angles in the corresponding spherical system. The scattered field is then calculated for a direction specified by a unit vector $\mathbf{s}$ with coordinates $s_x = \sin\theta\cos\phi$, $s_y = \sin\theta\sin\phi$, $s_z = \cos\theta$, where θ and ϕ are the polar and azimuthal scattered angles.

Figure 4.1 presents the effect of different number of terms, L in the summation and the corresponding scattered far fields. As we can see, L controls the edge sharpness in the potential and increases the number of fringes.

Figure 4.2 illustrates the dependence of the scattered intensity on the size of the spherical shell. The selected parameters are $L = 40$, $h_i = 1$ (completely hollow in the
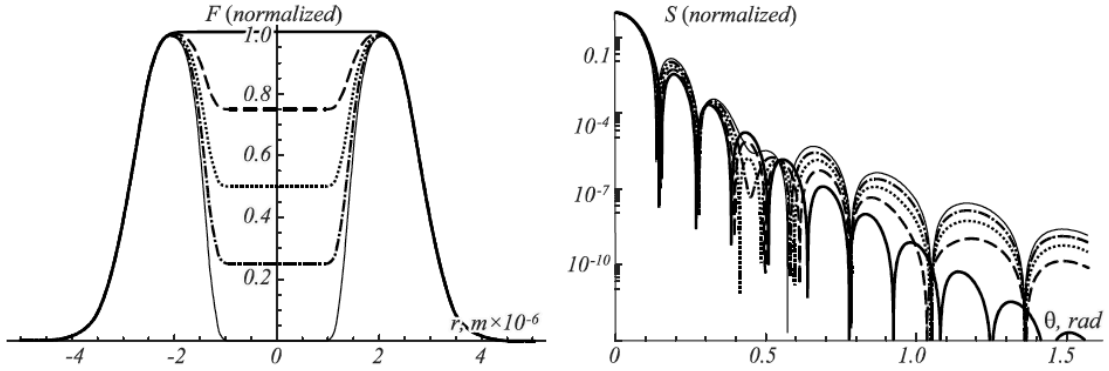
Figure 4.3: The semi-hollow potentials and the corresponding intensity of the plane wave scattered from them for $h_i = 0$ (thick solid curve), $h_i = 0.25$ (dash curve), $h_i = 0.5$ (dotted curve), $h_i = 0.75$ (dashed-dotted curve) and $h_i = 1$ (thin solid curve). (From Ref. [72])

center), and different values of σ_o and σ_i (for all cases $\sigma_o/\sigma_i = 5$). As the size of the shell increases, more fringes in the scattered intensity appear.

Figure 4.3 elucidates the capability of the model to predict the scattered intensity by semi-hollow particles. The hollowness is controlled by the parameter h_i. On fixing $L = 40$, $\sigma_o = 10/k$ and $\sigma_i = 5/k$ and varying h_i from 0 to 1, it can be seen that the number of dark fringes increases as the hollowness decreases.

4.1.3 Hollow ellipsoids

We can construct scattering potential of an ellipsoidal scatterer with adjustable size, thickness, edge softness and fill factor by the distribution:

$$F_{HE}(\mathbf{r};\omega) = \frac{1}{C_l} \sum_{l=1}^{L} (-1)^{l-1} \binom{L}{l} \left\{ h_0 \exp\left[-l \left(\frac{x^2}{2\sigma_{xo}^2} + \frac{y^2}{2\sigma_{yo}^2} + \frac{z^2}{2\sigma_{zo}^2} \right) \right] \right.$$
$$\left. - h_i \exp\left[-l \left(\frac{x^2}{2\sigma_{xi}^2} + \frac{y^2}{2\sigma_{yi}^2} + \frac{z^2}{2\sigma_{zi}^2} \right) \right] \right\}. \tag{4.5}$$

The similar condition must be satisfied because of the nonnegative definite potential and the thickness. So $h_o > h_i$, $\sigma_{xo} > \sigma_{xi}$, $\sigma_{yo} > \sigma_{yi}$, $\sigma_{zo} > \sigma_{zi}$.
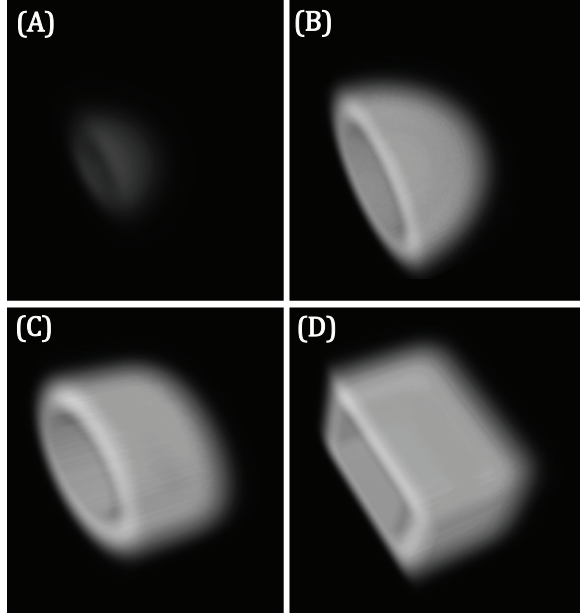
Figure 4.4: Hollow (A) ellipsoid with $L = 1$, (B) ellipsoid with $L = 20$, (C) cylinder with $L = M = 20$ and (D) parallelepiped with $L = M = P = 20$. For all figures $\sigma_{xo} = 1/k$, $\sigma_{yo} = 1.5/k$, $\sigma_{zo} = 2/k$, $\sigma_{xi} = 0.5/k$, $\sigma_{yi} = 1/k$ and $\sigma_{zi} = 1.5/k$. Half-structures are presented for better visualization. (From Ref. [72])

On substituting this expression into Eq. (1.42) one finds that the corresponding far field scattered intensity becomes

$$
S_{HE}^{(s)}(r\mathbf{s}; \omega) = \frac{S^{(i)}(\omega)}{r^2} \Bigg\{ h_o \frac{(2\pi)^{3/2}\sigma_{xo}\sigma_{yo}\sigma_{zo}}{C_l} \times \sum_{l=1}^{L} \frac{(-1)^{l-1}}{l^{3/2}} \binom{L}{l} \exp\Bigg[\frac{-k^2}{2l}(\sigma_{xo}^2(\mathbf{s}_x - \mathbf{s}_{0x})^2
$$

$$
+ \sigma_{yo}^2(\mathbf{s}_y - \mathbf{s}_{0y})^2 + \sigma_{zo}^2(\mathbf{s}_z - \mathbf{s}_{0z})^2) \Bigg] - h_i \frac{(2\pi)^{3/2}\sigma_{xi}\sigma_{yi}\sigma_{zi}}{C_l} \sum_{l=1}^{L} \frac{(-1)^{l-1}}{l^{3/2}} \binom{L}{l}
$$

$$
\times \exp\Bigg[\frac{-k^2}{2l}(\sigma_{xi}^2(\mathbf{s}_x - \mathbf{s}_{0x})^2 + \sigma_{yi}^2(\mathbf{s}_y - \mathbf{s}_{0y})^2 + \sigma_{zi}^2(\mathbf{s}_z - \mathbf{s}_{0z})^2) \Bigg] \Bigg\}^2.
$$

$$(4.6)$$

Similarly the following condition must be satisfied.

$$
h_0 \sigma_{ox}\sigma_{oy}\sigma_{oz} - h_i \sigma_{ix}\sigma_{iy}\sigma_{iz} \geq 0
$$

$$(4.7)$$

This is also automatically satisfied because of the previous conditions.
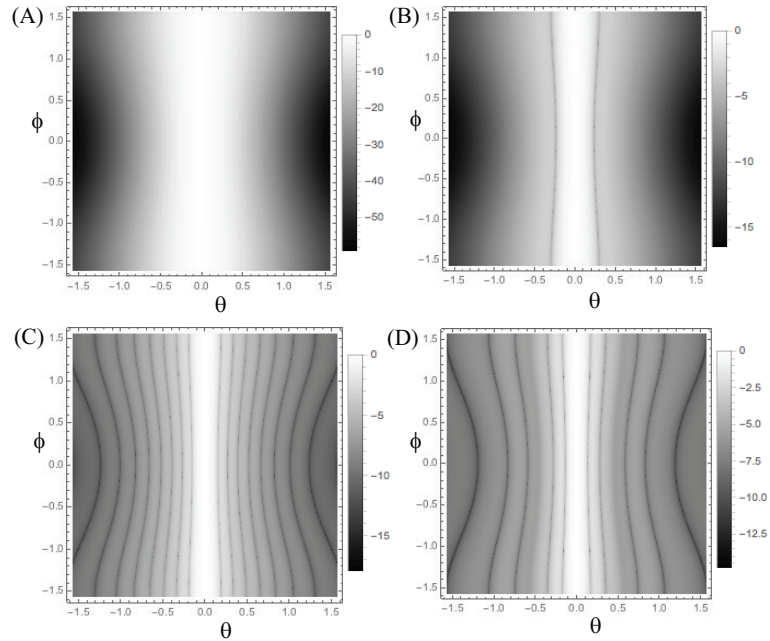
Figure 4.5: Density plots of the scattered intensity of a plane wave from ellipsoidal potentials with $\sigma_{ox} = 10/k$, $\sigma_{oy} = 8/k$, $\sigma_{oz} = 6/k$, $\sigma_{ix} = 5/k$, $\sigma_{iy} = 4/k$, $\sigma_{iz} = 3/k$ and (A) $L = 1$, $h_i = 0$; (B) $L = 1$, $h_i = 1$; (C) $L = 40$, $h_i = 0$ and (D) $L = 40$, $h_i = 1$. (From Ref. [72])

Figures 4.4(A) and 4.4(B) show the hollow elliptical potentials with $L = 1$ and $L = 20$, respectively. Fig. 4.5 presents the density plots of the plane wave scattered by typical ellipsoidal scatterers of fixed size with solid [4.5 (A) and 4.5 (C)] and completely hollow [4.5 (B) and 4.5 (D)] centers. Soft-edge case ($L = 1$, [4.5 (A) and 4.5 (B)]) and fairly hard-edge case ($L = 40$, [4.5 (C) and 4.5 (D)]) are explored. It is clear that the hard-edge case lead to increased number of dark fringes compared with soft-edge. As for the soft-edge case, two dark fringes appear in the center with the hollow potentials. In the hard-edge case, the hollow potentials result in a reduced number of dark fringes compared with solid potentials.

4.1.4 Hollow cylinders

The hollow cylindrical potential can be structured by the subtraction of two products of 2D multi-Gaussian and 1D multi-Gaussian functions. With the cylindrical axis along z direction, the potential takes the form:

$$
\begin{aligned}
F_{HC}(\mathbf{r};\omega) = {} & h_0 \frac{1}{C_l} \sum_{l=1}^{L} (-1)^{l-1} \binom{L}{l} \times \exp\left[-l\left(\frac{x^2}{2\sigma_{xo}^2} + \frac{y^2}{2\sigma_{yo}^2}\right)\right] \\
& \times \frac{1}{C_m} \sum_{m=1}^{M} (-1)^{m-1} \binom{M}{m} \exp\left[-m\frac{z^2}{2\sigma_{zo}^2}\right] \\
& - h_i \frac{1}{C_l} \sum_{l=1}^{L} (-1)^{l-1} \binom{L}{l} \exp\left[-l\left(\frac{x^2}{2\sigma_{xi}^2} + \frac{y^2}{2\sigma_{yi}^2}\right)\right] \\
& \times \frac{1}{C_m} \sum_{m=1}^{M} (-1)^{m-1} \binom{M}{m} \exp\left[-m\frac{z^2}{2\sigma_{zi}^2}\right].
\end{aligned}
\tag{4.8}
$$

The similar condition must be satisfied as before. Here C_m has the same form as C_l in Eq. (4.2) but generally different value of upper index. One can easily model the potential with cylindrical axis along x or y directions by exchanging all the quantities relating to z direction with those relating to x or y directions in Eq. (4.8).

Figure 4.4(C) depicts the hollow cylindrical potential with $L = M = 20$. We note that for $L = M = 1$ the cylinder reduces to the Gaussian shell in Fig. 4.4(A).
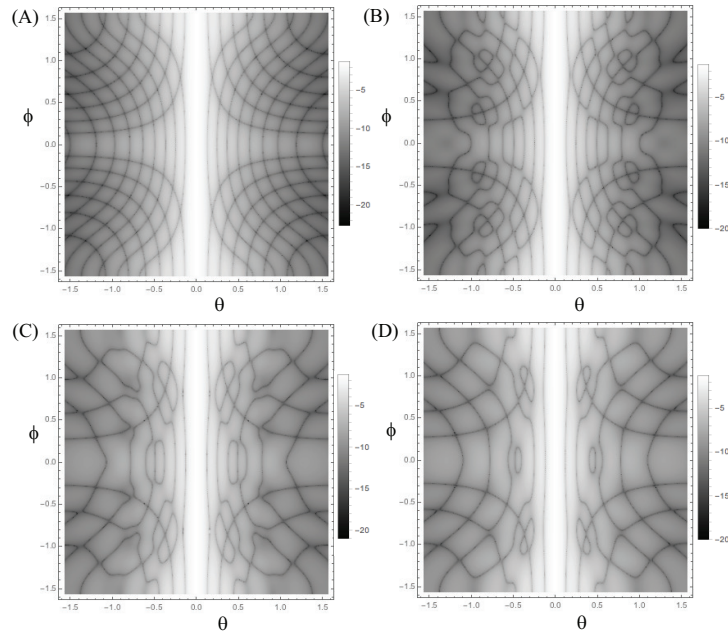
Figure 4.6: Density plots of the far-field intensity of the plane wave scattered from the cylindrical scatterers with symmetry axis along the y-direction (perpendicular to the scattering axis) with $\sigma_{ox} = 10/k$, $\sigma_{oy} = 8/k$, $\sigma_{oz} = 6/k$, $\sigma_{ix} = 5/k$, $\sigma_{iy} = 4/k$, $\sigma_{iz} = 3/k$ for (A) $h_i = 0$ (solid cylinder); (B) $h_i = 0.1$; (C) $h_i = 0.4$; (D) $h_i = 1$ (completely hollow cylinder). (From Ref. [72])

On substituting from Eq. (4.8) into Eq. (1.42), the corresponding far-field scattered intensity is given by:

$$
\begin{aligned}
S_{HC}^{(s)}(r\mathbf{s};\omega) =& \frac{S^{(i)}(\omega)}{r^2}\Bigg\{ h_o \frac{(2\pi)^{3/2}\sigma_{xo}\sigma_{yo}\sigma_{zo}}{C_l C_m} \times \sum_{l=1}^{L} \frac{(-1)^{l-1}}{l}\binom{L}{l} \\
& \times \exp\left[\frac{-k^2}{2l}(\sigma_{xo}^2(\mathbf{s}_x-\mathbf{s}_{0x})^2 + \sigma_{yo}^2(\mathbf{s}_y-\mathbf{s}_{0y})^2)\right] \\
& \times \sum_{m=1}^{M} \frac{(-1)^{m-1}}{\sqrt{m}}\binom{M}{m} \exp\left[\frac{-k^2\sigma_{zo}^2}{2m}(\mathbf{s}_z-\mathbf{s}_{0z})^2\right] \\
& - h_i \frac{(2\pi)^{3/2}\sigma_{xi}\sigma_{yi}\sigma_{zi}}{C_l C_m} \sum_{l=1}^{L} \frac{(-1)^{l-1}}{l}\binom{L}{l} \\
& \times \exp\left[\frac{-k^2}{2l}(\sigma_{xi}^2(\mathbf{s}_x-\mathbf{s}_{0x})^2 + \sigma_{yi}^2(\mathbf{s}_y-\mathbf{s}_{0y})^2)\right] \\
& \times \sum_{m=1}^{M} \frac{(-1)^{m-1}}{\sqrt{m}}\binom{M}{m} \exp\left[\frac{-k^2\sigma_{zi}^2}{2m}(\mathbf{s}_z-\mathbf{s}_{0z})^2\right]\Bigg\}^2
\end{aligned}
\tag{4.9}
$$

Figure 4.6 illustrates the scattered intensity by cylindrical scatterers of different hollowness with cylindrical axis along y direction. It can be seen that the pattern changes qualitatively from solid to completely hollow cylindrical scatterers.

4.1.5   Hollow parallelepipeds

A hollow soft-edge parallelepiped's scattering potential can be modeled by a product of three 1D multi-Gaussian distributions:

$$F_{HP}(\mathbf{r};\omega) = h_0 \frac{1}{C_n} \sum_{n=1}^{N} (-1)^{n-1} \binom{N}{n} \exp\left[-n\frac{x^2}{2\sigma_{xo}^2}\right] \times \frac{1}{C_p} \sum_{p=1}^{P} (-1)^{p-1} \binom{P}{p}$$

$$\exp\left[-p\frac{y^2}{2\sigma_{yo}^2}\right] \times \frac{1}{C_m} \sum_{m=1}^{M} (-1)^{m-1} \binom{M}{m} \exp\left[-m\frac{z^2}{2\sigma_{zo}^2}\right]$$

$$- h_i \frac{1}{C_n} \sum_{n=1}^{N} (-1)^{n-1} \binom{N}{n} \exp\left[-n\frac{x^2}{2\sigma_{xi}^2}\right] \times \frac{1}{C_p} \sum_{p=1}^{P} (-1)^{p-1} \binom{P}{p}$$

$$\exp\left[-p\frac{y^2}{2\sigma_{yi}^2}\right]' \times \frac{1}{C_m} \sum_{m=1}^{M} (-1)^{m-1} \binom{M}{m} \exp\left[-m\frac{z^2}{2\sigma_{zi}^2}\right], \tag{4.10}$$

where C_n and C_p have the same form as normalization factor C_l in Eq. (4.2) but may have different values of upper indexes. The similar condition also must be satisfied.

Figure 4.4(D) shows the hollow parallelepiped-like potential with $L = M = P = 20$. Similar to the cylindrical case, for $L = M = P = 1$ the parallelepiped shell reduces to the elliptical soft Gaussian shell in Fig. 4.4(A).

The far-zone scattered intensity distribution can be readily obtained by substituting from Eq. (4.10) into Eq. (1.42):

$$S_{HP}^{(s)}(rs;\omega) = \frac{S^{(i)}(\omega)}{r^2} \left\{ \frac{(2\pi)^{3/2}\sigma_{xo}\sigma_{yo}\sigma_{zo}}{C_n C_p C_m} \times \sum_{n=1}^{N} \frac{(-1)^{n-1}}{\sqrt{n}} \binom{N}{n} \exp\left[\frac{-k^2\sigma_{xo}^2}{2n}(\mathbf{s}_x - \mathbf{s}_{0x})^2\right]\right.$$

$$\times \sum_{p=1}^{P} \frac{(-1)^{p-1}}{\sqrt{p}} \binom{P}{p} \exp\left[\frac{-k^2\sigma_{yo}^2}{2p}(\mathbf{s}_y - \mathbf{s}_{0y})^2\right]$$

$$\times \sum_{m=1}^{M} \frac{(-1)^{m-1}}{\sqrt{m}} \binom{M}{m} \exp\left[\frac{-k^2\sigma_{zo}^2}{2m}(\mathbf{s}_z - \mathbf{s}_{0z})^2\right] - h_i \frac{(2\pi)^{3/2}\sigma_{xi}\sigma_{yi}\sigma_{zi}}{C_n C_p C_m}$$

$$\times \sum_{n=1}^{N} \frac{(-1)^{n-1}}{\sqrt{n}} \binom{N}{n} \exp\left[\frac{-k^2\sigma_{xi}^2}{2n}(\mathbf{s}_x - \mathbf{s}_{0x})^2\right]$$

$$\times \sum_{p=1}^{P} \frac{(-1)^{p-1}}{\sqrt{p}} \binom{P}{p} \exp\left[\frac{-k^2\sigma_{yi}^2}{2p}(\mathbf{s}_y - \mathbf{s}_{0y})^2\right]$$

$$\times \sum_{m=1}^{M} \frac{(-1)^{m-1}}{\sqrt{m}} \binom{M}{m} \exp\left[\frac{-k^2\sigma_{zi}^2}{2m}(\mathbf{s}_z - \mathbf{s}_{0z})^2\right] \right\}^2.$$
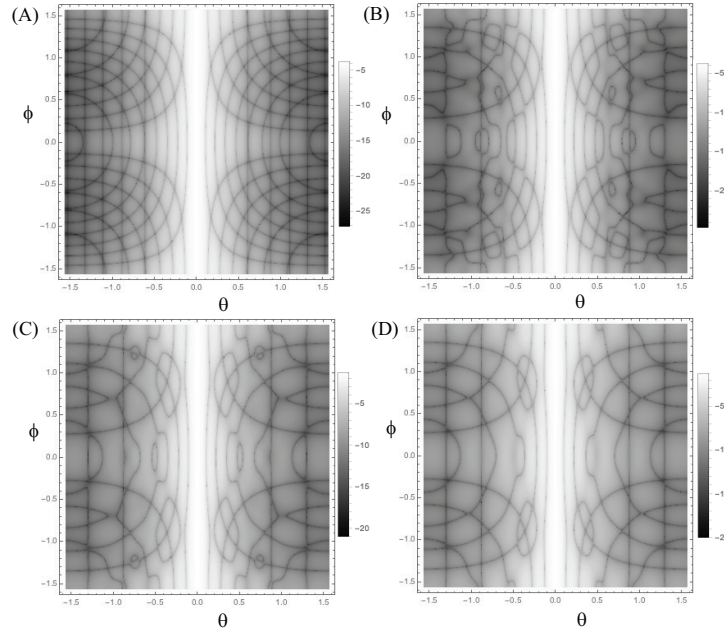
Figure 4.7: Density plots of the far-field intensity of the plane wave scattered from the typical parallelepiped-like scatterers with $\sigma_{ox} = 10/k$, $\sigma_{oy} = 8/k$, $\sigma_{oz} = 6/k$, $\sigma_{ix} = 5/k$, $\sigma_{iy} = 4/k$, $\sigma_{iz} = 3/k$ for (A) $h_i = 0$ (solid parallelepiped); (B) $h_i = 0.1$; (C) $h_i = 0.4$; (D) $h_i = 1$ (completely hollow parallelepiped). (From Ref. [72])

Figure 4.7 presents the scattered intensity for several parallelepiped-like scatterers with different hollowness. Similar to cylindrical cases, the patterns are sensitive to the hollowness of the parallelepiped-like scatterers.

4.1.6 Conclusions

We have established analytical models for the spherical, ellipsoidal, cylindrical and parallelepiped scatterers by means of multi-Gaussian functions of different dimensions. The proposed models have the ability to easily control the size, thickness, hollowness and edge sharpness of the scatterers. Based on weak scattering theory and the first-order Born approximation, we have obtained the analytical expressions for scattered intensities with incident plane waves for all various scatterers. Our results elucidate that far-field intensity distributions are qualitatively distinguishable

with different scatterers accounting for size, thickness, hollowness, edge sharpness and geometrical orientations.

Since the models are entirely based on dimension-separable and easily integrable and transformable Gaussian functions, they can readily serve as a database for all kinds of scatterers, for instance it can be extended to the following cases: 1) A collection of particles with different geometries, 2) Scatterers with different inside and outside profiles, 3) The nested potentials of the same or various geometrical profiles.

4.2 Electromagnetic weak scattering

4.2.1 Background

Stokes parameters are one of the most prominent ways to characterize the polarization of the electromagnetic field. The polarization content of the field can change at various events including propagation, scattering, interference, and interaction with other particles. In the era of rapidly developing technology, real time analysis of the electromagnetic field is in demand. Therefore, it is of great significance to understand the instantaneous Stokes parameters of the electromagnetic field and their corresponding probability.

In this section we will focus on developing the mathematical analysis of the electromagnetic field on weak scattering. In particular, we will derive the Probability Density Functions (PDFs) of the instantaneous Stokes parameters of an electromagnetic, polarized plane wave on scattering from a weak, statistically stationary, homogeneous and isotropic medium of Schell-model type with Gaussian statistics. We

will also study the dependence of the PDFs on the properties of the source and the scatterer [73].

4.2.2 Scattering of the average and instantaneous Stokes vectors

The scattering scenario is illustrated in Fig. 4.8. An electric vector-field $\mathbf{E}^{(i)}(\mathbf{r}') = [E_x^{(i)}(\mathbf{r}'), E_y^{(i)}(\mathbf{r}')]$ is incident on a scatterer occupying domain D at position $\mathbf{r}'$. Here x and y present two mutually orthogonal polarization directions transverse to the optical axis z. Suppose that the field is polychromatic but let us suppress its dependence on frequency for brevity.

The scattering potential of the scatterer is given by

$$F(\mathbf{r}') = \frac{k^2}{4\pi}[n^2(\mathbf{r}') - 1], \tag{4.11}$$

where $n(\mathbf{r}')$ is the refractive index at position $\mathbf{r}'$ within the scatterer, $k = 2\pi/\lambda$, is the wave-number of light, λ being its wavelength in vacuum. Moreover, assume that the potential obeys Gaussian statistics [26] and that the correlation function has the expression

$$C_F(\mathbf{r}'_1, \mathbf{r}'_2) = \langle F^*(\mathbf{r}'_1)F(\mathbf{r}'_2)\rangle, \tag{4.12}$$

where angular brackets denote ensemble average within the scatterer.

In section 1.6, we have introduced the weak scattering theory in electromagnetic case and derived formulas for the scattered electric field components in Cartesian coordinates. Now we will derive the Stokes parameters for the scattered field in spherical coordinates. In spherical coordinates the unit vector $\mathbf{s}$ has components

$$s_x = \sin\theta\cos\phi, \quad s_y = \sin\theta\sin\phi, \quad s_z = \cos\theta, \tag{4.13}$$
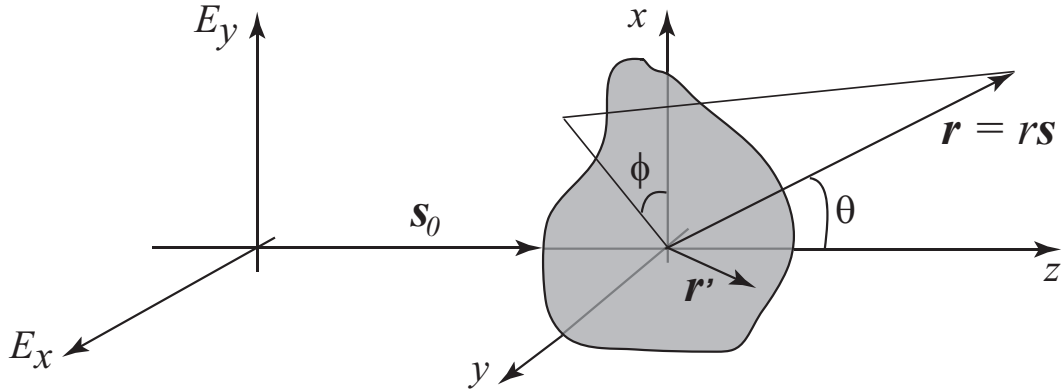
Figure 4.8: Illustration of the notation from the scatterer to the far field.

where θ and ϕ are the polar and azimuthal angles, respectively. In the far zone of the scatterer the field is transverse with respect to scattering direction $\mathbf{s}$ and therefore can be characterized only by the polar and azimuthal components, E_θ and E_ϕ, in the spherical coordinates (see also [74], [76]):

$$E_\theta^{(s)}(r\mathbf{s}) = \cos\theta\cos\phi E_x^{(s)}(r\mathbf{s}) + \cos\theta\sin\phi E_y^{(s)}(r\mathbf{s}) - \sin\theta E_z^{(s)}(r\mathbf{s}),$$
$$E_\phi^{(s)}(r\mathbf{s}) = -\sin\phi E_x^{(s)}(r\mathbf{s}) + \cos\phi E_y^{(s)}(r\mathbf{s}). \tag{4.14}$$

From Eqs. (1.46) and (4.14), the scattered field components in the far zone yield:

$$E_\theta^{(s)}(r\mathbf{s}) = \cos\theta\cos\phi Q_x(r\mathbf{s}) + \cos\theta\sin\phi Q_y(r\mathbf{s}),$$
$$E_\phi^{(s)}(r\mathbf{s}) = -\sin\phi Q_x(r\mathbf{s}) + \cos\phi Q_y(r\mathbf{s}), \tag{4.15}$$

where Q_x and Q_y are given in Eq. (1.47).

In spherical coordinates the average Stokes parameters of the transverse scattered field can be defined as [74]

$$\langle S_0^{(s)}(r\mathbf{s})\rangle = \langle E_\theta^{(s)*}(r\mathbf{s})E_\theta^{(s)}(r\mathbf{s})\rangle + \langle E_\phi^{(s)*}(r\mathbf{s})E_\phi^{(s)}(r\mathbf{s})\rangle, \tag{4.16a}$$

$$\langle S_1^{(s)}(r\mathbf{s})\rangle = \langle E_\theta^{(s)*}(r\mathbf{s})E_\theta^{(s)}(r\mathbf{s})\rangle - \langle E_\phi^{(s)*}(r\mathbf{s})E_\phi^{(s)}(r\mathbf{s})\rangle, \tag{4.16b}$$

$$\langle S_2^{(s)}(r\mathbf{s})\rangle = \langle E_\theta^{(s)*}(r\mathbf{s})E_\phi^{(s)}(r\mathbf{s})\rangle + \langle E_\phi^{(s)*}(r\mathbf{s})E_\theta^{(s)}(r\mathbf{s})\rangle, \tag{4.16c}$$

$$\langle S_3^{(s)}(r\mathbf{s})\rangle = i[\langle E_\phi^{(s)*}(r\mathbf{s})E_\theta^{(s)}(r\mathbf{s})\rangle - \langle E_\theta^{(s)}(r\mathbf{s})E_\phi^{(s)}(r\mathbf{s})\rangle]. \tag{4.16d}$$

On substituting from Eqs. (4.15) into Eqs. (4.16) and applying the far-zone approximation of the Green's function,

$$G(r\mathbf{s}, \mathbf{r}') \approx \frac{\exp[-ik\mathbf{s} \cdot \mathbf{r}' + ikr]}{r}, \tag{4.17}$$

the average scattered Stokes parameters have the expressions

$$\langle S_0^{(s)}(r\mathbf{s})\rangle = (\cos^2\theta + 1)T_0(r\mathbf{s}) - \sin^2\theta\cos 2\phi T_1(r\mathbf{s}) - \sin^2\theta\sin 2\phi T_2(r\mathbf{s}), \tag{4.18a}$$

$$\langle S_1^{(s)}(r\mathbf{s})\rangle = -\sin^2\theta T_0(r\mathbf{s}) + \cos 2\phi(1 + \cos^2\theta)T_1(r\mathbf{s}) + \sin 2\phi(1 + \cos^2\theta)T_2(r\mathbf{s}),$$

$$\tag{4.18b}$$

$$\langle S_2^{(s)}(r\mathbf{s})\rangle = -2\cos\theta\sin 2\phi T_1(r\mathbf{s}) + 2\cos\theta\cos 2\phi T_2(r\mathbf{s}), \tag{4.18c}$$

$$\langle S_3^{(s)}(r\mathbf{s})\rangle = 2cos\theta T_3(r\mathbf{s}), \tag{4.18d}$$

where

$$T_\alpha(r\mathbf{s}) = \frac{1}{2r^2}\int_D\int_D \langle S_\alpha^{(i)}(\mathbf{r}_1', \mathbf{r}_2')\rangle C_F(\mathbf{r}_1', \mathbf{r}_2')\exp[-ik(\mathbf{s}\cdot(\mathbf{r}_2' - \mathbf{r}_1'))]d^3r_1'd^3r_2',$$

$$\tag{4.19}$$

$$(\alpha = 0, 1, 2, 3).$$

Here, $\langle S_\alpha^{(i)}(\mathbf{r}_1', \mathbf{r}_2')\rangle$ is the generalized Stokes parameter, i.e., a parameter defined just like the classic Stokes parameter but depends on a pair of spatial arguments [75].

From Eqs. (4.18)-(4.19), we notice that whereas the Stokes parameter $\langle S_3(r\mathbf{s})\rangle$ of the scattered field depends solely on the corresponding generalized Stokes parameter $\langle S_3^{(i)}(\mathbf{r}_1', \mathbf{r}_2')\rangle$ of the incident field, the other three Stokes parameters have coupled dependence. This is distinct from free-space paraxial propagation where all four parameters are independent on propagation [75].

We define instantaneous Stokes parameters of the scattered far field as [77]

$$S_0^{(s)}(r\mathbf{s}) = E_\theta^{(s)*}(r\mathbf{s})E_\theta^{(s)}(r\mathbf{s}) + E_\phi^{(s)*}(r\mathbf{s})E_\phi^{(s)}(r\mathbf{s}), \tag{4.20a}$$

$$S_1^{(s)}(r\mathbf{s}) = E_\theta^{(s)*}(r\mathbf{s})E_\theta^{(s)}(r\mathbf{s}) - E_\phi^{(s)*}(r\mathbf{s})E_\phi^{(s)}(r\mathbf{s}), \tag{4.20b}$$

$$S_2^{(s)}(r\mathbf{s}) = E_\theta^{(s)*}(r\mathbf{s})E_\phi^{(s)}(r\mathbf{s}) + E_\phi^{(s)*}(r\mathbf{s})E_\theta^{(s)}(r\mathbf{s}), \tag{4.20c}$$

$$S_3^{(s)}(r\mathbf{s}) = i[E_\phi^{(s)*}(r\mathbf{s})E_\theta^{(s)}(r\mathbf{s}) - E_\theta^{(s)}(r\mathbf{s})E_\phi^{(s)}(r\mathbf{s})]. \tag{4.20d}$$

The single-point PDFs of the instantaneous Stokes parameters of the stationary light field governed by Gaussian statistics have been derived in Refs. [78]- [80] and take the forms

$$\begin{aligned}p[S_0^{(s)}(r\mathbf{s})] =&\frac{1}{P^{(s)}(r\mathbf{s})\langle S_0^{(s)}(r\mathbf{s})\rangle}\left\{\exp\left[-\frac{2S_0^{(s)}(r\mathbf{s})}{(1+P^{(s)}(r\mathbf{s}))\langle S_0^{(s)}(r\mathbf{s})\rangle}\right]\right.\\ &\left.-\exp\left[-\frac{2S_0(r\mathbf{s})}{(1-P^{(s)}(r\mathbf{s}))\langle S_0^{(s)}(r\mathbf{s})\rangle}\right]\right\},\end{aligned} \tag{4.21}$$

$$\begin{aligned}p[S_\alpha^{(s)}(r\mathbf{s})] =&\frac{1}{\sqrt{\langle S_0^{(s)}(r\mathbf{s})\rangle^2(1-P^{(s)}(r\mathbf{s})^2)+\langle S_\alpha^{(s)}(r\mathbf{s})\rangle^2}}\\ &\times\exp\left[2\frac{S_\alpha^{(s)}(r\mathbf{s})\langle S_\alpha^{(s)}(r\mathbf{s})\rangle}{\langle S_0^{(s)}(r\mathbf{s})\rangle^2(1-P^{(s)}(r\mathbf{s})^2)}\right]\\ &\times\exp\left[-2\frac{|S_\alpha^{(s)}(r\mathbf{s})|\sqrt{\langle S_0(r\mathbf{s})\rangle^2(1-P^{(s)}(r\mathbf{s})^2)+\langle S_\alpha^{(s)}(r\mathbf{s})\rangle^2}}{\langle S_0^{(s)}(r\mathbf{s})\rangle^2(1-P^{(s)}(r\mathbf{s})^2)}\right]\end{aligned} \tag{4.22}$$

$(\alpha = 1, 2, 3).$

Here, $P^{(s)}(r\mathbf{s})$ is the degree of polarization of the field at a given point defined by

$$P^{(s)}(r\mathbf{s}) = \frac{\sqrt{\langle S_1^{(s)}(r\mathbf{s})\rangle^2 + \langle S_2^{(s)}(r\mathbf{s})\rangle^2 + \langle S_3^{(s)}(r\mathbf{s})\rangle^2}}{\langle S_0^{(s)}(r\mathbf{s})\rangle}. \tag{4.23}$$

It is clear from Eqs. (4.21) - (4.23) that each of the four PDFs is related to all four average Stokes parameters. In particular, even though the average Stokes parameter $\langle S_3 \rangle$ depends only on the corresponding generalized Stokes parameter of the incident field, it is not the case for its PDF, i.e., the PDF is associated with all other three generalized Stokes parameters of the incident field.

4.2.3 An example: polarized plane wave scattered from Gaussian Schell-model medium

Consider a polychromatic, polarized plane wave at position $\mathbf{r}'$,

$$E_\alpha^{(i)}(\mathbf{r}', \mathbf{s}_0) = a_\alpha \exp[ik\mathbf{s}_0 \cdot \mathbf{r}'], \quad (\alpha = x, y), \tag{4.24}$$

incident on the scatterer with direction $\mathbf{s}_0$ along z axis. The amplitude a_i is generally complex. The average Stokes parameters of the incident field then take the form

$$\langle S_0^{(i)}(\mathbf{r}_1', \mathbf{r}_2')\rangle = (A_x^2 + A_y^2) \exp[ik\mathbf{s}_0 \cdot (\mathbf{r}_2' - \mathbf{r}_1')], \tag{4.25a}$$

$$\langle S_1^{(i)}(\mathbf{r}_1', \mathbf{r}_2')\rangle = (A_x^2 - A_y^2) \exp[ik\mathbf{s}_0 \cdot (\mathbf{r}_2' - \mathbf{r}_1')], \tag{4.25b}$$

$$\langle S_2^{(i)}(\mathbf{r}_1', \mathbf{r}_2')\rangle = 2A_x A_y \Re[j_{xy}] \exp[ik\mathbf{s}_0 \cdot (\mathbf{r}_2' - \mathbf{r}_1')], \tag{4.25c}$$

$$\langle S_3^{(i)}(\mathbf{r}_1', \mathbf{r}_2')\rangle = 2A_x A_y \Im[j_{xy}] exp[ik\mathbf{s}_0 \cdot (\mathbf{r}_2' - \mathbf{r}_1')], \tag{4.25d}$$

where $A_x^2 = \langle |a_x|^2 \rangle$, $A_y^2 = \langle |a_y|^2 \rangle$, and

$$j_{xy} = |j_{xy}|e^{i\beta_{xy}} = \frac{\langle a_x^* a_y \rangle}{\sqrt{\langle a_x^2 \rangle \langle a_y^2 \rangle}}, \tag{4.26}$$

where $|j_{xy}| \leq 1$.

Suppose that the correlation function of the scattering potential is Gaussian-Schell model:

$$C_F(\mathbf{r}_1', \mathbf{r}_2') = C_0 \exp\left[-\frac{1}{2\sigma_R^2}\left(\frac{\mathbf{r}_1' + \mathbf{r}_2'}{2}\right)^2\right] \exp\left[-\frac{1}{2\sigma_r^2}\left(\frac{\mathbf{r}_1' - \mathbf{r}_2'}{2}\right)^2\right], \qquad (4.27)$$

where C_0 is the maximum potential strength, σ_R is the r.m.s. potential width and σ_r is the r.m.s. correlation width. We also assume the scatterer is quasi-homogeneous, i.e., $\sigma_R >> \sigma_r$ [81]. On substituting from Eqs. (4.25) and (4.27) into Eqs. (4.18)-(4.19), the average Stokes parameters of the scattered far field yield

$$\langle S_0^{(s)}\rangle(r\mathbf{s}) = \frac{1}{r^2}\left[(\cos^2\theta\cos^2\phi + \sin^2\phi)A_x^2 + (\cos^2\theta\sin^2\phi + \cos^2\phi)A_y^2 \qquad (4.28a)\right.$$
$$\left. - \sin^2\theta\sin 2\phi A_x A_y \Re[j_{xy}]\right]\tilde{C}_F(-\mathbf{K},\mathbf{K}),$$

$$\langle S_1^{(s)}\rangle(r\mathbf{s}) = \frac{1}{r^2}\left[(\cos^2\theta\cos^2\phi - \sin^2\phi)A_x^2 + (\cos^2\theta\sin^2\phi - \cos^2\phi)A_y^2 \qquad (4.28b)\right.$$
$$\left. + \sin 2\phi(1 + \cos^2\theta)A_x A_y \Re[j_{xy}]\right]\tilde{C}_F(-\mathbf{K},\mathbf{K}),$$

$$\langle S_2\rangle^{(s)}(r\mathbf{s}) = \frac{1}{r^2}[\cos\theta\sin 2\phi(A_y^2 - A_x^2) + 2\cos\theta\cos 2\phi A_x A_y \Re[j_{xy}]]\tilde{C}_F(-\mathbf{K},\mathbf{K}),$$
$$(4.28c)$$

$$\langle S_3\rangle^{(s)}(r\mathbf{s}) = \frac{2}{r^2}\cos\theta A_x A_y \Im[j_{xy}]\tilde{C}_F(-\mathbf{K},\mathbf{K}), \qquad (4.28d)$$

where $\tilde{C}_F$ is the Fourier transform of C_F and takes the form

$$\tilde{C}_F(-\mathbf{K},\mathbf{K}) = (2\pi\sigma_R\sigma_r)^3 C_0 \exp\left[-\frac{1}{2}\sigma_r^2 \mathbf{K}^2\right]$$
$$= (2\pi\sigma_R\sigma_r)^3 C_0 \exp\left[-2\sigma_r^2 k^2 \sin^2(\theta/2)\right], \qquad (4.29)$$

with $\mathbf{K} = k(\mathbf{s} - \mathbf{s}_0)$ being the momentum transfer vector.

Further, on substituting from Eqs. (4.28) into the PDFs given by Eqs. (4.21) - (4.23), the distributions of the PDFs for the scattered polychromatic plane wave can
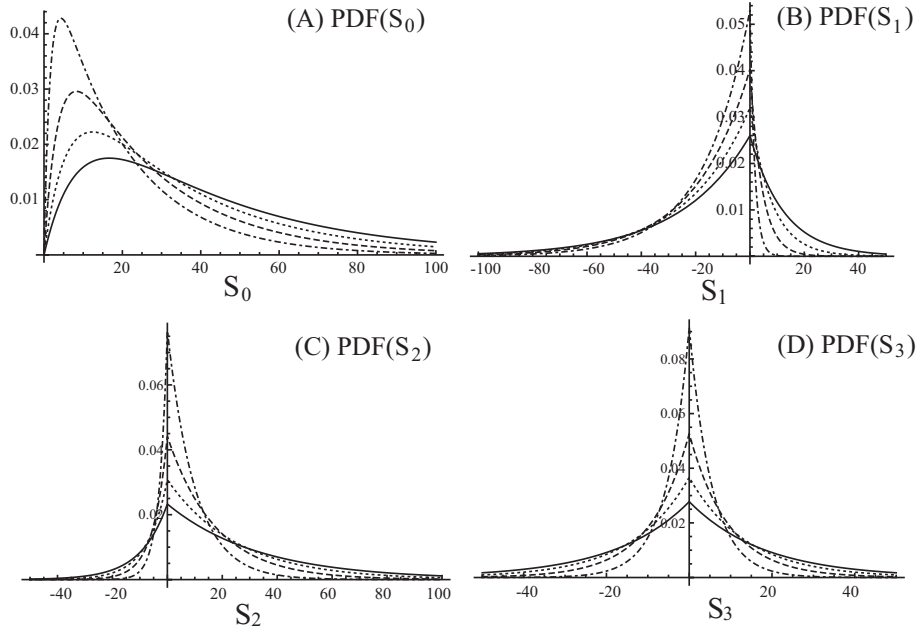
Figure 4.9: The PDFs of the instantaneous Stokes parameters: $\theta = 0$ (solid curve); $\theta = \pi/6$ (dotted curve); $\theta = \pi/4$ (dashed curve) and $\theta = \pi/3$ (dot-dashed curve). (From Ref. [73])

be obtained. The derivation is straightforward but bulky, therefore we will present our results numerically. Unless specified for particular figures, the parameters of the plane wave source and of the scatterer are chosen to be: $\lambda = 0.6328\mu m$, $\sigma_R = 10/k$, $\sigma_r = 1/k$. All the the average Stokes parameters $S_\alpha^{(s)}(r\mathbf{s})$, $(\alpha = 0, 1, 2, 3)$ are normalized by the factor $(2\pi\sigma_R\sigma_r)^3 C_0/r^2$.

Figure 4.9 presents the PDFs of the instantaneous Stokes parameters of the scattered field with different polar angle θ and fixed azimuthal angle $\phi = \pi/3$. It is also supposed that the electric field components are uncorrelated: $j_{xy} = 0$, while $A_x = 6$ and $A_y = 3$. As θ increases, the distributions are generally narrower. This implicates that the polarization states of the scattered field are less stochastic at larger polar angles. The instantaneous Stokes parameter S_0 corresponding to the maximum of PDF$[S_0^{(s)}]$ gradually shifts to smaller values, while those corresponding to the max-
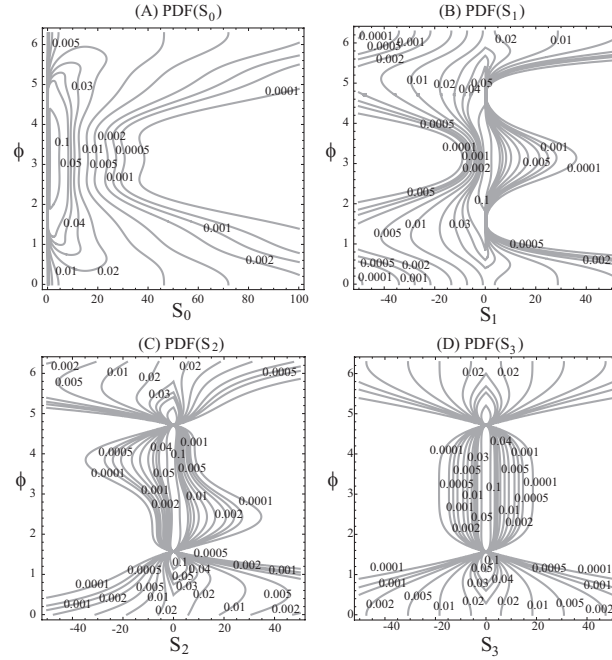
Figure 4.10: Contours of the PDFs of the scattered instantaneous Stokes parameters $\text{PDF}[S_\alpha^{(s)}]$ vs. $S_\alpha^{(s)}$ (horizontal axis) and polar angle ϕ (vertical axis). (From Ref. [73])

imum of $\text{PDF}[S_1^{(s)}]$, $\text{PDF}[S_2^{(s)}]$ and $\text{PDF}[S_3^{(s)}]$ remain zero. Notice that $\text{PDF}[S_3^{(s)}]$ is symmetric about the origin for the uncorrelated field components.

Figure 4.10 illustrates the dependence of the $\text{PDF}[S_\alpha^{(s)}]$ on the azimuthal angle ϕ, with $\theta = 0$. For $\text{PDF}[S_0^{(S)}]$, $\text{PDF}[S_1^{(S)}]$ and $\text{PDF}[S_3^{(S)}]$, we notice that the distributions are symmetric with respect to line $\phi = \pi$, while $\text{PDF}[S_2^{(S)}]$ has rotational symmetric with respect to the the center point corresponding to $S_2 = 0$ and $\phi = \pi$. In adddition, $\text{PDF}[S_3^{(S)}]$ is also symmetric with respect to line $S_3^{(s)} = 0$. It can also be concluded that the distributions for $\text{PDF}[S_0^{(S)}]$ and $\text{PDF}[S_1^{(S)}]$ are sharpest at $\phi = \pi$. However, the distributions for $\text{PDF}[S_2^{(S)}]$ and $\text{PDF}[S_3^{(S)}]$ behave like delta function at $\phi = \pi/2$ and $\phi = 3\pi/2$. This implies that the polarization states of the scattered field are most stable at those azimuthal angles.
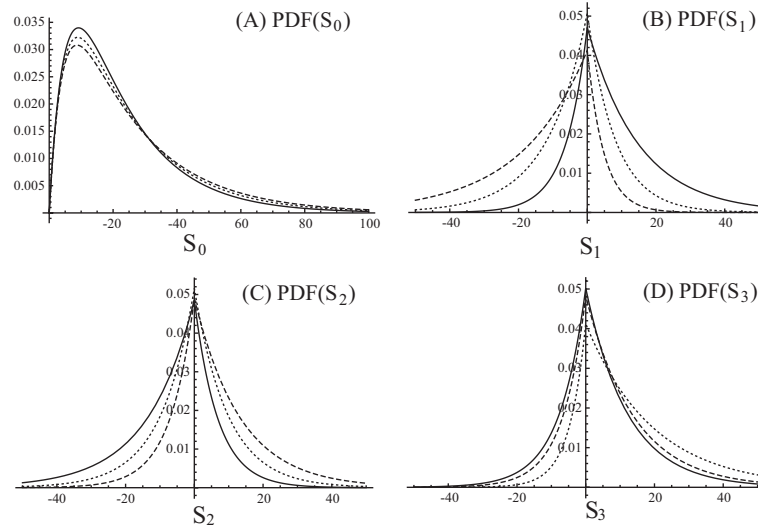
Figure 4.11: The PDFs of the instantaneous Stokes parameters: $j_{xy} = 0.6 \exp(i\pi/10)$ (solid curve); $j_{xy} = 0.6 \exp(i\pi/2)$ (dotted curve); $j_{xy} = 0.6 * \exp(i5\pi/6)$ (dashed curve) with $A_x = A_y = 4$, and $\theta = \pi/6$, $\phi = \pi/3$. (From Ref. [73])

Figure 4.11 compares the PDFs for beams with partially correlated electric field components, with different phases of j_{xy} but the same magnitude of correlation, $|j_{xy}| = 0.6$. This suggests that the incident field is elliptical polarized. It can be seen that different phases of j_{xy} result in different profiles of all the four PDF distributions. This is a surprising result implicating that the PDFs of the instantaneous Stokes parameters can even detect the phase distinctions in the correlation of the incident field components.

Figure 4.12 shows the dependence of PDFs on the r.m.s. correlation width σ_r of the scatterer, at fixed scattering angles $\theta = 0$ and $\phi = \pi/3$. All four distributions acquire sharper profiles as σ_r increases, suggesting that the scatterers with larger correlation length lead to less stochastic scattered field.
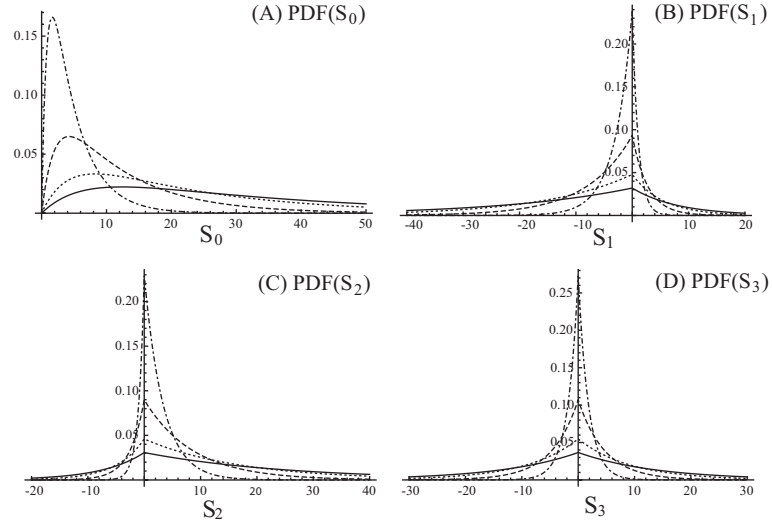
Figure 4.12: The PDFs of the scattered instantaneous Stokes parameters $\mathrm{PDF}[S_\alpha^{(s)}]$ vs. $S_\alpha^{(s)}$ for $\sigma_r = 1/k$ (solid curves); $\sigma_r = 2/k$ (dotted curves); $\sigma_r = 3/k$ (dashed curves); $\sigma_r = 4/k$ (dot-dashed curves). (From Ref. [73])

4.2.4   Conclusions

In this section, the PDFs of the instantaneous Stokes parameters of the scattered field scattered by particles with Gaussian statistics at a single point have been derived analytically. The incident fields can have arbitrary spectrum, coherence and polarization states. As an example, the general expressions have been applied to the case of the incident polychromatic plane wave with different polarization states scattered by a quasi-homogeneous and isotropic scatterer with Gaussian-Schell model.

Our results revealed that the PDFs of the instantaneous Stokes parameters are sensitive to either the variations in incident field or the scatterer. As a result of Cartesian to spherical coordinate system transformation, the average Stokes parameters of the scattered field are coupled to different average Stokes parameters of the incident light, therefore the PDFs of the scattered instantaneous Stokes parameters have a much more complex dependence on the polarization state of the incident light.

The results of this section can be readily extended beyond the quasi-homogeneous regime, to other types of incident radiation and other two-point correlation function of the scattering potential. The general expressions may find applications in light-matter interactions such as biological tissues imaging, material science and thermo-dynamical systems monitoring.

CHAPTER 5

Summary

Various physical and statistical properties of light fundamentally stem from its phase modulation. Coherence, polarization, spectral density distribution etc. are the statistical presentations of the underlying phase distribution of the light source. The phase of light is modulated whenever light-matter interaction occurs including light propagation in media, light scattering and light diffraction. In the mean time, the structured phase of light carries important information about the matter that it interacts with. To retrieve the information from the structured phase of light effectively and accurately is the ultimate goal of imaging and communication systems.

The contribution of this thesis comes from two aspects of phase modulation of light, one is to study active or artificial phase modulation of light leading to novel statistical properties, the other is to explore passive or natural phase modulation of light resulting from scattering or propagation in stationary random media such as biological tissues.

In the respect of active phase modulation of light, we have introduced two methods: sliding function method and coherent mode decomposition method. In the sliding function method, we have focused on the phase structuring of the complex

coherence state of light fields. It has been known for decades that coherence states carry crucial information about a number of observable properties of light, such as the average intensity, spectrum, polarization and angular momentum. We have established a simple theoretical model to design non-trivial complex degree of coherence for 1D and 2D sources with interesting far zone spectral density distributions. The sources developed by this method have the potential in optical trapping, imaging and sensing applications. In the technique of coherent mode decomposition, we have experimentally generated I_m Bessel-correlated beams carrying separable phase with the orbital angular momentum. The simplicity of this method can be potentially used for design and fine tuning of a variety of sources.

Regarding passive phase modulation of light, we included two topics: propagation in biological tissues and scattering from random media. Unlike interaction of atmospheric and oceanic turbulence with optical fields being a well-explored field, soft bio-tissues-light interaction is very little understood. It has been shown that some bio-tissues represent remarkable examples of the turbulent-like system having very well measured power spectra. In order to clarify the continuous light evolution through bio-tissues we have first determined the fundamental ranges at which the transition from weak to strong turbulent regime occurs by considering the scintillation index of the plane and spherical optical waves and a Gaussian beam. Secondly, we have predicted evolution of deterministic and random light beams in isotropic and anisotropic (geometrically, not electromagnetically) soft bio-tissues and, in particular, showed the direction and the extent of the average intensity deformation caused by diffusion with and without anisotropy. We have also illustrated that due to the turbu-

lent scale range limited by several microns the propagation in bio-tissue is practically insensitive to the coherence state of the illumination.

In the second topic of passive phase modulation, we have investigated the expansion of the sphere-based Mie scattering (weak regime only) to other 3D potentials, including their shapes (ellipsoids, cylinders, parallelepipeds), edge sharpness and arbitrary fill factor. Such generalization has become possible because of the tractable mathematical model that we have introduced for the scattering potentials expressed in terms of finite series of alternating Gaussian functions. We have found that for non-spherical scatterers the scattering patterns are not sequences of dark rings but rather a complex net of dark curves depending on the scatterers properties. The other contribution was in analytical calculation of the probability density functions (PDFs) of the instantaneous Stokes parameters on scattering of an electromagnetic plane wave. We have shown the effect of the polarization state of the (deterministic) incident light on the far-field scattered distribution of the polarization states for the only type of scatterer (Gaussian single-point statistics and Gaussian two-point correlation function) for which the exact expressions for the PDFs can be obtained. In both studies the refractive index distribution within the scattering volume affects the phase content of the incident light resulting in structuring of the far-field scattered patterns.

We envision that the results presented in this thesis, being fundamental in nature, will generally find applications in imaging, communication and sensing systems. In particular, we believe that currently emerging techniques in bio-photonics, for instance, quantitative phase tomography and microscopy will benefit from our findings.

Bibliography

[1] L. Mandel and E. Wolf, *Optical Coherence and Quantum Optics*, (Cambridge University Press, 1995).

[2] F. Gori and M. Santarsiero, Opt. Lett. 32, 3531–3533 (2007).

[3] M. Born and E. Wolf, *Principles of Optics*, (7th edition, Cambridge University Press, 1999).

[4] C. J. Chang-Hasnain et al., "Dynamic, polarization, and transverse mode characteristics of vertical cavity surface emitting lasers", IEEE J. Quantum Electronics 27, 6 (1991).

[5] T. Shirai et al., "Mode analysis of spreading of partially coherent beams propagating through atmospheric turbulence", J. Opt. Soc. Am. A 20, 1094-1102 (2003).

[6] J. Li and O. Korotkova, "Deterministic mode representation of random stationary media for scattering problems", J. Opt. Soc. Am. A 34, 1021-1028 (2017).

[7] M. S. Soskin et al, "Topological charge and angular momentum of light beams carrying optical vortices", Phys. Rev. A 56, 4064-4075 (1997).

[8] S. A. Ponomarenko, "A class of partially coherent beams carrying optical vortices", J. Opt. Soc. Am. A 18, 150-156 (2001).

[9] L. C. Andrews and R. L. Phillips, Laser beam propagation through random medium, 2nd ed. (SPIE Press. Bellington, WA, 2005).

[10] O. Korotkova, L. C. Andrews, R. L. Phillips, "A model for a partially coherent Gaussian beam in atmospheric turbulence with applications for lasercom and LIDAR systems", Opt. Eng. 43, 330-341 (2004).

[11] O. Korotkova, N. Farwell and E. Shchepakina, "Light scintillation in oceanic turbulence", Waves in Random and Complex Media 22, 260-266 (2012).

[12] O. Korotkova, "Design of weak scattering media for controllable light scattering", Opt. Lett. 40, 284-287 (2015).

[13] T. Kim et al., "White-light diffraction tomography of unlabelled live cells", Nature Photonics 8, 256-263 (2014).

[14] G. Gbur and T. D. Visser, "Coherence vortices in partially coherent beams", Opt. Commun. 222, 117-125 (2003).

[15] E. Wolf, "Solution of the phase problem in the theory of structure determination of crystals from X-ray diffraction experiments", Phys. Rev. Lett. 103, 075501 (2009).

[16] G. Popescu, *Quantitative Phase Imaging of Cells and Tissues*, (McGraw-Hill, 2011).

[17] S. Divitt and L. Novotny, "Spatial coherence of sunlight and its implications for light management in photovoltaics", Optica 2, 95-103 (2015).

[18] S. Sahin and O. Korotkova, "Light sources generating far fields with tunable flat profiles", Opt. Lett. 37, 2970-2972 (2012).

[19] F. Wang, J. Li, G. Martinez-Piedra, and O. Korotkova, "Propagation dynamics of partially coherent crescent-like optical beams in free space and turbulent atmosphere", Opt. Express 25, 26055-26066 (2017).

[20] R. Simon and N. Mukunda, "Twisted Gaussian Schell-model beams", J. Opt. Soc. Am. A 10, 95-109 (1993).

[21] C. Ding, M. Koivurova, J. Turunen and L. Pan, "Temporal self-splitting of optical pulses", Phys. Rev. A 97, 053838 (2018).

[22] O. Korotkova, X. Chen, "Phase structuring of complex degree of coherence", Opt. Lett. 43, 4727-4730 (2018).

[23] X. Chen, O. Korotkova, "Phase structuring of the 2D complex coherence states", Opt. Lett. (2019) (Accepted in Opt. Lett.).

[24] L. Ma and S. A. Ponomarenko, "Optical coherence gratings and lattices", Opt. Lett. 39, 6656-6659 (2014).

[25] G. A. Siviloglou and D. N. Christodoulides, "Accelerating finite energy Airy beams", Opt. Lett. 32, 979-981 (2007).

[26] J. W. Goodman, *Statistical Optics* (John Wiley and Sons, Inc., 2000).

[27] J. Wallis, D. Gregory and J. Caswell, "A Letter of Dr. Wallis to Dr. Sloan, concerning the Quadrature of the Parts of the Lunula of Hippocrates Chius, performed by Mr. John Perks; with the further Improvements of the same, by Dr. David Gregory, and Mr. John Caswell", Philos. Trans. Roy. Soc. Lond. 21, 411-418 (1699).

[28] H. Eves, "A graphometer", The Math. Teacher 41, 311-313 (1948).

[29] X. Chen, O. Korotkova, "Complex degree of coherence modeling with famous planar curves", Opt. Lett. 43, 6049-6052 (2018).

[30] G. Gbur and T. D. Visser, *The Structure of Partially Coherent Fields*, in Prog. Opt. Editor E. Wolf, 55, 285-341 (2010).

[31] J. Bernoulli, Acta Eruditorum 9, 336338 (1694); reprinted in J. Bernoulli, Opera, Geneva, 1744 (reprint Brussels, Culture and Civilization, 1967), pp. 608-612.

[32] J. Russel, R. Cohn, *Centered Trochoid* (Bookvika Publishing, 2012).

[33] D. H. Nash, "Rotary engine geometry", Math. Mag. 50, 87-89 (1977).

[34] G. Grandi, "Florum Geometricorum Manipulus Regiae Societati Exhibitus, Phil. Trans. Roy. Soc. Lond. 32, 355-371 (1722).

[35] A. Forbes, A. Dudley, and M. McLaren, "Creation and detection of optical modes with spatial light modulators", Adv. Opt. Photon. 8, 200–227 (2016).

[36] B. Ndagano, N. Mphuthi, G. Milione, and A. Forbes, "Comparing mode-crosstalk and mode-dependent loss of laterally displaced orbital angular momentum and HermiteGaussian modes for free-space optical communication", Opt. Lett. 42, 4175–4178 (2017).

[37] J. Wang et al., "Terabit free-space data transmission employing orbital angular momentum multiplexing", Nat. Photon. 6, 488-496 (2012).

[38] J. C. Ricklin and F. M. Davidson, "Atmospheric optical communication with a Gaussian Schell beam", J. Opt. Soc. Am. A 20, 856–866 (2003).

[39] J. Li, X. Chen et al., "Mitigation of atmospheric turbulence with random light carrying OAM", Opt. Commun. (2019) (Accepted in Opt. Commun.)

[40] X. Chen, J. Li, S. M. Hashemi and O. Korotkova, "Synthesis of Im-Bessel correlated beam via coherent modes", Opt. Lett. 43, 3590-3593 (2018).

[41] J. M. Schmitt and G. Kumar, "Turbulent nature of refractive-index variations in biological tissue", Opt. Lett. 21, 1310-1312 (1996).

[42] M. Xu, "Plum pudding random medium model of biological tissue toward remote microscopy from spectroscopic light scattering", Biomed. Opt. Express 8, 2879-2895 (2017).

[43] Y. Zhang et al., "Supramolecular delivery of photoactivatable fluorophores in developing embryos", Proc. of SPIE 10078 (2017).

[44] Y. Zhang et al., "Multicolor super-resolution imaging using spectroscopic single-molecule localization microscopy with optimal spectral dispersion", Appl. Opt. 58, 2248-2255 (2019).

[45] E. R. Thapaliya et al., "Bright and compact macromolecular probes for bioimaging applications", Proc. of SPIE 10507 (2018).

[46] X. Chen, J. Li, and O. Korotkova, "Light scintillation in soft biological tissues", Waves in Random and Complex Media (in press, 2018).

[47] M. Hunter et al., "Tissue self-affinity and polarized light scattering in the Born approximation: a new model for precancer detection", Phys. Rev. Lett. 97, 138102 (2006).

[48] A. J. Gomes et al., "In vivo measurement of the shape of the tissue-refractive-index correlation function and its application to detection of colorectal field carcinogenesis", J. Biomed. Opt. 17, 159801 (2012).

[49] N. Das et al., "Probing multifractality in tissue refractive index: prospects for precancer detection", Opt. Lett. 38, 211-213 (2013).

[50] N. Das et al., "Tissue multifractality and Born approximation in analysis of light scattering: a novel approach for precancers detection", Scien. Reps. 4, 6129 (2014).

[51] N. K. et al., "Probing multifractality in depth-resolved refractive index fluctuations in biological tissues using backscattering spectral interferometry", J. Opt. 18, 125301 (2016).

[52] C. J. R. Sheppard. Scattering by fractal surfaces with an outer scale. Opt. Commun. 122, 178-188 (1996).

[53] V. V. Tuchin, *Tissue Optics, Light Scattering Methods and Instruments for Medical Diagnostics*, Third Edition (SPIE Press, 2015).

[54] V. V. Tuchin, "Tissue optics and photonics: biological tissue structures: review", *J. of Biomed. Photon. and Eng.* 1, 3-21, (2015).

[55] M. Shan, M. E. Kandel, and G. Popescu, "Refractive index variance of cells and tissues measured by quantitative phase imaging," *Opt. Express* 25, 1573-1581 (2017).

[56] B. E. Danheke, Editor, *Measurement of Suspended Particles by Quasi-Elastic Light Scattering*, (Wiley-Interscience: New York, 1983).

[57] D. Huang, E. A. Swanson, C. P. Lin, J. S. Schuman, W. G. Stinson, W. Chang, M. R. Hee, T. Flotte, K. Gregory, C. A. Puliafito, and J. G. Fujimoto, "Optical coherence tomography", Science 254, 1178-1181 (1991).

[58] N. Gnosh and I. A. Vitkin, "Tissue polarimetry: concepts, challenges, applications and outlook", *J. Biomed. Opt.* 16, 110801 (2011).

[59] W. Denk, J. H. Strickler and W. W. Webb, "Two-photon laser scanning fluorescence microscopy", *Science* 248, 4951, 73-76 (1990).

[60] Y. Zhang et al., "Far-red photoactivatable BODIPYs for the super-resolution imaging of live cells", J. Am. Chem. Soc. 140 12741-12745 (2018).

[61] Y. Zhang et al., "A photoactivatable far-red/near-Infrared BODIPY to monitor cellular dynamics in vivo", ACS Sens. 3 1347-1353 (2018).

[62] S. Nickell, M. Hermann, M. Essenpreis, T. J. Farrell, U. Kramer and M. S. Patterson, "Anisotropy of light propagation in human skin", *Phys. Med. Biol.* 45, 2873-2886 (2000).

[63] R. V. Beers, B. Aernouts, M. M. Reis, and W. Saeys, "Anisotropic light propagation in bovine muscle tissue depends on the initial fiber orientation, muscle type and wavelength", *Opt. Express* 25, 22082-22095 (2017).

[64] J. Heiskala, I. Nissil, T. Neuvonen, S. Jrvenp, and E. Somersalo, "Modeling anisotropic light propagation in a realistic model of the human head," *Appl. Opt.* 44, 2049-2057 (2005).

[65] T. Yun, N. Zeng, W. Li, D. Li, X. Jiang, and H. Ma, "Monte Carlo simulation of polarized photon scattering in anisotropic media," *Opt. Express* 17, 16590-16602 (2009).

[66] O. V. Angelsky, A. G. Ushenko,G., Yu. A. Ushenko, Ye, G. Ushenko, Y. Y. Tomka, V. P. Pishak, "Polarization-correlation mapping of biological tissue coherent images," *J. of Biomed. Opt.* 10, 064025 (2005).

[67] Y. A. Ushenko, O. I. Telenga, A. P. Peresunko, and O. K. Numan"New parameter for describing and analyzing the optical-anisotropic properties of biological tissues," *J. of Innovative Optical Health Sciences* 4, 463-475 (2011).

[68] O. Korotkova, *Random Beams: Theory and Applications* (CRC Press, Boca Raton, FL, 2013).

[69] X. Chen and O. Korotkova, "Optical beam propagation in anisotropic biological tissue", OSA Continuum 1, 1055-1067 (2018).

[70] F. Wang and O. Korotkova, "Random optical beam propagation in anisotropic turbulence along horizontal links", *Opt. Express* 24, 24422-24434 (2016).

[71] Mie Gustav, "Beitrge zur Optik trber Medien, speziell kolloidaler Metallsungen", Annalen der Physik. 330 377-445 (1908).

[72] X. Chen and O. Korotkova, "Scattering of light from particles with hollow semi-hard edge potentials", Computer Optics 40, 635-641 (2016).

[73] X. Chen and O. Korotkova, "Probability density functions of instantaneous Stokes parameters on weak scattering", Opt. Commun. 400, 1-8 (2017).

[74] T. Wang, D. Zhao, "Stokes parameters of an electromagnetic light wave on scattering", Opt. Commun. 285, 893-895 (2012).

[75] O. Korotkova and E. Wolf, "Generalized Stokes parameters of random electromagnetic beams", Opt. Lett. 30, 198-200 (2005).

[76] Y. Zhu, D. Zhao, "Stokes parameters and degree of polarization of nonparaxial stochastic electromagnetic beams", Phys. Lett. A. 373, 1595-1598 (2009).

[77] C. Brosseau, *Fundamentals of Polarized Light: A Statistical Optics Approach*, (Wiley, 1998).

[78] R. Barakat, "Statistics of the Stokes parameters", J. Opt. Soc. Amer. A 4, 1256-1263 (1987).

[79] C. Brosseau, R. Barakat and E. Rockower, "Statistics of the Stokes parameters for Gaussian distributed fields", Opt. Commun. 82, 204 (1991).

[80] D. Eliyahu, "Vector statistics of correlated Gaussian fields", Phys. Rev. E 47, 2881 (1993).

[81] R.A. Silverman, "Scattering of plane waves by locally homogeneous dielectric noise", Proc. Cambridge Philos. Soc. 54, 530 (1958).